IMPROVED SAMPLE INTRODUCTION SYSTEMS FOR INDUCTIVELY COUPLED PLASMA OPTICAL EMISSION SPECTROMETRY AND THEIR APPLICATION TO THE ANALYSIS OF SIMPLE AND COMPLEX MATRICES

By

Tia Kimberley Anderlini

A thesis submitted to the Graduate Program in Chemistry

in conformity with the requirements for the

Degree of Master of Science

Queen's University

Kingston, Ontario, Canada

November, 2016

Abstract

The objective of this thesis is to explore new and improved methods for greater sample introduction efficiency and enhanced analytical performance with inductively coupled plasma optical emission spectrometry (ICP-OES). Three projects are discussed in which the capabilities and applications of ICP-OES are expanded:

1. In the first project, a conventional ultrasonic nebuliser was modified to replace the heater/condenser with an infrared heated pre-evaporation tube. In continuation from previous works with pre-evaporation, the current work investigated the effects of heating with infrared block and rope heaters on two different ICP-OES instruments. Comparisons were made between several methods and setups in which temperatures were varied. By monitoring changes to sensitivity, detection limit, precision, and robustness, and analyzing two certified reference materials, a method with improved sample introduction efficiency and comparable analytical performance to a previous method was established.
2. The second project involved improvements to a previous work in which a multimode sample introduction system (MSIS) was modified by inserting a pre-evaporation tube between the MSIS and torch. The new work focused on applying an infrared heated ceramic rope for pre-evaporation. This research was conducted in all three MSIS modes (nebulisation mode, hydride generation mode, and dual mode) and on two different ICP-OES instruments, and comparisons were made between conventional setups in terms of sensitivity, detection limit, precision, and robustness. By tracking both hydride-forming and non-hydride forming elements, the effects of heating in combination with hydride generation were probed. Finally, optimal methods were validated by analysis of two certified reference materials.

3. A final project was completed in collaboration with ZincNyx Energy Solutions. This project sought to develop a method for the overall analysis of a 12 M KOH zincate fuel, which is used in green energy backup systems. By employing various techniques including flow injection analysis and standard additions, a final procedure was formulated for the verification of K concentration, as well as the measurement of additives (Al, Fe, Mg, In, Si), corrosion products (such C from CO_3^{2-}), and Zn particles both in and filtered from solution. Furthermore, the effects of exposing the potassium zincate electrolyte fuel to air were assessed.

Acknowledgements

I would like to express my sincere thanks to my supervisor, Dr. Diane Beauchemin, for her guidance, support, and pursuit of progress and success throughout my degree, for always keeping my options open and for putting up with my stubbornness.

I am hugely grateful to Agilent Technologies for the use of their demo instrument. I was extremely privileged in being able to use this instrument for the majority of my degree, and hope that Baby Gerber goes on to do great things. Additionally, thank you to Dr. David Bruce at ZincNyx Energy Solutions for his enthusiasm and suggestions throughout our collaboration.

I am also grateful to Dr. Loock and Dr. Oleschuk for serving on my committee and for providing important feedback and insight that has helped me see this work in a different light. I would like to acknowledge the financial assistance from the Natural Sciences and Engineering Research Council of Canada (NSERC), and Queen's University School of Graduate Studies and Research.

Thank you to the past and present Beauchemin group members for the laughs, support, and friendship they have provided since day one in the lab. Special thanks to Nausheen for being the best desk mate I could ask for and for convincing me to go back to Queen's, and to Lucas for being a great brother and boar since day one in 213. Thank you Michelle for trusting that an end was in sight, and for being the getaway I've needed time and time again. Finally, I would like to express my huge gratitude to my mum, dad, and brother for their constant support and love. Thank you dad for always backing me through the good and the bad and for emphasizing that it will all work out in the end. Thank you mum for reminding me of my goals, for being exceptionally understanding of my choices, my frustrations, and my fears, and for being the incredible support that has gotten me this far.

Table of Contents

List of Figures

List of Tables

List of Abbreviations

CCD	Charge-coupled device
CIROS	Circular optical system
CTD	Charge transfer device
CVG	Chemical vapour generation
DLA	Diagonal linear array
FI	Flow injection
HC	Heater/condenser
HG	Hydride generation
HT	Heating tape
ICP-MS	Inductively coupled plasma mass spectrometry
ICP-OES	Inductively coupled plasma optical emission spectrometry
IR	Infrared
LTE	Local thermodynamic equilibrium
MOS	Metal oxide semiconductor
MSIS	Multimode sample introduction system
PEEK	Polyether ether ketone
PET	Pre-evaporation tube
PMT	Photomultiplier tube

PN	Pneumatic Nebuliser
RF	Radio frequency
RSD	Relative standard deviation
STD ADD	Standard additions
TEP	Total excitation potential
USN	Ultrasonic nebuliser
VDV	Vertical dual view

Chapter 1: Introduction

1.1 ICP-OES for Multi-Elemental Analysis

1.1.1 ICP-OES vs. ICP-MS

Known as the predominant methods for elemental analysis of samples in industrial, biological, environmental, pharmaceutical, and forensic science [1], inductively coupled plasma optical emission spectrometry (ICP-OES) and ICP mass spectrometry (ICP-MS) see continuous technological advances for improving their accuracy and precision at low detection limits in a variety of matrices. ICP-OES is a principal method for the multi-elemental determination of major, minor and trace elements [2, 3]. ICP-MS is generally saved for multi-elemental analysis at ultra-trace levels. Although it has greater sensitivities and lower detection limits than ICP-OES [4], ICP-MS lacks in its ability to resist matrix effects. Due to its characteristic passive measurement of emitted light, ICP-OES is intrinsically more robust than ICP-MS, which requires the physical extraction of ions from the plasma [5]. In fact, 0.2% m/v is the maximum dissolved solid content that can be tolerated by ICP-MS during continuous nebulization, due to clogging of the sampler and skimmer cones. This can frequently result in the need for extensive sample pre-treatment and dilution. On the other hand, ICP-OES can handle up to several % m/v dissolved solid content, nodding to simpler and faster sample preparation. If the detection capabilities of ICP-OES were greatly improved, the benefits of using ICP-MS could be achieved, while retaining the benefits of ICP-OES. With this in mind, the main goal of this thesis is to explore and expand the analytical capabilities of ICP-OES.

1.1.2 Fundamentals of the ICP

The ICP was originally created for OES in the mid-1960s by Fassel et al. at Iowa State University and by Greenfield et al. at Albright & Wilson, Ltd. [6, 7], and was only later developed for mass

spectrometry. Since then, detection limits have been improved for ICP-OES by several orders of magnitude, through continuous development of the system and its operation. Figure 1.1 shows an ICP torch assembly, in which three concentric fused-quartz tubes (the outer, intermediate, and inner gas tubes) make up the ICP torch [8]. A copper coil, known as the load coil, surrounds the upper portion of the torch and is connected to a radio frequency (RF) generator. RF power is applied to the load coil, resulting in an alternating current moving through the coil with an oscillation corresponding to the frequency of the generator. This current oscillation results in the same high-frequency oscillation of magnetic and electric fields being set up in the upper region of the torch. Meanwhile, argon gas flows through the torch and a spark from the Tesla coil strips electrons from some argon atoms. These "seed" electrons are accelerated by the magnetic field, collide with more argon atoms, and inevitably strip off more electrons in a chain reaction. Eventually, the culmination of these collision interactions produces the inductively coupled plasma discharge – a high-temperature plasma consisting of argons atoms, electrons, and ions. This plasma is maintained by continuously adding energy through the RF coil, which is then transferred to the electrons in a process known as inductive coupling [9].

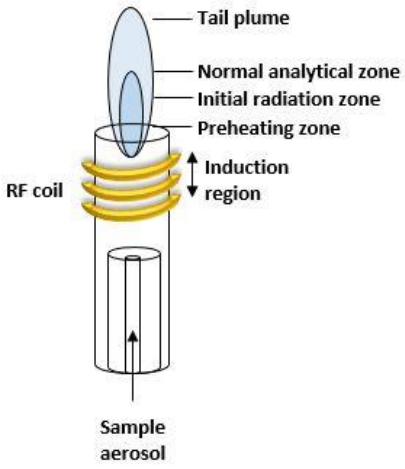

Figure 1.1: Schematic of the ICP torch assembly, showing the three quartz tubes, RF coil, and different regions of the plasma

Argon gas flows through the torch via three main gas flow connections: plasma, auxiliary, and aerosol carrier gas flows. The plasma gas flows through the outer-most tube of the torch and is responsible for sustaining the plasma and isolating it from the outer quartz tube. The auxiliary gas flows through the intermediate tube and, being optional, is simply used to position the plasma relative to the load coil. The aerosol carrier gas flow (or nebuliser flow) carries the sample aerosol through the inner tube and punches a hole through the central channel of the plasma.

When an aerosol is introduced into the plasma, a series of processes take place in the ICP. First, the solvent is removed from the sample aerosol, leaving behind microscopic particles of solid. The particles are then vapourized, resulting in gaseous molecules, and subsequently these molecules are dissociated into atoms (atomized). These processes take place primarily in the preheating zone (PHZ). Further up, in the initial radiation zone (IRZ) and normal analytical zone (NAZ), ionisation and excitation of the atoms and ions occur, ultimately resulting in the emission of radiation from the excited species.

1.1.3 SPECTRO ARCOS vs. Agilent 5100

In order to detect and measure the light emitted by the excited atoms and ions in the plasma, the produced polyatomic radiation must be separated into individual wavelengths by a polychromator, which can measure light of several wavelengths at once. However, the actual detection of light is done by a photosensitive detector (i.e. a photomultiplier tube (PMT), charge-injection device, or a charge-coupled device) [8, 9]. Since both instruments used in this work, the SPECTRO ARCOS and the Agilent 5100, use a charge-coupled device (CCD), only this detector will be discussed in detail.

A CCD is one type of detector in a broad range of solid-state silicon-based array detectors known as charge transfer devices (CTDs). A CCD is made up of MOS (metal-oxide semiconductor) detectors which range in size from 5-50 µm wide, and up to 200 µm high, and which can be arranged in two-dimensional arrays [9]. The MOS capacitors (also known as pixels) are each composed of a metal

electrode, a p-type silicon substrate, and a thin, top, insulating layer of SiO_2. Photons striking a detector give rise to electron-hole pairs, the resulting electrons being stored in a potential well in the silicon below the metal electrode. The amount of charge accumulated is proportional to the incident light intensity and the integration time. Two periods of an acquisition cycle occur to result in the reading of an image. In the first period, the detector is exposed to light and charge accumulates in the active MOS detectors, while the pixels adjacent to an active pixel are kept inactive to avoid bleeding of charge. The total time it takes for this period to occur is called the "integration time." In the second period, the charges are extracted. The collected charge on the MOS capacitors can only be read sequentially, and therefore is destroyed in the process of being read. To do so, a voltage is applied to the pixel adjacent to the MOS which accumulated the charge, thereby attracting the electrons to the adjacent pixel. Meanwhile, the voltage of the former active pixel is slowly decreased. Hence, the charges are moved through the CCD's rows until they reach the final row. Unfortunately, a main obstacle with applying CCDs to spectroscopic applications is the disproportion of the small surface area of the detector and the large focal plane of polychromators.

Although both instruments in this work use a CCD detector, there is a marked difference between the two in terms of detection. The difference falls in the different methods to overcome the mismatch between the detector and the focal plane described above. The SPECTRO ARCOS measures from 130 nm to 770 nm using 32 linear arrays [10] positioned along a Circular Optical System (CIROS), which is based on a Rowland circle design (Fig 1.2). While a typical PMT Rowland circle monitors discrete wavelengths, the CIROS system allows for a large wavelength coverage and a high resolution. As can be expected from the Rowland circle design, such instruments can take up considerable space, which is avoided in newer models of ICP-OES instruments.

The Agilent 5100 does not have the large space requirement of the ARCOS' Rowland circle. Measuring a wavelength range of 167-785 nm, the Agilent 5100 uses an echelle optical mount design

(Fig. 1.3) with a VistaChip II detector. The computer-optimized echelle optical design involves focusing the echelle image onto the instrument's single detector. After entering through the single entrance slit, the light from the plasma is collected by mirrors and directed to an echelle grating (94.74 lines/mm) and CaF_2 prism cross disperser, creating an echellogram of 70 orders. This echellogram is then projected onto the CCD detector (VistaChip II). Made up of 70 diagonal linear arrays (DLAs) of pixels that are aligned to precisely match the individual spectral free range of each diffraction order produced by the echelle optics, the VistaChip II functions to correct the mismatch between conventional CCD arrays and the focal plane of the echelle Spectrometer. The VistaChip measures 15 mm by 19 mm, with a total of 70,000 pixels packed on the 70 DLAs [11] – a huge contrast to the 32 detectors needed to cover a similar wavelength range on the SPECTRO ARCOS.

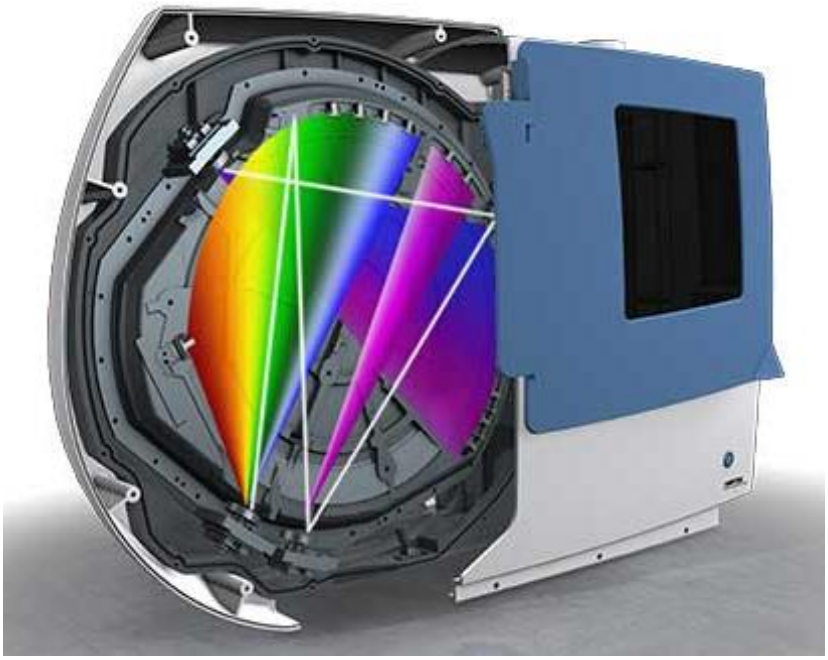

Figure 1.2: SPECTRO ARCOS Rowland circle design (Courtesy of SPECTRO Analytical Instruments GmbH*)*

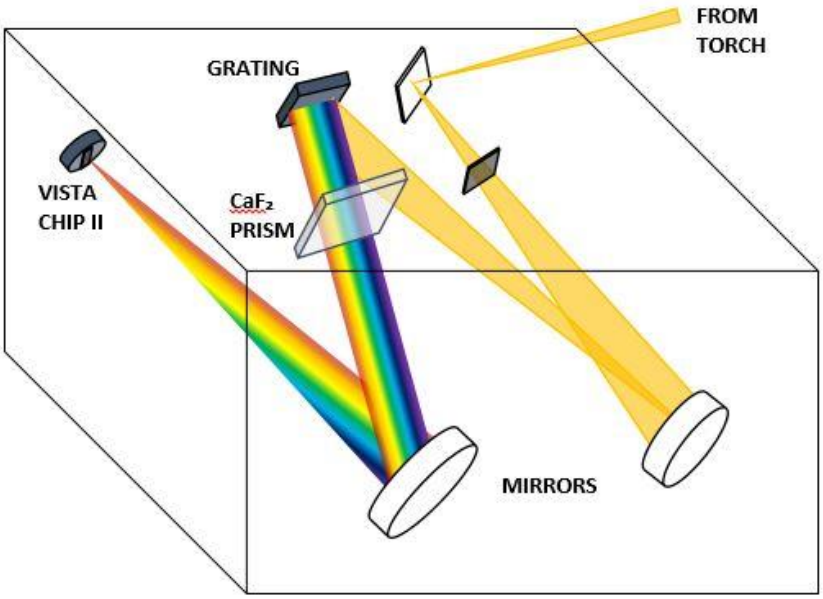

Figure 1.3: Agilent 5100 echelle optics

The other primary difference between the SPECTRO ARCOS and the Agilent 5100 is the torch viewing modes. The SPECTRO ARCOS has only lateral viewing, while the Agilent 5100 functions in both lateral (called radial by the vendor, which is not commensurate with light being measured in a single line of sight instead of from all around the plasma as implied by the term radial), and axial viewing modes as mirrors direct the collected light from the plasma to the detector. Therefore, axial and lateral modes can be operated sequentially without changing the physical position of the torch. This configuration is known as vertical dual view (VDV). While lateral view is known to be inherently more robust, axial view tends to have higher sensitivities and lower detection limits [9]. In lateral view, the observation volume is constrained in the NAZ, which therefore limits the effect of potential background and spectral interferences. In axial view, a longer viewing path down the axis of the plasma allows for a greatly improved sensitivity [8].

1.2 Sample Introduction Systems for ICP-OES

1.2.1 Conventional Sample Introduction for ICP-OES

A typical sample introduction system for ICP-OES consists of a nebulizer attached to a spray chamber, which is clamped to the torch. A peristaltic pump feeds the sample through capillary tubing to the nebuliser, which aspirates the sample [12]. In order for the plasma to reproducibly desolvate, vaporize, atomize, ionize, and excite the analyte, the sample introduction system must deliver the sample as an aerosol rather than a stream of liquid [9]. Furthermore, the system should prevent or at least greatly reduce the possibility of clogging the torch injector with particulates, which would inevitably extinguish the plasma [13]. Hence the ability of the nebuliser to produce small droplets for various samples is imperative to the sample introduction efficiency (Section 1.2.2). In the case of solid samples (including soils, food materials, fertilizers, and animal tissues), extraction or digestion is required prior to analysis in order to produce samples in aqueous solution [9].

In essence, the nebuliser determines the transport efficiency, which is defined as the ratio of the amount of analyte entering the plasma to the quantity of aspirated analyte [14]. In the case of conventional pneumatic nebulisation (PN), which uses a pneumatic nebuliser and spray chamber, this value is 2-5%, with 95-98% of the sample going down the drain [13]. Further drawbacks with this sample introduction system include the large variation in droplet size, which can greatly increase the noise level. Following desolvation and vaporisation, large droplets will cool the plasma and the surrounding smaller droplets that have been atomized, ionized, and excited, thereby reducing the number of excited atoms and ions. Reducing droplet size is therefore a key component to improving sensitivities and detection limits. Ultrasonic nebulisation is an alternative sample introduction system, which aims to increase transport efficiency and reduce noise sources. By pumping the solution onto the surface of a piezoelectric transducer, an extremely fine aerosol is produced via ultrasonic waves interacting with the

liquid film [13]. Furthermore, a desolvation system vaporizes and condenses the sample, which reduces the solvent load. Together, these characteristics result in a reduced average droplet size and a transport efficiency of 5-20%, depending on the sample solution [15]. The ultrasonic nebuliser is discussed in more detail in Section 1.2.2.

1.2.2 Nebulisers

As the work of this thesis focuses more heavily on differences among nebulisers than on spray chambers, only the former will be discussed. Five different nebulisers were used in this work: Seaspray, V-groove, and OneNeb all from Agilent Technologies; MiraMist from Burgener Nebulisers; and an ultrasonic nebuliser by CETAC.

Figure 1.4: Seaspray nebuliser (Courtesy of Glass Expansion)

The most basic of these nebulisers is the Seaspray. This borosilicate glass concentric nebuliser involves a solution being introduced through a capillary tube to a region of low pressure, which is produced from gas flowing quickly past the end of the capillary [9]. This low-pressure, high-speed gas combination draws the liquid into the gas stream, which breaks up the solution into an aerosol. While concentric nebulisers are often plagued by clogging due to their small liquid and gas orifices, the Seaspray nebuliser can handle up to 20% salt solutions in continuous operation. This is due to its smooth, uniform design to minimize the adhesion of salt crystals, as well as its self-washing tip, which uses the washing action of the dispersing droplet to inhibit further crystal growth [16].

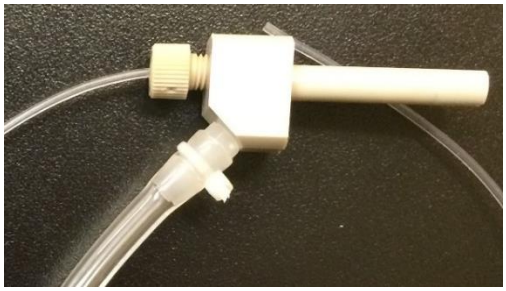

Figure 1.5: Prototype V-groove nebuliser

The V-groove nebuliser from Agilent is a prototype, meaning little can be said about the specific characteristics of this model, except for its construction from inert materials. This allows Agilent's V-groove to analyze strong acids and bases, as well as organic solvents. Generally speaking, a V-groove nebuliser, which is a variation of a Babington nebuliser, is used for the analysis of a high-solid content and can handle the nebulisation of suspended particles [12]. This nebuliser works by allowing the liquid sample to flow down a groove with a small orifice in the centre for the nebulizing gas. The high speed gas exiting this hole shears the flowing liquid, resulting in an aerosol [9, 17, 18].

Figure 1.6: MiraMist nebuliser (Courtesy of Burgener Research Inc.)

The MiraMist nebuliser, developed by Burgener [19], is an enhanced parallel path nebuliser, in which the gas stream and the sample solution flow through the nebuliser in parallel capillaries. Due to the surface tension along a spout that dips into the gas stream at the tip of the nebuliser, the liquid is pulled along the gas stream. This results in the gas and liquid interacting where the speed of the gas is at

its maximum, meaning a more efficient transfer of energy, and a finer aerosol droplet size [20]. In contrast to the V-groove nebuliser in which sample flows down a groove onto the nebulizer gas outlet, the Burgener nebulisers do not rely on gravity to deliver liquid to the gas stream, and therefore can operate in any orientation. As this nebuliser is made of PEEK, it can handle most samples except concentrated acids and some organic solvents.

Figure 1.7: OneNeb nebuliser (© Agilent Technologies, Inc. 2012.
Reproduced with Permission, Courtesy of Agilent Technologies, Inc.)

The OneNeb from Agilent is a new design based on Flow Blurring technology, in which the sample mixes with the gas flow at a high turbulence at the nozzle of the nebuliser [21]. This turbulent mixing creates an aerosol of extremely fine micro- and nano-scale droplets. With a constant capillary diameter, and no drop in pressure, blockage of the OneNeb is practically eliminated, and high solid concentration samples can be routinely nebulised. Furthermore, the OneNeb is made completely of inert materials, enabling the analysis of strong acids and bases as well as common organic solvents.

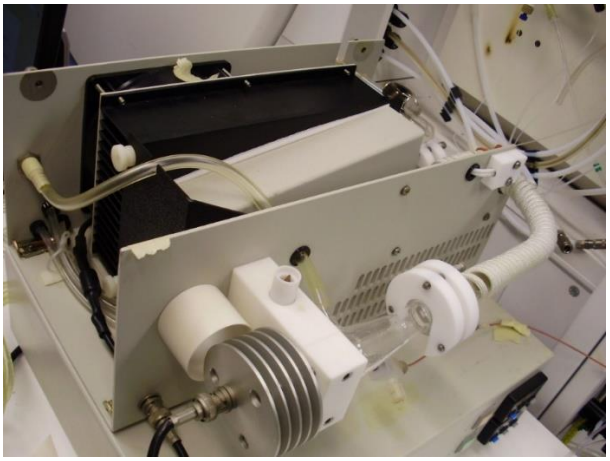

Figure 1.8: Ultrasonic nebuliser (with lid removed to show heater and condenser)

The ultrasonic nebuliser (USN) uses sound waves instead of a gas to generate the sample aerosol. The liquid sample is pumped onto a piezoelectric crystal, which is driven by an ultrasonic generator at a frequency of 10-200 MHz [12]. The oscillations of the piezoelectric transducer break the sample into an extremely fine aerosol that reaches the ICP with high efficiency, resulting in 10-fold improvements in detection limit over conventional pneumatic nebulisation [9]. Due to the high efficiency of the USN, the ICP experiences an increased water load. Therefore, a heater/condenser (HC) system is used to vaporise and condense the solvent following nebulisation. This combination of reducing the average droplet size, and pre-concentrating the analyte with solvent removal effectively improves sensitivities and detection limits [5, 22]. However, it also exacerbates matrix effects, as the matrix is preconcentrated along with the analytes.

1.2.3 Multimode Sample Introduction System

While ultrasonic nebulisation can be hugely beneficial for reducing detection limits, it can fail in the detection on some elements such as Hg and B, which can be lost in the HC system [5]. In order to preserve such elements and achieve even lower detection limits for hydride-generating elements, a multimode sample introduction system can be used. The multimode sample introduction system (MSIS)

was invented by McLaughlin and Brindle [23] to produce vapour-phase species in an unconfined gap at the very center of a cyclonic spray chamber [24]. This invention was based on the concept of hydride generation (HG), also referred to as chemical vapour generation (CVG), whereby a sample in dilute acid is mixed with a reducing agent to produce atomic hydrogen and this hydrogen reacts with As, Bi, Cd, Hg, Ge, Pb, Sb, Se, Te, and Sn in solution to form volatile hydrides [25]. These hydride compounds are separated from the reaction mixture and transported to the plasma with an efficiency of nearly 100%, resulting in improvements in detection limit of up to a factor of 1000 when compared to conventional pneumatic nebuliser (PN) and spray chamber setup [9]. In contrast to other devices for CVG, MSIS can be operated in three modes: dual mode, which involves both vapour generation and nebulisation; vapour generation mode, which strictly involves CVG without nebulisation of the sample; and nebulisation mode, which is simply conventional nebulisation with a cyclonic spray chamber and without CVG [26].

1.2.4 Flow Injection

Flow injection works by injecting a liquid sample aliquot into a carrier that flows continuously through the sample introduction system, thereby pushing the sample along with it. This carrier may be either a solution simply to continuously feed the plasma, or a reagent that reacts with the sample [27]. As the sample moves through the system, the sample zone broadens, and may react with the reagent carrier, forming the product prior to being read by the detector [28]. Flow injection is advantageous over “batch processes” of sample preparation and analysis by providing increased speed and easier sample handling. Additionally, in the case of the applications of this thesis, flow injection can be useful when analyzing corrosive materials that may attack the sample introduction system and degrade it with continuous use [29, 30]. Rather than diluting such a sample, which may contaminate it in the process,

minute aliquots can be injected into the system, thereby reducing negative impacts on the torch, spray chamber, and nebuliser, while preventing reduction of analyte detection.

1.2.5 Pre-evaporation Systems

By pre-evaporating the analyte and solvent prior to them reaching the plasma, sample introduction efficiency may be increased and noise sources may be reduced. The pre-evaporation technique not only reduces noise by eliminating large sample droplets that cool the plasma; this method also avoids the removal of water (as is done by a USN-HC, for example), which prevents pre-concentration of the matrix and allows water to act as a load buffer in the plasma, thereby minimizing matrix effects [5]. Furthermore, the hydrogen atoms produced when water vapour enters the plasma facilitate the transfer of energy from the bulk of the plasma to the plasma's central channel and affects the ionization and excitation characteristics of the ICP [31].

Hence, the use of pre-evaporation sample introduction for improving detection limits, sensitivity, and robustness in ICP-based instruments is an area of extensive investigation by the Beauchemin Group. These improvements have been illustrated early on in ICP-MS applications [32], with ultrasonic nebulization for environmental applications [5, 22], with a multimode sample introduction system (MSIS) [25], and with conventional pneumatic nebulization with varying spray chambers [33]. Through the years, different models of IR heaters and heating tape have been tested, in search of a setup that provides the best heating uniformity. Using these methods, both improved robustness and detection limits have demonstrated the usefulness of ICP-OES with pre-evaporation over ICP-MS for analysis of low-ppb samples. For instance, when compared to a conventional pneumatic nebulization method, detection limits improved 10-25 fold, depending on the element and the type pf emission line used (i.e. atomic or ionic), with an ultrasonic nebulizer coupled to an infrared-heated pre-evaporation tube with ICP-OES [5].

1.3 Thesis Objectives

The goals herein are to build from past methods and create new methods for improved sample introduction efficiency and analytical capabilities of ICP-OES. Improvements in terms of sensitivity, detection limit, precision, and robustness will be made by new methods, in comparison to conventional sample introduction systems:

Objective 1 (addressed in Chapter 2): Investigate whether an improvement in analytical performance can be achieved using an IR rope heater instead of block heaters for a modified USN setup with a pre-evaporation tube. We will also see which of two ICP-OES instruments provides the greatest analytical improvements for the new methods, and which setup resulted in the most efficient system.

Objective 2 (addressed in Chapter 3): See if improvements in analytical performance can be met by applying pre-evaporation to MSIS using IR rope heaters. Results will be compared on two ICP-OES instruments for all three MSIS modes (nebulisation mode, hydride generation mode, and dual mode).

Objective 3 (addressed in Chapter 4): Develop a method for the overall analysis of a 12 M KOH zincate fuel. A final procedure will be created to analyze both the particle and liquid portions of the fuel, including the accurate measurement of dissolved analytes (Al, C, Fe, Mg, In, Si, Zn) and verification of K concentration.

1.4 References

[1] J.D. Winefordner, I.B. Gornushkin, T. Correll, E. Gibb, B. W. Smith and N. Omenetto, Comparing several atomic spectrometric methods to the super stars: special emphasis on laser induced breakdown spectrometry, LIBS, a future super star, J. Anal. At. Spectrom., (2004), 19, 1061–1083.

[2] El-Ghawi, U., Pátzay, G., Vajda, N and Dódizs, D. Analysis of selected fertilizers imported to Libya for major, minor, trace and toxic elements using ICP-OES and INAA, J. Radioanal. Nucl. Chem., (1999), 242, 693-701.

[3] Kira, C. S and Maihara, V. A., Determination of major and minor elements in dairy products through inductively coupled plasma optical emission spectrometry after wet partial digestion and neutron activation analysis. Food Chem., (2007), 100, 390-395.

[4] D. Beauchemin, Environmental analysis by inductively coupled plasma mass spectrometry. Mass Spectrom. Rev., (2010), 29, 560-592.

[5] A. Asfaw, W. MacFarlane and D. Beauchemin, Ultrasonic nebulization with infrared heated preevaporation tube for sample introduction in ICP-OES: application to geological and environmental samples, J. Anal. At. Spectrom., 27 (2012) 1254-1263.

[6] S. Greenfield, I.L. Jones, C.T. Berry, High-pressure Plasma as Spectroscopic Emission Sources, Analyst, 89(11), 713–720 (1964).

[7] R.H. Wendt, V.A. Fassel, Induction-coupled Plasma Spectrometric Excitation Source, Anal. Chem., 37(7), 920–922 (1965).

[8] Hou, X and Jones, B. T. Inductively Coupled Plasma-Optical Emission Spectrometry. In Encyclopedia of Analytical Chemistry; John Wiley & Sons, Ltd, (2000), 9468–9485.

[9] Boss, C.B and Fredeen, K. J. Concept, Instrumentation and Techniques in Inductively Coupled Plasma Optical Emission Spectrometry, Second Edition, Perkin Elmer, 1997.

[10] SPECTRO ARCOS brochure, http://www.potencialzero.com/media/33905/br_ARCOSen082011.pdf, Retrieved Sept. 17, 2016.

[11] Agilent 5100 specifications, http://hpst.cz/sites/default/files/attachments/5991-4838en-techoview-5100-optics.pdf, Retrieved Sept. 17, 2016.

[12] P. Gaines, Sample Introduction for ICP-MS and ICP-OES, Inorganic Ventures, Spectroscopy Solutions for Materials Analysis, (2005).

[13] J. Mora, S. Maestre, V. Hernandis and J. L. Todoli, Liquid-sample introduction in plasma spectrometry. Trends Anal. Chem., 22, (2003), 123 – 132.

[14] A. Montaser, Inductively coupled plasma mass spectrometry. Wiley-VCH: New York, 1998.

[15] Martin Brennan, A Practical Approach to Quantitative Metal Analysis of Organic Matrices, John Wiley & Sons Ltd., 2008.

[16] Seaspray brochure, http://www.geicp.com/site/images/flyers/SeaSprayFlyer.pdf, Retrieved Sept 17, 2016.

[17] R.F. Suddendorf, K.W. Boyer, Mechanical device to produce a finely dispersed aerosol, U.S. Patent 4,206,160, Issue date: Jun 3, 1980

[18] M.N.A. Noordermeer, One-piece high-solids nebulizer, U.S. Patent 4,880,164, Issue date: Nov 14, 1989

[19] MiraMist Manual, http://burgenerresearch.com/MiraMistManual.html, Retrieved Sept. 17, 2016.

[20] Enhanced Parallel Path Nebulisers, http://burgenerresearch.com/Enhanced.html, Retrieved Sept. 17, 2016.

[21] OneNeb brochure, http://www.agilent.com/cs/library/brochures/OneNeb%20nebulizer%20sales%20flyer.pdf, Retrieved Sept. 17, 2016.

[22] A. Asfaw and D. Beauchemin, Improvement of the Capabilities of Inductively Coupled Plasma Optical Emission Spectrometry by Replacing the Desolvation System of an Ultrasonic Nebulization System with a Pre-evaporation Tube, Spectrochim. Acta Part B 65 (2010) 376-384.

[23] R.I.J. McLaughlin, I.D. Brindle, Multimode Sample Introduction System, U.S Patent number 6,891,605; May 10, 2005

[24] R. McLaughlin, P. Cheese, M. Ding, A. Ptolemy, A. Conn, D. Brindle, (2006) Am. Lab., 13–17 41.

[25] A. Asfaw and D. Beauchemin, Combination of a multimode sample introduction system with a preevaporation tube to improve multi-element analysis by ICP-OES, J. Anal. At. Spectrom. 27 (2012) 8091.

[26] I. Brindle, Vapour-generation analytical chemistry: from Marsh to multimode sample-introduction system, Anal. Bioanal. Chem, (2007) 388:735–741

[27] D.C. Harris, Quantitative Chemical Analysis, 9th Edition, W.H. Freeman Company, New York, NY, 2016.

[28] J. Ruzicka, The second coming of flow-injection analysis, Anal. Chim. Acta, 261 (1992) 3-10.

[29] E. H. Hansen and J. Ruzicka, The principles of flow injection analysis as demonstrated by three lab exercises, J. Chem. Educ., (1979), 56 (10), p 677

[30] T. Imato, N. Ishibashi, Flow Injection Analysis of Concentrated Aqueous Solution of Strong Acids and Bases, Analyt. Sci, Vol. 1 (1985) No. 5 P 481-482

[31] S. E. Long and R. F. Browner, Influence of water on conditions in the inductively coupled argon plasma, Spectrochim. Acta, Part B, (1988), 43, 1461–1471.

[32] G. Peters and D. Beauchemin, Effect of Pre-evaporating the Solvent on the Analytical Performance of Inductively Coupled Plasma Mass Spectrometry, Spectrochim. Acta, Vol. 48B. No 12, (1993) 1481-1494.

[33] Y. Makonnen, J. Burgener and D. Beauchemin, “Improvement of Analytical Performance in Inductively Coupled Plasma Optical Emission Spectrometry without Compromising Robustness using an Infrared-Heated Sample Introduction System with a Pneumatic Nebulizer”, J. Anal. At. Spectrom. 30 (2015) 214–224

Chapter 2: Improvement of Sample Introduction to ICP-OES Using an Ultrasonic Nebulizer with an Infrared Heated Pre-Evaporation Tube

2.1 Introduction

Fast, robust, and sensitive multi-elemental analysis techniques for accurate and precise detection of samples are required across various disciplines including health and food sciences, geochemical exploration, pharmaceuticals, and atmospheric sciences. Two of the most common techniques for multi-elemental analysis are ICP-MS and ICP-OES [1-4]. While the former is used for ultra-trace elemental analysis, the latter is typically employed for analysis of major, minor, and trace elements. Although ICP-MS has a clear advantage in detection limits, ICP-OES wins in the category of robustness, as its passive measurement of light is able to resist matrix effects, while the physical extraction of ions in the plasma of ICP-MS subjects it to both spectroscopic and non-spectroscopic interferences [5]. If the detection abilities of ICP-OES could be improved to the level of ICP-MS, ICP-OES could see huge success in new-found applications across many disciplines. Therefore, this chapter will investigate the potential of improving sensitivities and detection limits of ICP-OES without sabotaging robustness.

One of the leading sample introduction systems for nearing this goal is the ultrasonic nebuliser. By greatly reducing the noise caused by variable droplet size, and increasing the transport efficiency, the USN generally results in a 10-fold improvement in detection limits over conventional pneumatic nebulisation with ICP-OES [6]. Through vaporising and condensing the sample aerosol with the USN's heater and condenser, respectively, solvent is removed to pre-concentrate the analyte and increase the sample introduction efficiency by 30% [7, 8]. However, in the process of pre-concentrating the analyte, the matrix is also pre-concentrated [9]. Moreover, some elements may be lost during the process of desolvation, and memory effects may become exacerbated by the heater/condenser and membrane desolvator [10, 11]. Finally, by removing water in the heater/condenser system, the beneficial attributes

of water as a load buffer in the plasma are also removed. Water typically minimizes matrix effects [12] and acts as the main source of hydrogen in the plasma. Having a high thermal conductivity, hydrogen facilitates the transfer of energy between the bulk and central channel of the plasma [13].

By replacing the heater/condenser of a USN with a pre-evaporation tube (PET), water is preserved while the benefits of ultrasonic nebulisation are still achieved [14, 15]. Using heating tape (HT) to heat the PET, improvements in detection limit in comparison to a conventional PN were achieved while preserving robustness. This method also allowed for the successful determination of Hg which otherwise would have been lost in the HC [15]. However, the plasma extinguished at sample uptake rates above 0.3 mL min^{-1} due to the high solvent load, and comparisons to USN-HC with membrane desolvator (MD) proved USN-PET(HT) to have insignificant improvements in detection limit and a degradation of instrumental precision.

Alternatively, by using an IR heater, the benefits of a fast heating rate and uniform temperature [16, 17] were realized. A USN-PET(IR) system was optimized with block infrared heaters and compared to both PN and USN-HC [14]. Resulting in a 10-25 fold improvement in detection limit over conventional PN, this USN-PET(IR) method proved that pre-evaporating the sample aerosol improves both the plasma excitation conditions and robustness by increasing the amount of water vapour entering the plasma. The objective of this work was therefore to improve on these past USN-PET methods using two types of infrared heaters at lower temperatures. While 400 °C had been used as the optimal temperature in the past work, the present goal was to see if a lower heating temperature would provide sufficient pre-evaporation. By optimizing this sample introduction system on two different ICP-OES instruments, important attributes for successful operation were uncovered, and a method with improved sample introduction efficiency was reached.

2.2 Experimental

2.2.1 Instrumentation

Method development and application was performed on an ARCOS ICP-OES instrument (lateral view, SPECTRO Analytical Instruments, Kleve, Germany) and an Agilent 5100 ICP-OES (dual view, Agilent Technologies, Santa Clara, California, United States). These instruments were equipped with a cyclonic double-pass spray chamber and pneumatic Seaspray nebuliser (both Agilent Technologies, Santa Clara, California, United States), which were used for reference experiments. The conventional pneumatic nebulisation setup was replaced on both instruments with a CETAC U-6000 AT+ USN-HC (CETAC Technologies, Omaha, Nebraska, USA). This USN-HC setup was further adjusted by removing the HC and inserting an IR-heated pre-evaporation glass tube and sheathing device. The optimal operating conditions for all setups are provided in Tables 2.1 and 2.2.

Table 2.1: Optimal conditions for sample introduction systems with SPECTRO ARCOS

Condition	PN	PN [14]	USN-HC [14]	USN-PET(IR) 400°C* block	USN-PET(IR) 300°C block	USN-PET(IR) 160°C block	USN-PET(IR) 250°C rope
RF Power (W)	1400	1450	1400	1400	1400	1400	1400
Plasma observation height (mm)	11.0	11.0	11.0	11.0	11.0	11.0	11.0
Plasma gas flow rate (L min^{-1})	12.00	12.00	12.00	12.00	12.00	12.00	12.00
Auxiliary gas flow rate (L min^{-1})	1.0	1.0	1.0	2.50	2.50	2.50	2.50
Sample uptake rate (mL min^{-1})	2.0	2.0	2.0	1.5	0.8	0.5	0.8
Drain removal rate (mL min^{-1})	11.0	11.0	15.0	15.0	15.0	15.0	15.0
Aerosol carrier gas flow rate (L min^{-1})	1.00	0.70	0.75	0.25	0.33	0.33	0.43
Sheathing gas flow rate (L min^{-1})	---	---	---	0.40	0.40	0.40	0.40
USN heater temperature (°C)	---	---	140	---	---	---	---
USN condenser temperature (°C)	---	---	3	---	---	---	---

Table 2.2: Optimal conditions for sample introduction systems with Agilent 5100

Condition	PN	USN-HC Lateral	USN-HC Axial	USN-PET(IR) Rope Lateral	USN-PET(IR) Rope Axial
RF Power (kW)	1.40	1.45	1.45	1.5	1.5
Plasma gas (L/min)	12	12	12	12	12
Aux gas (L/min)	1.0	2.0	2.0	2.0	2.0
Aerosol carrier gas (L/min)	0.7	0.5	0.5	0.3	0.2
Sheath gas (L/min)	N/A	N/A	N/A	0.4	0.4
Sample uptake (mL/min)	2.0	2.0	2.0	2.0	2.0
IR Temperature (°C)	N/A	N/A	N/A	250	250
USN heater temperature (°C)	N/A	140	3	N/A	N/A
USN condenser temperature (°C)	N/A	140	3	N/A	N/A
Plasma observation height (mm)	6	1	N/A	6	N/A

2.2.2 IR-heated pre-evaporation system

The IR-heated pre-evaporation system, illustrated in Fig. 2.1, involved a 38.1 cm long glass tube with a 28mm/15mm glass ball joint connected to the USN at one end, and a 12mm/5mm joint connected to a sheathing device at the other end. The 7 cm long sheathing device with 12mm/5mm ball inlet-socket ends was connected to a conventional ICP torch (Agilent Technologies, Santa Clara, California, United States, and SCP Science, Baie d'Urfe, Quebec, Canada, for the 5100 and ARCOS, respectively).

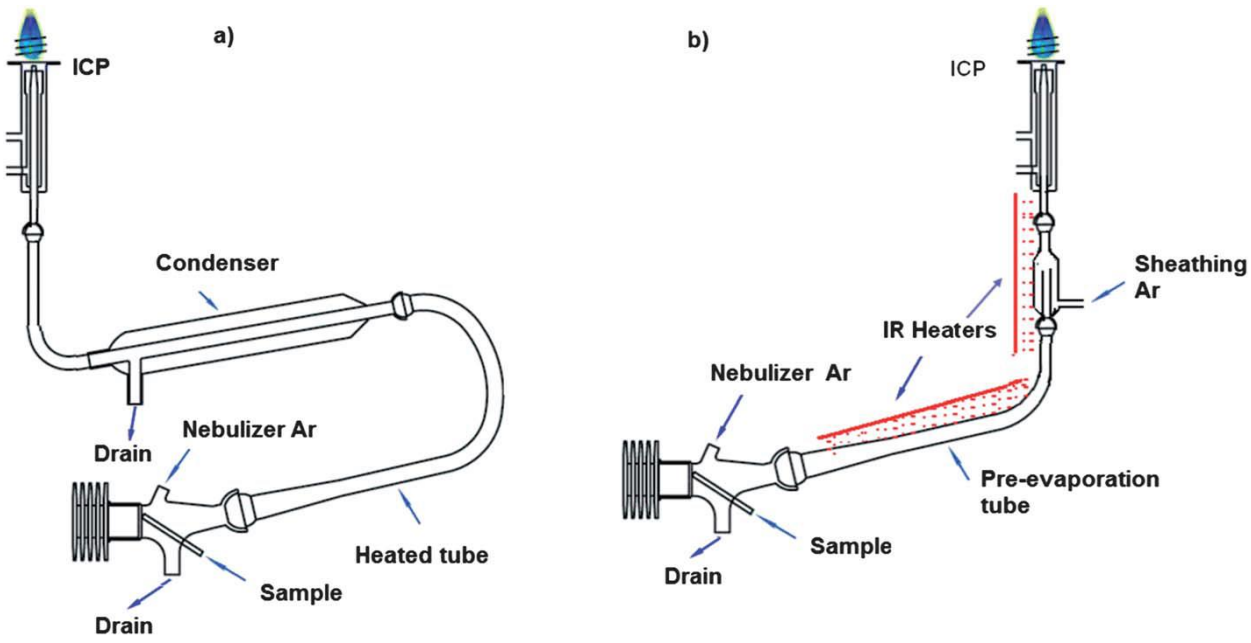

Figure 2.1: Ultrasonic nebuliser with heater and condenser attached (a), and connected to the torch with an IR-heated PET and sheathing device (b). (Reproduced from Ref. 14 with permission from The Royal Society of Chemistry).

For the ARCOS experiments, two 60 mm wide and 245 mm long ceramic IR block heaters (Process Heaters Inc., Toronto, Ontario, Canada) were aligned parallel to the PET, sheathing device and bottom 7 cm of the torch (Fig. 2.2a). The temperature of these heaters was controlled by two PL512 Mantle-Minder temperature controllers (GLAS-COL Apparatus Company), with a thermocouple connected on the inner surface of each heater. A final ARCOS experiment using a rope heater (Marsh Beaded Heaters, Normangee, Texas, US) involved tightly wrapping a heated wire strung with ceramic beads around the PET, sheathing device, and bottom 7 cm of the torch (Fig. 2.2b). A thermocouple was attached to the outer heated portion of the torch (the injector) and the temperature was again controlled by two PL512 Mantle-Minder temperature controllers (GLAS-COL Apparatus Company). Therefore, while the temperature of the heater surface is measured for the block heaters, the temperature of the area under the heater is measured for the rope heater. Since glass is mostly

transparent to infrared radiation, the temperature measured by the thermocouple on the outside of the PET should be fairly similar to the temperature on the inside of the PET to which the aerosol is exposed.

Figure 2.2: USN-PET(IR) setup for SPECTRO ARCOS ICP-OES with block infrared heaters (a) at left, and with a rope infrared heater (b) at right.

A similar setup was used for the Agilent experiments (Fig. 2.3); however, in this case only the bottom 3 cm of the torch was heated, as the Agilent instrument required specialized torches with a plastic casing surrounding the injector. Hence a modified torch was used, in which the bottom 2 cm of plastic casing was cut off so that the exposed quartz could be heated. Additionally, a longer PET and L-shaped glass piece (54 cm total length) were used in place of the 38.1cm long PET. This was due to the deeper horizontal length from the front of the instrument to the torch injector. When attempting to attach the 38.1 cm tube, the USN could not be brought close enough and the angle of the PET provided insufficient connection to the nebuliser. The resulting setup with the 54 cm PET left about 15 cm of PET length unheated.

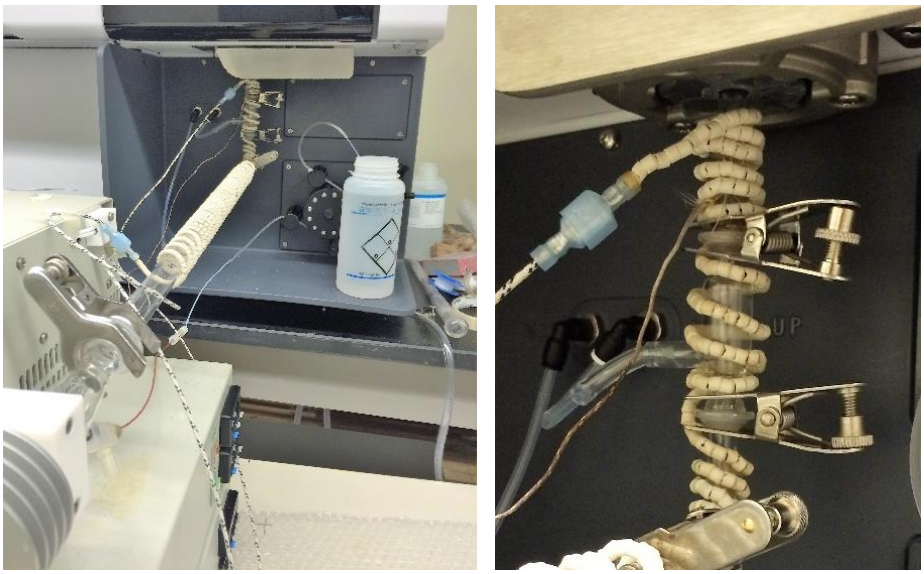

Figure 2.3: USN-PET(IR) setup for Agilent 5100; at left using a long pre-evaporation tube and L-connector (54 cm total); at right, the sheath adaptor and bottom 3 cm of the torch are heated, with thermocouple attached to the lower region of the torch injector.

2.2.3 Reagents and certified reference materials

Standard solutions and samples were prepared with 18 Ω cm^{-1} double deionized water (DDW) (Pro UV/DI, Sartorius Stedim Biotech, Gottingen, Germany) and with HNO_3 (ACS grade; Fisher Scientific, Ottawa, Canada) that was purified prior to use with a DST-1000 Teflon sub-boiling distillation system (Savillex, Minnetonka, USA). 1000 and 10 000 mg L^{-1} mono-elemental plasma standard solutions (SCP Science, Baie d'Urfe, Quebec, Canada) (Bi, Ga, Hg, Eu, Na, In, Se, Li, Y, Ge, Mo, Sb, Si, Ti, Zr, Al, As, Be, Cd, Co, Ce, Cr, Cu, Fe, K, La, Mg, Mn, Ni, P, Pb, S, Sr, V, Zn) were used for the preparation of multi-elemental 100 mg L^{-1} stock solutions with 4% HNO_3. From these, 10 mg L^{-1} stock solutions were made with 2% HNO_3, and more dilute multi-element solutions were prepared daily as calibration standards with corresponding matrix-matched blanks.

Certified reference Waste Water EU-L-3 (SCP Science, Baie d'Urfe, Quebec, Canada) was analyzed directly for method validation, while SRM 8433 Corn Bran (National Institute of Standards and

Technology, Gaithersburg, MD, USA) was digested on a hot plate prior to analysis. About 0.3g of SRM was weighed into a Teflon decomposition vessel (Savillex, Minnetonka, USA) and 2.5 mL HNO_3 and 0.5 mL H_2O_2 (30 wt. % in H_2O, ACS reagent, Sigma-Aldrich, Steinhein, Germany) were added prior to placing the vessel on a hot plate at 50 °C for 2 hours. Digested samples were diluted to 60 mL with DDW, and all standards and blanks for calibration were prepared with matching final acid concentrations.

2.2.4 Optimization

A 100 µg L^{-1} multi-elemental solution was used for multivariate optimizations, in order to find the best compromise conditions in terms of robustness and sensitivity. By monitoring the Mg II 280.270 nm/ Mg I 285.213 nm ratio, operating parameters that provided the most robust conditions were chosen, where a ratio of 10 or above indicated a robust plasma. At such a robustness, changes in matrix composition and solvent loading do not significantly affect plasma excitation. Hence, improved sensitivity and detection limit of analytes can be established. A face-centered central composite design was used for optimisation of aerosol carrier gas flow rate, sheath gas flow rate, sample uptake rate, and IR temperature for ARCOS experiments (Table 2.3). Chosen operating conditions for RF power, plasma gas flow rate, and auxiliary gas flow rate were based on previous optimisations on the same instrument [14].

Table 2.3: Central composite design for optimization of USN-PET(IR) block on ARCOS

Run Order	IR Temperature (°C)	Sample Uptake (mL/min)	Sheath Gas (L/min)	Aerosol Carrier Gas (L/min)
1	300	0.75	0.45	0.3
2	300	0.5	0.4	0.4
3	230	0.75	0.45	0.3
4	160	0.5	0.5	0.2
5	160	0.5	0.4	0.4
6	230	0.75	0.45	0.3
7	230	0.75	0.4	0.3
8	300	0.5	0.5	0.2
9	230	0.75	0.45	0.3
10	160	0.75	0.45	0.3

11	230	0.75	0.45	0.4
12	160	0.5	0.5	0.4
13	230	0.75	0.5	0.3
14	300	1	0.5	0.2
15	160	1	0.4	0.2
16	230	0.75	0.45	0.3
17	230	0.75	0.45	0.3
18	230	0.75	0.45	0.3
19	230	0.75	0.45	0.3
20	160	0.5	0.4	0.2
21	230	1	0.45	0.3
22	230	0.75	0.45	0.2
23	160	1	0.4	0.4
24	230	0.5	0.45	0.3
25	300	1	0.4	0.2
26	160	1	0.5	0.4
27	160	1	0.5	0.2
28	300	1	0.4	0.4
29	300	0.5	0.5	0.4
30	300	1	0.5	0.4
31	300	0.5	0.4	0.2

Optimization of USN-PET(IR) on the Agilent 5100 was separated into two optimisations: aerosol carrier gas flow rate, sheath gas flow rate, sample uptake rate were varied for the first optimization, and IR temperature, auxiliary gas flow rate, plasma gas flow rate, and RF power were adjusted in the second optimization. Comparable optimization experiments were conducted for all PN and USN-HC setups. Following these multivariate optimizations, a univariate optimization of plasma observation height was employed while holding all other operating parameters at their optimum values. The IR temperature was kept at a maximum of 300 °C for ARCOS experiments to create a large enough separation from previous work [14], while the temperature had to be kept below 250 °C for Agilent experiments to prevent melting of the torch casing. Since the rope heater provided both convective and IR heating, the area downstream of the heated region was found to be 30-60 °C higher than the temperature measured by the thermocouple at the base of the torch. Therefore, extra precautions in temperature settings had to be taken to ensure damage to the torch would not occur.

2.2.5 Data Analysis

Minitab 17 Software was used in creating and analyzing experimental designs for multivariate optimizations. Sensitive atomic and ionic emission lines free from possible spectroscopic interference were selected for all 35 elemental analytes. The signals were corrected using two points (one on either side of the emission peak) for polynomial background correction (Smart Analyzer Vision Software, SPECTRO Analytical Instruments, Kleve, Germany) for all ARCOS experiments. On the Agilent instrument, a fitted background correction was selected with 3 pixels read per analyte line (ICP Expert Software, Agilent Technologies, Santa Clara, California, United States). All subsequent data treatments were processed in Microsoft Excel 2013. The signal intensity of the blank was subtracted from that of its corresponding multi-element standard solution or sample to give the net signal intensity for the specified standard or sample. Detection limits for all analytes were calculated as 3 times the standard deviation of the average signal intensity of at least 10 consecutive blanks divided by the slope of the calibration curve (i.e. the sensitivity).

2.3 Results and Discussion

2.3.1 Selection of optimum parameters

For simplicity, the optimization of USN-PET(IR) block on SPECTRO ARCOS will be the major focus in this section. The 300°C and 160°C sets of optimal parameters were both verified by this experiment, but the 300°C set will be discussed in more detail as these parameters provided the best analytical performance. 160°C was chosen as a lower temperature cut off to investigate the effects of heating only minimally above the conventional heater temperature of USN-HC (140°C), and far below the previous and current optimal USN-PET(IR) temperatures (400°C and 300°C, respectively). As expected from the previous work by Asfaw et al. [14], the maximum temperature tested provided the highest signal intensities and Mg II/ Mg I ratio, as the aerosol is vapourized more efficiently at higher temperatures.

This is demonstrated in contour plots (Fig. 2.4) of blank-subtracted signal intensities when sample uptake rate, sheath gas flow rate, aerosol carrier gas flow rate, and IR temperature are varied. While only As 189.042 nm and Mg 280.270 nm/ Mg 285.213nm contour plots are shown, data for all 35 analytes were analyzed for optimization experiments. For all elements, similar contour plot trends were observed, resulting in an easier compromise for optimal settings. This similarity for different elemental analytes agrees with a previous study in which a single sampling depth provided optimal sensitivity for almost all elements in ICP-MS [18]. It is important to note that while the "optimal" conditions often appear at maxima (as the dark green represents the highest values, and the dark blue represents the lowest values in Fig. 2.4), these maxima were often set according to instrument restraints. For instance, the sheath gas flow rate could not be set below 0.4 L/min, resulting in an experimental maximum at this value.

As the previous work lists 12 L min^{-1} and 2.5 L min^{-1} as the optimal plasma and auxiliary gas flow rates, respectively, these values were left unchanged. While the typical default auxiliary gas flow rate for ICP-OES is 1 L min^{-1}, increasing to 2.5 L min^{-1} provided a Mg II/Mg I ratio increase from 11 to 12.6 [14]. Conversely, by decreasing the plasma gas flow rate, analyte intensities and Mg II/ Mg I ratios were found to increase. Additionally, 1400 W was found to be the optimal setting for RF power in Asfaw's work, as a robust plasma is achieved when the RF power is at least 1400 W [19], and higher RF power increases robustness [20]. RF power was kept the same in order to have an unbiased comparison of robustness between the previous 400°C experiment and the new experimental setups.

In order to increase the residence time of the aerosol on the membrane of the ultrasonic nebuliser, and therefore improve precision, a sheathing device was used to allow for a lower aerosol carrier gas flow rate. Hence, aerosol and vapour could be pushed through the PET by a low flow aerosol carrier gas, and then given an extra push by the sheath gas to sweep it into the ICP. Optimal values for sheath gas flow rate and aerosol carrier gas flow rate were found to be 0.4 and 0.33 L min^{-1},

respectively. With a total central gas (aerosol carrier gas + sheath gas) of 0.73 L min^{-1}, the results are in agreement with reports of Grotti et al. [21] who found that both the Mg II/ Mg I ratio and excitation temperature increase with a carrier gas flow rate increase of up to 0.7 – 0.85 L min^{-1} (depending on the RF power), but decrease past this point.

In comparison with Asfaw's work, a decreased sample uptake rate of 0.8 mL min^{-1} was found to provide optimal signal intensity and robustness (Fig. 2.4) versus the 1.5 mL min^{-1} sample uptake rate previously used. With a decreased temperature, a lower sample uptake rate is required to ensure all sample aerosol is vaporized in the PET. This trend is also observed in the 160°C experiment, whereby a 0.5 mL min^{-1} sample uptake rate was optimal. Increasing the sample uptake rate much higher than this would result in a buildup of un-vaporized sample and condensation at the base of the torch, which would inevitably extinguish the plasma.

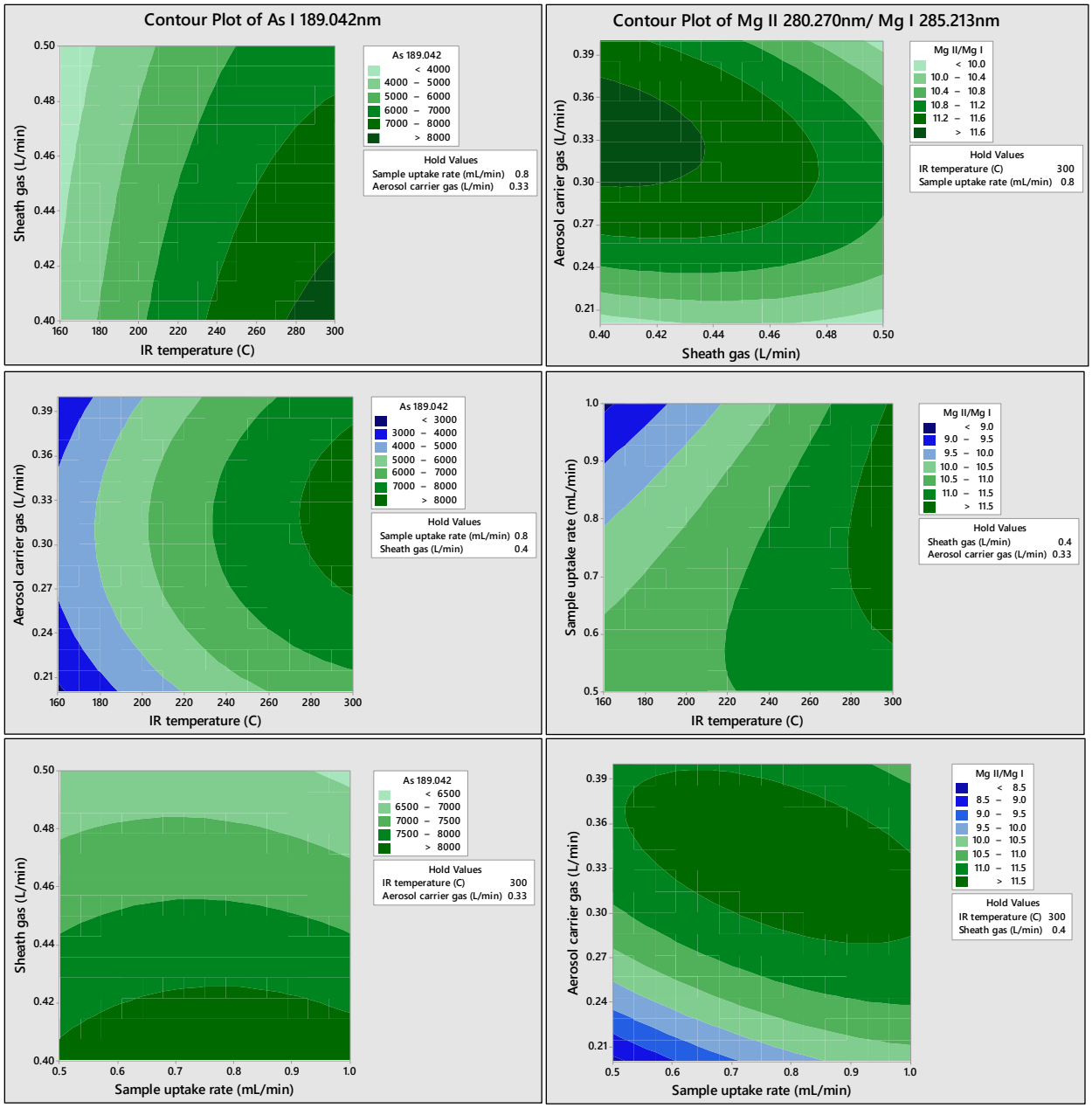

Figure 2.4: Contour plots for the multivariate optimization of USN-PET(IR) block at 300°C on SPECTRO ARCOS. Values are held in order to find the optimal compromised conditions for two other parameters. At left, blank subtracted As 189.042nm emission intensities are shown. At right, Mg 280.270nm and 285.213nm emission intensities have been blank subtracted, with the ratio providing an indication of robustness.

The plasma observation height was kept constant throughout the ARCOS experiments, being set to 11 mm above the load coil. This was based on previous work on the same instrument [14, 15]. The plasma observation height was optimized for lateral view on the Agilent instrument by holding all other

conditions at their optimum values and measuring signal intensities as the reading for the detector was directed deeper into the plasma. The optimal plasma observation height was found to be 6 mm for USN-PET(IR) and 1 mm for USN-HC.

2.3.2 Sensitivity, detection limit, and precision

Tables 2.4-2.7 provide examples of the sensitivities and detection limits, as well as factors of improvements for the various setups involved in this work. Sensitivity, the slope of the calibration curve, and detection limit, which is calculated as 3 times the standard deviation of 10 replicates of the blank signal divided by the sensitivity, are shown to improve when using USN-HC over PN. This is expected as the average droplet size is reduced and the analyte is pre-concentrated in the heater/condenser. By replacing the HC with a heated PET, there is further improvement in detection capabilities as aerosol droplets can be vapourized (reducing noise caused by large droplets), but the important plasma benefits from water as a load buffer are not lost from solvent removal. Thereby, on the SPECTRO instrument, we see an average factor of improvement in sensitivity when using USN-PET(IR) block at 300 °C of 4.0 ± 1.4, **3.5 ± 1.4** when compared to PN, and of 3.5 ± 5.3, **3.0 ± 1.8** when compared to USN-HC. Here, the average of a set of 20 atomic lines is given first, and the average of 20 ionic lines is given second in bold. In comparing detection limits, these ratios are 2.2 ± 2.4, **1.9 ± 1.9** and 0.9 ± 2.0, **0.8 ± 1.3** when this USN-PET setup is compared to PN and USN-HC, respectively.

On the Agilent instrument, the average improvement in sensitivity is 2.6 ± 0.5 (6.3 ± 2.6), **2.4 ± 0.8 (6.2 ± 3.5)** when compared to PN and 0.8 ± 0.8 (0.6 ± 0.8), **0.6 ± 0.1 (0.46 ± 0.05)** when compared to USN-HC on the same instrument, where lateral view values are listed first and axial view values are given in brackets. In terms of detection limits, the average factor of improvement was 2.1 ± 1.0 (3.4 ± 2.7), **2.6 ± 1.2 (3.4 ± 3.5)** and 0.6 ± 0.2 (0.5 ± 0.3), **0.6 ± 0.2 (0.4 ± 0.2)** compared to PN and USN-HC, respectively. Ratio values less than 1 (as in the case of Agilent USN-PET compared to USN-HC) show that the analytical

performance was degraded with the USN-PET(IR) setup. Since the rope heater did not cover the entire length of the long PET, leaving 15 cm of unheated tube length, the system was less efficient than a conventional setup. By increasing the tube length, sticky elements such as Hg had more surface area to cling to, resulting in lower sensitivities. Additionally, condensation and accumulation of sample would occur at the connection between the PET and the spray chamber, due to the drastic temperature difference between this location and the heated area further up the PET. Since the USN could be placed closer to the ICP-OES instrument and the angle of the PET to the torch did not cause problems in connection, the shorter 38.1 cm PET could be used in all USN-PET(IR) experiments on the ARCOS instrument. Therefore when comparing USN-PET(IR) rope methods between Agilent and ARCOS, it is important to note that only the Agilent setup has an unheated length of PET. Furthermore, due to the plastic casing on the Agilent torches, only 3 cm of the torch injector was heated for the Agilent setup, while 7 cm of torch injector was heated on the ARCOS setup. The pre-evaporated sample would therefore rapidly cool in the remainder of the torch injector length prior to entering the plasma, resulting in a decrease in pre-evaporation effectiveness. Comparing USN-PET(IR) rope on ARCOS to USN-PET(IR) rope on Agilent, sensitivity increases on average by a factor of 34 ± 21 (12 ± 10), **23 ± 20 (6.6 ± 4.5)** when using the ARCOS setup, and the average detection limit increases by a factor of 8.4 ± 17.8 (3.5 ± 8.0), **1.6 ± 1.7 (1.2 ± 2.2)**. As expected, the ARCOS setup provides better detection capabilities, even when compared to the axial view. Typically, axial view provides lower detection limits than lateral, while lateral view is more robust [6]. Axial view takes the measurement from a longer path through the central channel of the plasma, while lateral view measures a horizontal slice of the plasma, which includes both the bulk of the plasma and the central channel. By looking through the bulk of the plasma, or buffer zone, matrix effects are minimized; however, by looking down into the plasma, background signal and matrix effects are exacerbated. Despite each of these three methods being set to 250 °C, the method on the ARCOS has the advantage of a shorter PET, allowing for heating all along its length.

To compare the effects of heating temperature and method of IR heating (i.e. block heaters vs. rope heaters), USN-PET(IR) on ARCOS was conducted at 300 °C and 160 °C with block heaters and at 250 °C with a rope heater. Heating at 300 °C instead of 160 °C resulted in average improvement factors of 2.2 ± 1.5, **3.5 ± 1.8** for sensitivity and 2.8 ± 1.5, **3.7 ± 2.4** for detection limit. Unsurprisingly, heating to 160 °C was not as efficient at vaporizing the aerosol and therefore resulted in lower sensitivities and higher detection limits. Heating at 300 °C with block heaters instead of 250 °C with the rope heater resulted in average improvement ratios of 1.4 ± 0.3, **1.3 ± 0.4** for sensitivity and 3.1 ± 4.8, **1.7 ± 1.2** for detection limit. This average improvement in analytical capabilities highlights the benefits of the uniformity of pure IR heating. Since rope heaters use both convective and infrared heating, the homogeneity of heating intensity along the PET may be affected, disrupting the effectiveness of pre-evaporation. Although the block heaters were set 50 °C higher than the rope heater, it is unlikely that this temperature difference is the cause of a different analytical performance. Since the area downstream of the rope heater is actually 30-60 °C higher than that measured by the thermocouple, the true temperature used for pre-evaporation may in fact be the same for both heater types.

Due to the large range in factors of improvement for different elements, the above averages may not give the clearest picture when comparing ionic and atomic lines. Since compromise operating conditions were used for each setup, some elements would see a degradation in performance while others saw an enhancement. Rather than comparing as averages, improvements in analytical performance are more apparent when comparing the atomic and ionic lines element-by-element. Generally speaking, sensitivity enhancements are greater for ionic lines than atomic lines, due to lines with a higher total excitation potential (TEP) being more sensitive to changes in the ICP's excitation conditions [22, 23]. For instance, the factors of improvement for detection limit when using recommended ionic lines over recommended atomic lines for Al, Be, Hg, and Mg are 120, 22, 8.7, and 4.2, respectively, when comparing USN-PET(IR) at 300 °C to USN-HC on the ARCOS. In terms of

sensitivity, these ratios of improvement are 7.1, 2.7, 2.0, and 3.1, for Al, Be, Hg, and Mg. In another comparison when ionic lines, rather than atomic are used, there is a factor of improvement for detection limit of 31 (45), 6.6 (4.6), 2.3 (3.4), and 1.6 (3.0) for Al, Cu, In, and Mg, respectively, when comparing USN-PET(IR) rope on ARCOS to USN-PET(IR) rope on Agilent. Again, lateral view results on the Agilent and ARCOS instruments are given first, while the axial view results for Agilent are compared to lateral view results on the ARCOS secondly, in brackets. In terms of sensitivity, these ratios are 0.67 (2.3) for Al, 3.9 (2.8) for Cu, 1.2 (1.6) for In, and 1.3 (1.5) for Mg. This comparison highlights the fact that axial view ionic lines had a greater factor of improvement over atomic lines than the corresponding lines in lateral view.

Finally, USN-PET(IR) block at 300 °C is compared to the previous work of heating USN-PET(IR) block to 400 °C [14]. As fewer lines are provided in Asfaw's work, comparisons are made as overall averages from Tables 2.5 and 2.7, rather than separate averages for atomic and ionic lines. With an average sensitivity factor of improvement with the 300 °C method of 1.0 ± 0.5 and an average detection limit ratio of 0.8 ± 1.8, it would appear that 400 °C is slightly more effective at pre-evaporation than 300 °C. Put another way, these ratios of improvement for Asfaw's method are 1.5 ± 2.4 for sensitivity, and 5.1 ± 5.7 for detection limit; however, this analysis is without normalization of the sample uptake rate. Hence, it can be asserted that the 300 °C method provides nearly the same sensitivities and detection limits as the previous work, but with a more efficient system (i.e. the IR temperature is reduced by 100 °C and the sample uptake rate is nearly halved).

Instrumental precisions, represented as % relative standard deviation (RSD) of 10 replicates of a 100 ppb multi-element standard, are listed in Table 2.8. While USN-PET(IR) at 400 °C had an average RSD of 1.3 ± 0.7%, USN-PET(IR) at 160 °C had a greater RSD of 3.2 ± 6.6%, and USN-PET(IR) at 300 °C had an even larger RSD of 4.3 ± 3.9%, according to values listed in Table 2.8. USN-HC had a comparable RSD to the rope heater experiments, with average values of 2.2 ± 2.2%, 2.4 ± 1.4%, 3.3 ± 1.6% (1.4 ± 0.6%)

and 3.5 ± 3.2% (2.3 ± 1.5%), for ARCOS USN-HC, ARCOS USN-PET(IR) rope 250 °C, Agilent USN-HC, and Agilent USN-PET(IR) rope, respectively.

Table 2.4: Sensitivity (cps per ng mL^{-1}) for USN and Conventional Setups

	A	B	C	D	E	F	G	H	I	J	K	L
Element Line (nm)	**PN (ARCOS)**	**PN Lateral (Agilent)**	**PN Axial (Agilent)**	**USN-HC (ARCOS)**	**USN-HC Lateral (Agilent)**	**USN-HC Axial (Agilent)**	**USN-PET(IR) Lateral rope (Agilent)**	**USN-PET(IR) Axial rope (Agilent)**	**USN-PET(IR) 400°C [14] Block (ARCOS)**	**USN-PET(IR) 300° C block (ARCOS)**	**USN-PET(IR) 160° C block (ARCOS)**	**USN-PET(IR) 250° C rope (ARCOS)**
Al II 167.019	160	3.4	0.57	12	24	20	9	10	930	69	10	130
As I 189.042	16	0.49	0.42	29	2	6.4	1.1	3.4	100	100	22	57
Be II 313.042	8900	1200	1100	7200	5300	15000	3400	7000	12000	33000	7800	25000
Bi I 223.061	11	0.46	0.84	29	1.8	10	1.1	4.3	40	---	---	31
Cd II 214.439	410	12	12	270	57	200	24	110	2800	2100	320	1400
Co II 228.615	310	6.9	9	1000	30	120	15	59	830	1300	380	920
Cr II 267.716	84	11	15	130	47	190	25	87	420	360	73	270
Cu II 224.700	47	0.74	0.95	100	3.2	12	1.5	6.3	230	230	97	130
Cu I 324.754	230	8.2	20	580	31	170	24	75	510	610	250	560
Eu II 420.505	750	72	190	2400	260	1500	210	580	---	2100	1700	2500
Fe II 238.204	210	13	17	250	58	230	29	110	960	840	220	520
Ga I 294.364	19	2	4.3	45	7.5	42	4.8	18	---	52	130	49
Ge I 265.117	11	0.28	0.59	26	1.1	7.1	0.68	2.9	50	---	---	32
Hg I 184.887	95	3.7	3	170	23	64	16	32	150	130	50	110
In II 230.606	7.9	0.51	0.83	13	2.1	11	1.2	4.5	---	26	75	20
K I 766.491	0.17	1.4	38	51	1.8	150	1.3	22	40	37	17	77
La II 408.672	280	22	55	700	88	460	63	190	---	870	1100	960
Li I 670.783	160	83	2000	830	330	21000	270	5100	380	490	540	520
Mg II 280.270	1400	55	72	1800	260	1000	130	440	6300	7000	1500	4300
Mg I 285.213	180	6.1	15	430	25	160	16	62	480	540	230	390
Mn II 257.610	610	57	76	760	240	1000	140	460	2400	2100	470	1400
Mo II 202.032	65	2.6	3.3	77	11	45	5.7	21	300	250	53	160
Ni II 231.604	81	1.8	2.4	120	8.1	31	3.9	16	500	390	69	280
P I 177.434	11	0.38	0.18	9	1.9	4	1	2	70	42	8	32

Pb II 220.353	16	1.2	1.6	25	5.3	22	2.1	12	---	84	15	48
S I 180.669	13	0.17	0.11	18	0.56	1.4	0.44	0.81	90	59	27	36
Sb I 217.582	11	0.26	0.42	20	0.94	4.9	0.61	2.4	60	39	55	29
Se I 196.026	9.6	0.49	0.47	1.7	2	6.9	1.3	3.9	50	42	8.7	30
Si I 251.611	44	1	1.7	140	1.5	5.6	1	3.1	160	160	50	140
Sr II 421.552	5400	550	1300	17000	2200	12000	1600	4600	11000	17000	7200	18000
Ti II 334.941	580	81	140	890	330	1400	210	610	1800	1900	710	1300
V II 292.464	740	68	100	140	31	140	19	62	350	300	73	240
Y II 371.029	1700	35	78	4800	150	800	94	320	6400	6600	2800	6200
Zn II 206.200	260	1.7	1.6	1370	8.1	25	3.3	14	1400	2200	340	1600
Zn I 213.857	360	14	16	1100	58	240	34	120	1600	1500	340	1700
Zr II 339.198	300	17	32	580	70	360	42	150	1100	1200	560	830

Table 2.5: Sensitivity Ratios for USN and Conventional Setups

Element Line (nm)	I/A	J/A	L/A	J/D	L/D	J/I	G/B	H/C	G/E	H/F
Al II 167.019	5.8	0.43	0.78	5.9	11	0.074	2.7	18	0.37	0.52
As I 189.042	6.2	6.3	3.5	3.5	1.9	1	2.2	8	0.53	0.53
Be II 313.042	1.3	3.7	2.9	4.6	3.5	2.8	2.8	6.4	0.64	0.47
Bi I 223.061	3.6	---	2.8	---	1.1	---	2.3	5.1	0.59	0.43
Cd II 214.439	6.9	5.3	3.4	8	5.2	0.77	1.9	8.8	0.42	0.55
Co II 228.615	2.6	4.2	2.9	1.2	0.87	1.6	2.2	6.5	0.51	0.49
Cr II 267.716	5	4.3	3.2	2.8	2.1	0.85	2.2	5.6	0.54	0.46
Cu II 224.700	4.9	4.9	2.8	2.2	1.3	0.99	2	6.6	0.46	0.52
Cu I 324.754	2.2	2.7	2.4	1.1	0.96	1.2	2.9	3.8	0.78	0.43
Eu II 420.505	---	2.8	3.3	0.9	1.1	---	2.9	3	0.81	0.38
Fe II 238.204	4.5	4	2.5	3.4	2.1	0.88	2.2	6.2	0.5	0.47
Ga I 294.364	---	2.8	2.6	1.2	1.1	---	2.4	4.2	0.64	0.43
Ge I 265.117	4.4	---	2.9	---	1.3	---	2.4	4.8	0.61	0.41
Hg I 184.887	1.6	1.4	1.1	0.76	0.63	0.86	4.3	11	0.68	0.5
In II 230.606	---	3.3	2.5	2	1.5	---	2.3	5.4	0.57	0.41
K I 766.491	240	230	470	0.74	1.5	0.93	0.89	0.59	0.68	0.15

La II 408.672	---	3.1	3.4	1.2	1.4	---	2.8	3.4	0.72	0.41
Li I 670.783	2.4	3.1	3.2	0.6	0.63	1.3	3.3	2.6	0.82	0.24
Mg II 280.270	4.5	5.1	3.1	4	2.4	1.1	2.4	6.1	0.5	0.43
Mg I 285.213	2.7	3.1	2.2	1.3	0.91	1.1	2.6	4.3	0.62	0.38
Mn II 257.610	3.9	3.4	2.3	2.8	1.9	0.87	2.4	6	0.56	0.45
Mo II 202.032	4.6	3.8	2.5	3.2	2.1	0.83	2.2	6.4	0.52	0.47
Ni II 231.604	6.2	4.8	3.5	3.2	2.4	0.77	2.1	6.8	0.49	0.51
P I 177.434	6.3	3.8	2.8	4.7	3.5	0.6	2.7	11	0.54	0.5
Pb II 220.353	---	5.4	3.1	3.4	1.9	---	1.8	7	0.4	0.53
S I 180.669	7.1	4.7	2.9	3.3	2.1	0.66	2.5	7.4	0.78	0.57
Sb I 217.582	5.5	3.5	2.6	1.9	1.4	0.65	2.3	5.6	0.64	0.48
Se I 196.026	5.2	4.4	3.1	24	17	0.83	2.7	8.2	0.67	0.57
Si I 251.611	3.6	3.6	3.3	1.1	1	1	0.96	1.8	0.69	0.55
Sr II 421.552	2.1	3.2	3.3	1	1.1	1.5	2.9	3.4	0.74	0.39
Ti II 334.941	3.2	3.4	2.3	2.2	1.5	1.1	2.6	4.3	0.65	0.42
V II 292.464	0.47	0.4	0.33	2.1	1.7	0.85	0.28	0.59	0.6	0.44
Y II 371.029	3.7	3.8	3.6	1.4	1.3	1	2.7	4.1	0.62	0.4
Zn II 206.200	5.3	8.6	6.1	1.6	1.2	1.6	1.9	8.8	0.4	0.57
Zn I 213.857	4.5	4.1	4.8	1.3	1.5	0.91	2.3	7.1	0.58	0.48
Zr II 339.198	3.7	4.1	2.8	2.1	1.4	1.1	2.5	4.6	0.6	0.42

Table 2.6: Detection Limits (ng/mL) for USN and Conventional setups

Ratio Label	A	B	C	D	E	F	G	H	I	J	K	L
Element Line (nm)	PN (ARCOS)	PN Lateral (Agilent)	PN Axial (Agilent)	USN-HC (ARCOS)	USN-HC Lateral (Agilent)	USN-HC Axial (Agilent)	USN-PET(IR) Lateral rope (Agilent)	USN-PET(IR) Axial rope (Agilent)	USN-PET(IR) 400°C [14] Block (ARCOS)	USN-PET(IR) 300° C block (ARCOS)	USN-PET(IR) 160° C block (ARCOS)	USN-PET(IR) 250° C rope (ARCOS)
Al II 167.019	0.2	7	20	3	0.4	1	2	1	0.07	0.5	3	0.4
As I 189.042	7	30	50	0.9	10	3	20	9	1	0.9	3	2
Be II 313.042	0.09	0.1	0.06	0.04	0.008	0.02	0.02	0.6	0.01	0.01	0.08	0.06
Bi I 223.061	10	60	30	2	10	2	20	4	4	---	---	10
Cd II 214.439	0.4	0.6	2	0.2	0.3	0.1	0.6	0.3	0.05	0.1	0.2	0.2
Co II 228.615	1	8	3	0.2	1	0.4	3	0.4	0.2	0.3	2	1
Cr II 267.716	1	3	2	0.2	0.5	0.1	0.8	0.4	0.3	0.5	1	1
Cu II 224.700	2	20	7	0.3	5	0.7	10	2	0.6	3	10	2
Cu I 324.754	3	4	2	0.1	1	0.2	2	0.4	0.3	0.5	1	3
Eu II 420.505	2	1	0.4	0.2	0.5	0.09	0.6	0.2	---	4	6	3
Fe II 238.204	0.7	3	2	0.1	0.5	0.2	1	0.5	0.2	1	3	1
Ga I 294.364	10	20	7	2	10	1	20	3	---	20	10	20
Ge I 265.117	8	50	30	1	20	2	30	10	2	---	---	7
Hg I 184.887	0.6	4	6	0.1	2	1	4	3	0.6	2	7	1
In II 230.606	20	70	20	4	20	5	30	10	---	40	10	20
K I 766.491	4000	200	4	8	100	0.7	---	10	3	20	40	30
La II 408.672	7	4	1	1	0.9	0.2	1	0.5	---	10	10	8
Li I 670.783	3	10	0.1	0.4	3	0.02	4	0.7	0.4	3	7	4
Mg II 280.270	0.5	0.3	0.1	0.03	0.1	0.02	0.2	0.09	0.03	0.08	0.8	0.05
Mg I 285.213	0.6	7	1	0.09	1	0.1	2	0.5	0.2	1	5	0.8
Mn II 257.610	0.2	1	0.3	0.06	0.2	0.03	0.3	0.1	0.04	0.07	0.1	0.2
Mo II 202.032	2	10	9	0.4	3	1	5	2	0.4	0.3	1	1
Ni II 231.604	2	20	5	0.5	4	0.9	7	1	0.2	0.9	2	2
P I 177.434	3	60	90	3	5	3	20	10	1	2	4	30

Pb II 220.353	7	20	6	2	6	0.6	10	3	---	4	4	7
S I 180.669	5	100	70	3	40	20	60	40	1	3	10	1
Sb I 217.582	10	50	30	2	20	4	30	10	1	10	20	7
Se I 196.026	10	30	20	10	8	5	30	4	10	1	7	6
Si I 251.611	3	30	20	0.4	6	2	20	6	1	1	3	8
Sr II 421.552	0.3	0.2	0.06	0.04	0.1	0.01	0.1	0.02	0.02	0.5	2	0.4
Ti II 334.941	1	2	0.3	0.4	0.2	0.07	0.4	0.2	0.06	0.6	3	3
V II 292.464	0.3	1	0.3	0.5	2	0.3	4	1	0.5	0.8	2	3
Y II 371.029	0.9	0.9	0.3	0.1	0.2	0.05	0.4	0.1	0.05	1	4	1
Zn II 206.200	0.8	8	10	0.2	2	0.9	5	0.7	0.06	0.3	3	0.2
Zn I 213.857	0.3	2	2	0.2	0.2	0.2	0.6	0.3	0.09	0.2	0.4	0.2
Zr II 339.198	2	5	0.7	0.2	1	0.09	1	0.2	0.1	1	6	2

Table 2.7: Detection Limit Ratios for USN and Conventional Setups

Element Line (nm)	A/I	A/J	A/L	D/J	D/L	I/J	B/G	C/H	E/G	F/H
Al II 167.019	2.9	0.4	0.5	6	7.5	0.14	3.5	20	0.2	1
As I 189.042	7	7.8	3.5	1	0.45	1.1	1.5	5.6	0.5	0.33
Be II 313.042	9	9	1.5	4	0.67	1	5	0.1	0.4	0.033
Bi I 223.061	2.5	---	1	---	0.2	---	3	7.5	0.5	0.5
Cd II 214.439	8	4	2	2	1	0.5	1	6.7	0.5	0.33
Co II 228.615	5	3.3	1	0.67	0.2	0.67	2.7	7.5	0.33	1
Cr II 267.716	3.3	2	1	0.4	0.2	0.6	3.8	5	0.63	0.25
Cu II 224.700	3.3	0.67	1	0.1	0.15	0.2	2	3.5	0.5	0.35
Cu I 324.754	10	6	1	0.2	0.033	0.6	2	5	0.5	0.5
Eu II 420.505	---	0.6	0.69	0.062	0.072	---	1.7	2.3	0.75	0.59
Fe II 238.204	3.5	0.7	0.7	0.1	0.1	0.2	3	4	0.5	0.4
Ga I 294.364	---	0.72	0.73	0.094	0.095	---	1.3	2.2	0.57	0.35
Ge I 265.117	4	---	1.1	---	0.14	---	1.7	3	0.67	0.2

Hg I 184.887	1	0.3	0.6	0.05	0.1	0.3	1	2	0.5	0.33
In II 230.606	---	0.62	0.95	0.12	0.18	---	2.6	1.1	0.74	0.38
K I 766.491	1300	200	130	0.4	0.27	0.15	---	0.4	---	0.07
La II 408.672	---	0.58	0.78	0.086	0.12	---	3.3	1.9	0.86	0.4
Li I 670.783	7.5	1	0.75	0.13	0.1	0.13	2.5	0.14	0.75	0.029
Mg II 280.270	17	6.3	10	0.38	0.6	0.38	1.5	1.1	0.5	0.22
Mg I 285.213	3	0.6	0.75	0.09	0.11	0.2	3.5	2	0.5	0.2
Mn II 257.610	5	2.9	1	0.86	0.3	0.57	3.3	3	0.67	0.3
Mo II 202.032	5	6.7	2	1.3	0.4	1.3	2	4.5	0.6	0.5
Ni II 231.604	10	2.2	1	0.56	0.25	0.22	2.9	5	0.57	0.9
P I 177.434	3	1.5	0.1	1.5	0.1	0.5	3	9	0.25	0.3
Pb II 220.353	---	1.8	1	0.5	0.29	---	2	2	0.6	0.2
S I 180.669	5	1.7	5	1	3	0.33	1.7	1.8	0.67	0.5
Sb I 217.582	10	1	1.4	0.2	0.29	0.1	1.7	3	0.67	0.4
Se I 196.026	1	10	1.7	10	1.7	10	1	5	0.27	1.3
Si I 251.611	3	3	0.38	0.4	0.05	1	1.5	3.3	0.3	0.33
Sr II 421.552	15	0.6	0.75	0.08	0.1	0.04	2	3	1	0.5
Ti II 334.941	17	1.7	0.33	0.67	0.13	0.1	5	1.5	0.5	0.35
V II 292.464	0.6	0.38	0.1	0.63	0.17	0.63	0.25	0.3	0.5	0.3
Y II 371.029	18	0.9	0.9	0.1	0.1	0.05	2.3	3	0.5	0.5
Zn II 206.200	13	2.7	4	0.67	1	0.2	1.6	14	0.4	1.3
Zn I 213.857	3.3	1.5	1.5	1	1	0.45	3.3	6.7	0.33	0.67
Zr II 339.198	20	2	1	0.2	0.1	0.1	5	3.5	1	0.45

Table 2.8: Instrumental precision (% relative standard deviation for 100ppb, n=10) for USN and Conventional Setups

Element Line (nm)	PN (ARCOS)	PN Lateral (Agilent)	PN Axial (Agilent)	USN-HC (ARCOS)	USN-HC Lateral (Agilent)	USN-HC Axial (Agilent)	USN-PET(IR) Lateral Rope (Agilent)	USN-PET(IR) Axial Rope (Agilent)	USN-PET(IR) 400°C [14] Block (ARCOS)	USN-PET(IR) 300° C Block (ARCOS)	USN-PET(IR) 160° C Block (ARCOS)	USN-PET(IR) 250° C Rope (ARCOS)
Al II 167.019	1	1.7	1.4	1.1	2	1.4	2.3	1.2	1.4	6.9	0.9	3.1
As I 189.042	0.5	2	1.5	0.88	7.4	1.8	5.8	1.8	1.4	4.9	1.6	1.1
Be II 313.042	1.3	0.87	0.41	3.2	3	0.92	1.7	1.7	0.7	4.7	2	4.7
Bi I 223.061	0.49	7	3.7	0.62	8.6	1.9	7.5	9.4	1.6	---	---	0.6
Cd II 214.439	0.8	0.85	0.7	2.5	2.8	0.81	1.8	2.2	0.3	4.3	2.8	4.8
Co II 228.615	0.53	0.32	0.61	1.8	2.6	1.6	3.1	2.2	2.4	4.1	3	2.2
Cr II 267.716	0.73	1.3	1.4	1.8	2.2	0.83	2	1.7	1.7	3.9	3.4	2
Cu II 224.700	0.63	0.83	1.2	1.6	2.4	0.92	2.4	1.4	2	3.4	1.6	1.5
Cu I 324.754	0.54	1.5	0.98	1.5	2.5	1.1	1.8	1.2	1.4	3.3	2.2	1.8
Eu II 420.505	0.6	0.8	1.4	3	1.7	1.8	1.6	1.6	---	2.6	1.3	3.6
Fe II 238.204	0.73	0.7	0.54	1.8	2.1	0.79	2.6	1.3	2.1	3.6	2.2	2.3
Ga I 294.364	0.61	2.4	1.2	0.5	3.2	0.72	3.8	1.9	---	2.2	2.3	2
Ge I 265.117	0.46	5	1.3	0.79	5.7	2	8.7	4	1.3	---	---	0.7
Hg I 184.887	2.2	5.3	6	3.6	1.7	0.62	2.2	2.6	1.7	3.2	1.5	6.2
In II 230.606	0.42	5.8	2.2	0.38	5.8	1.5	15	1.5	---	2.7	2.3	2.3
K I 766.491	0.72	1.3	1.5	0.71	3.9	1.1	11	4	1.9	26	40	2.9

La II 408.672	0.5	0.78	0.78	2.1	3.2	2	1.6	1.5	---	2.4	1.7	2.5
Li I 670.783	0.49	1	0.35	0.83	1.9	2	1.3	1.4	1.6	2.4	1.7	2
Mg II 280.270	0.67	0.52	0.29	3.6	2.8	1.2	1.6	1.5	0.2	4	1.8	4.9
Mg I 285.213	0.45	0.57	0.73	1.3	2.6	0.83	1.4	1.7	1.5	3	1.7	2.4
Mn II 257.610	0.62	0.52	0.91	2.1	2.6	0.89	2.3	2.3	0.7	3.7	2.1	4.7
Mo II 202.032	0.83	0.79	0.8	0.86	2.5	1.8	1.6	2.7	1.8	4.1	1.2	2.3
Ni II 231.604	0.74	0.92	0.84	1.7	2.6	0.86	3.2	1.7	1.8	4.3	3.2	2
P I 177.434	0.69	2	4.4	1.9	3.8	2.6	2.9	2.7	2.1	3.4	2.6	1.2
Pb II 220.353	0.99	2	0.96	0.86	1.4	0.77	3.7	1.4	---	4	2.2	0.72
S I 180.669	0.73	3.7	3.7	0.79	5.4	2.6	8.3	3.2	1.8	2.2	1.7	0.92
Sb I 217.582	0.41	4.7	2.2	0.46	4.5	2.8	8.5	4.3	1.4	3	1.4	0.78
Se I 196.026	0.55	2.5	1.5	1.9	5.9	1.3	2.5	4.7	2.1	5.6	1.4	0.62
Si I 251.611	0.63	1.4	0.82	1.5	3.7	0.49	2.3	1.1	2	3.2	3.3	1.4
Sr II 421.552	1.4	1.3	0.65	3	2.6	1.6	1.4	1.3	0.2	3.8	1.3	3.7
Ti II 334.941	0.7	0.65	1.2	2	2.8	1.6	1.3	1.6	1	3.3	1.7	4.4
V II 292.464	0.63	0.57	1	1.7	3	0.81	1.8	2.1	1.6	3.7	3.9	1.4
Y II 371.029	0.81	0.56	0.47	3.2	2.5	1.1	1.5	1.5	0.9	3.2	1.2	4.4
Zn II 206.200	0.6	0.74	0.69	11	2.5	1.3	3.3	1.6	0.8	4.3	2.9	2.1
Zn I 213.857	0.56	0.64	0.69	10	2.1	1	1.5	2.3	0.2	3.6	2.1	2.1
Zr II 339.198	0.55	0.54	0.33	2	2.6	1.2	1	1.7	0.2	2.9	1.8	2

2.3.3 Plasma robustness

Robustness, represented by the Mg 280.270 nm/285.213 nm ratio is compared for the current experimental setups in Fig. 2.5. Asfaw's USN-PET(IR) at 400 °C had a Mg ratio of 13.0 ± 0.3, which is comparable to the USN-PET(IR) 300 °C ratio of 12.3 ± 0.5. A robust plasma is defined by Mermet as one with a Mg II/ Mg I ratio of at least 10 [19], where Mg is chosen as the test element due to the close excitation energies of the atomic and ionic line which simplifies the second exponential of the Saha equation, and because both lines are highly sensitive to parameter changes. Only USN-PET(IR) at 300 and 400 °C, in addition to the lateral USN-HC setup on Agilent (Mg ratio of 10.23 ± 0.03), can be classified as robust. USN-HC on Agilent in axial view, and USN-HC on ARCOS had the lowest Mg ratios at 6.6 ± 0.1 and 4.0 ± 0.1, respectively. The USN-PET(IR) rope experiments on Agilent had robustness values of 8.7 ± 0.3 for lateral view and 7.10 ± 0.04 for axial view. This value was much closer to 10 for the rope experiment on ARCOS which had a Mg ratio of 9.4 ± 0.2, with the improvement from Agilent likely being due to the minimization of potential air-leaks via less connections compared to the Agilent USN-PET setup, in addition to more efficient heating along the PET, and the shorter distance from the spray chamber to the torch. The USN-PET(IR) 160 °C experiment had a Mg ratio of 8.9 ± 0.6, indicating the impact a lower pre-evaporation temperature can have on robustness (i.e. 300 °C vs. 160 °C).

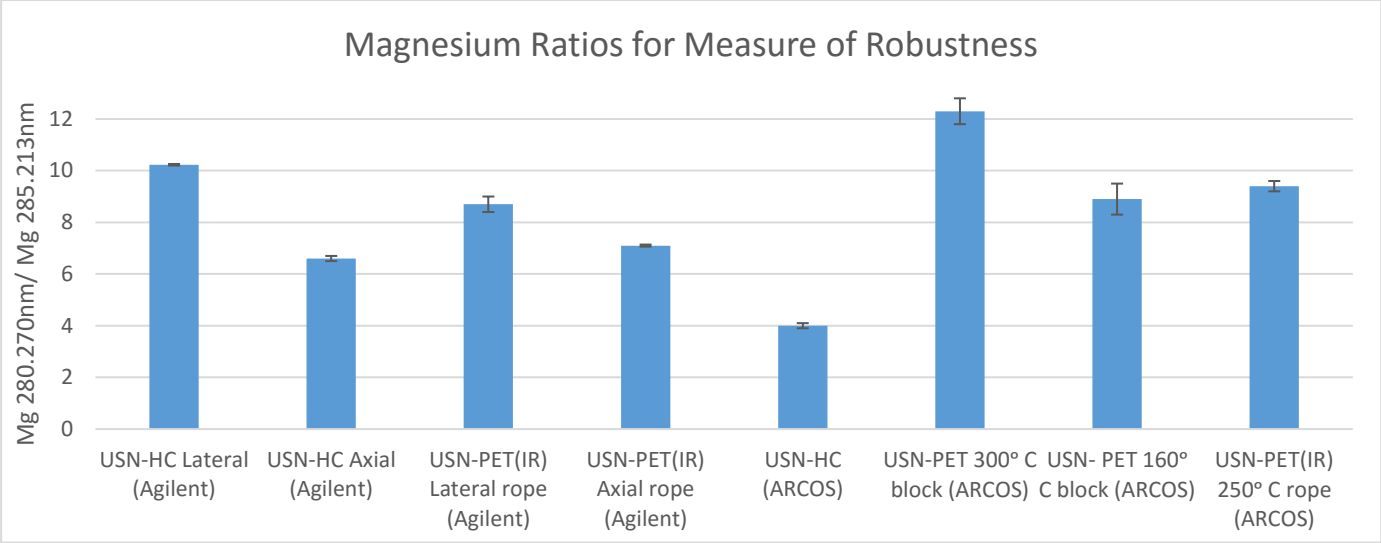

Figure 2.5: Magnesium ratios (Mg 280.270nm/ Mg 285.213) for measure of robustness for Ultrasonic Nebuliser Setups

2.3.4 Analysis of food and water samples

Plasma robustness of the USN-PET(IR) 300 °C setup was further investigated, as this method provided the best analytical capabilities of all methods tested. This second analysis of robustness was done by comparing detected concentrations of elemental analytes in waste water and corn bran samples to certified reference values and their confidence limits at the 95% confidence level. A simple external calibration without internal standardisation, but with matrix-matching was conducted. For simplicity of matrix-matching the standards used in the experiment, the corn bran digests were diluted until a 4 % HNO_3 concentration was reached. Due to this, corn bran digests had to be diluted more than is typically done for food samples [24]. This caused many elemental analytes to have extremely low concentrations that cannot be detected by ICP-OES, and the number of elements listed for the corn bran SRM 8433 is therefore reduced. Internal standardisation with an Ar emission line, as had previously been done [14, 15], was not beneficial to these experiments and therefore is not included is Table 2.9.

Table 2.9: Concentrations ± standard deviation (n = 5) determined in certified reference materials by USN-PET(IR) 300°C Block (ARCOS)

	Waste Water, Low (EU-L-3) (mg/L)		Corn Bran SRM 8433 (mg/kg)	
Element	**USN-PET(IR)**	**Certified ± Confidence Limit**	**USN-PET(IR)**	**Certified ± Confidence Limit**
Al	6.50 ± 0.04	6.28 ± 0.19		
As	8.45 ± 0.10	8.40 ± 0.12		
Be	1.23 ± 0.01	1.23 ± 0.02		
Cu	10.58 ± 0.21	10.6 ± 0.2		
Cd	2.29 ± 0.03	2.28 ± 0.05		
Cr	6.15 ± 0.07	6.26 ± 0.15		
Fe	5.60 ± 0.11	5.80 ± 0.09	15.47 ± 0.32	14.8 ± 1.8
K	202.6 ± 4.2	207 ± 5	475.3 ± 84.5	566 ± 75
Mn	11.83 ± 0.16	12.2 ± 0.2	2.30 ± 0.15	2.55 ± 0.29
Mo	3.97 ± 0.05	3.97 ± 0.08		
Na			471.4 ± 64.5	430 ± 31
Ni	8.29 ± 0.06	8.34 ± 0.12		
Pb	4.13 ± 0.01	4.18 ± 0.06		
S			658.7 ± 83.9	860 ± 150
Sb	1.78 ± 0.03	1.84 ± 0.07		
Se	2.84 ± 0.05	2.79 ± 0.16		
Zn	2.90 ± 0.06	3.05 ± 0.21	17.09 ± 0.73	18.6 ± 2.2

2.4 Conclusions

As formerly found, replacing the HC of a conventional USN-HC with an IR-heated pre-evaporation tube resulted in drastically improved analytical performance in terms of detection limit, sensitivity, precision and robustness, as a result of the preservation of water vapour. Due to the uniformity of pure IR heating when using block heaters, these were found to provide greater analytical capabilities than rope heaters, which produce heat via both IR and convective means. This additional convective heating caused problems not only with uniformity along the PET, but resulted in the area downstream of the heated region having higher temperatures than that measured by the thermocouple at the base of the torch. The current experiments also proved that higher temperatures provide more efficient pre-evaporation and consequentially, better detection capabilities. Therefore, the previous work at 400 °C generally had higher sensitivities, lower detection limits, and was more robust than the

best-case-scenario 300 °C method in this work. However, the gains of the 400 °C method were not drastic, and considering the increased sample introduction efficiency of the 300 °C method (sample uptake rate was approximately halved and IR temperature was lowered 100 °C), the newer method may be more desirable, depending on the applications.

When comparing the work on the ARCOS instrument to the Agilent instrument, it is clear that the latter could benefit from using a shorter PET with fewer connections (resulting in a lower probability of air leaks), and applying a block IR heater instead of the rope heater. In order to bring the USN close enough to the torch box, the plastic shelf at the sample introduction area of the ICP-OES could be cut to allow the USN to be brought right up to the instrument. Therefore, a PET even shorter than the 38.1cm tube used on ARCOS could potentially be used and the sample introduction efficiency may be further improved. Furthermore, the increase in sensitivity afforded by axial view could be more optimally coupled with USN-PET(IR), which cannot be done on the lateral-only ARCOS instrument. Since the Agilent torch design likely also played a role in efficiency of pre-evaporation, as only 3 cm of the torch injector could be heated on the modified torch, future work would also likely benefit from further modifications of the torch. By hollowing out the plastic casing (creating a circular tunnel around the torch injector), and making the casing out of a different material (i.e. Teflon) to be more resistant to heating, a full 7 cm of torch injector could be heated, as is the case for ARCOS experiments. This tunnel could be lined with aluminum foil to further diminish the possibility of melting by heating. A Teflon torch casing would allow for the same lightness and construction of the torch, but would prevent deformation at the gas inlets. This greater heating area above the sheath gas adaptor would prevent pre-vaporized aerosol from cooling prior to entering the ICP, which has often resulted in condensation at the sheath gas adaptor connection. Therefore, the benefits of pre-evaporation experiments of the ARCOS instrument can be more thoroughly and comparably investigated on the Agilent instrument.

2.5 References

[1] Chaves, E. S., de Loos-Vollebregt, M. T. C., Curtius, A. J and Vanhaecke, F., Determination of trace elements in biodiesel and vegetable oil by inductively coupled plasma optical emission Spectrometry following alcohol dilution. Spectrochimica Acta Part B: At. Spectrosc., (2011), 66, 733-739.

[2] Pohl, P and Sturgeon, R. E. Simultaneous determination of hydride- and non hydride-forming elements by inductively coupled plasma optical emission Spectrometry. Trends in Anal. Chem., (2010), 29, 1376-1389.

[3] Nardi, E. P., Evangelista, F. S., Tormen, L., Saint´Pierre, T. D., Curtius, A. J., Souza, S. S. d and Barbosa, J.F. The use of inductively coupled plasma mass Spectrometry (ICP-MS) for the determination of toxic and essential elements in different types of food samples. Food Chem., (2009), 112, 727-732.

[4] Pohl, P., Vorapalawut, N., Bouyssiere, B., Carrier, H and Lobinski, R. Direct multi-element analysis of crude oils and gas condensates by double-focusing sector field inductively coupled plasma mass Spectrometry (ICP MS). J. Anal. At. Spectrom, (2010), 25, 704-709.

[5] Martin-Esteban, A., Slowikowski, B and Grobecker, K. H. Correcting sensitivity drift during long-term multi-element signal measurements by solid sampling-ETV-ICP-MS. Talanta, (2004), 63, 667-673

[6] Charles B. Boss and Kenneth J. Fredeen, Concepts, Instrumentation, and Techniques in Inductively Coupled Plasma Optical Emission Spectrometry, 2nd Edition, The Perkin-Elmer Corporation, 1997.

[7] J. Borkowska-Burnecka, A. Lesniewicz and W. Zymicki, Spectrochim. Acta, Part B, (2006), 61, 579–587.

[8] K. V. Desboeufs, R. Losno and J. L. Colin, Figures of merit of pneumatic and ultrasonic sample introduction systems in inductively coupled plasma–multichannel-based emission spectrometry in an ultra-clean environment, Anal. Bioanal. Chem., (2003), 375, 567–573.

[9] J. Mora, S. Maestre, V. Hernandis and J. L. Todoli, Liquid-sample introduction in plasma spectrometry, TrAC, Trends Anal. Chem., (2003), 22, 123–132.

[10] I. Novotny, J. C. Farinas, J. L. Wan, E. Poussel and J. M. Mermet, Effect of power and carrier gas flow rate on the tolerance to water loading in inductively coupled plasma atomic emission spectrometry, Spectrochim. Acta, Part B, (1996), 51, 1517–1526.

[11] M. Bensimon, J. Bourquin and A. Parriaux, Determination of ultra-trace elements in snow samples by inductively coupled plasma source sector field mass spectrometry using ultrasonic nebulization, J. Anal. At. Spectrom., (2000), 15, 731–734.

[12] T. Prohaska, S. Hann, C. Latkoczy and G. Stingeder, Determination of rare earth elements U and Th in environmental samples by inductively coupled plasma double focusing sectorfield mass spectrometry (ICP-SMS), J. Anal. At. Spectrom., (1999), 14, 1–8.

[13] S. E. Long and R. F. Browner, Influence of water on conditions in the inductively coupled argon plasma, Spectrochim. Acta, Part B, (1988), 43, 1461–1471.

[14] A. Asfaw, W. MacFarlane and D. Beauchemin, Ultrasonic nebulization with infrared heated preevaporation tube for sample introduction in ICP-OES: application to geological and environmental samples, J. Anal. At. Spectrom., 27 (2012) 1254-1263

[15] A. Asfaw and D. Beauchemin, Improvement of the capabilities of inductively coupled plasma optical emission spectrometry by replacing the desolvation system of an ultrasonic nebulization system with a pre-evaporation tube, Spectrochim. Acta, Part B, (2010), 65, 376-384.

[16] A. Belhamra, R. Diabi and A. Moussaoui, Technology and applications of infrared heating in the industrial area, J. Eng. Appl. Sci., (2007), 2, 1183–1187.

[17] K. Krishnamurthy, H. K. Khurana, S. Jun, J. Irudayaraj and A. Demirci, Infrared heating in food processing: an overview, Compr. Rev. Food Sci. Food Saf., (2008), 7, 2–13.

[18] S. Liu and D. Beauchemin, The effect of pre-evaporation on ion distributions in inductively coupled plasma mass Spectrometry. Spectrochim. Acta B, 61, (2006), 157 – 163.

[19] J. M. Mermet, Use of magnesium as a test element for inductively coupled plasma atomic emission Spectrometry diagnostics. Anal. Chim. Acta, 250, (1991), 85-94.

[20] X. Romero, E. Poussel and J. M. Mermet, Influence of the operating conditions on the efficiency of internal standardization in inductively coupled plasma atomic emission Spectrometry. Spectrochim. Acta B, 52, (1997), 487-493.

[21] M. Grotti, C. Lagomarsino and R. Frache, Multivariate study in chemical vapor generation for simultaneous determination of arsenic, antimony, bismuth, germanium, tin, selenium, tellurium and mercury by inductively coupled plasma optical emission spectrometry, J. Anal. At. Spectrom, (2005), 20, 1365-1373.

[22] I. B. Brenner and A. T. Zander, Axially and radially viewed inductively coupled plasmas – a critical review, Spectrochim. Acta B, (2000), 55, 1195 - 1240.

[23] Y. Ralchenko, A. Kramida and J. Reader, NIST Atomic Spectra Database (ver. 5.1), http://physics.nist.gov/asd.

[24] N. Sadiq and D. Beauchemin, Optimization of the operating conditions of solid sampling electrothermal vaporization coupled to inductively coupled plasma optical emission spectrometry for the sensitive direct analysis of powdered rice, Analytica Chimica Acta, (2014), 851, 23-29.

Chapter 3: Improvements to the Analytical Performance of a Multi-Mode Sample Introduction System by coupling to an Infrared Heated Pre-Evaporation Tube

3.1 Introduction

Inductively coupled plasma mass spectrometry (ICP-MS) and ICP-OES remain two of the most used methods for simultaneous multi-elemental analysis of a large variety of samples [1]. While ICP-MS has the benefit of higher sensitivities and lower detection limits, ICP-OES is intrinsically more robust. Therefore, a common goal in ICP-OES research is to improve its detection limits without jeopardising robustness [2]. Both ICP-OES and ICP-MS are conventionally equipped with a pneumatic nebuliser and spray chamber [3], which typically results in 95-98% of the sample being pumped out of the spray chamber and into the waste.

Alternative sample introduction systems seek to improve both the sample introduction efficiency and the analytical performance of both ICP-OES and ICP-MS. One such method is the multimode sample introduction system (MSIS) [4], which has an efficiency of nearly 100% when hydride compounds are produced [5]. MSIS uses chemical vapour generation (CVG) to produce a vapour-phase species in a spatially free gap at the centre of a cyclonic spray chamber [6]. Hydride generation (HG), an example of CVG, occurs when a sample in dilute acid is mixed with a reducing agent (such as $NaBH_4$) to produce atomic hydrogen. This hydrogen reacts with As, Bi, Cd, Hg, Ge, Pb, Sb, Se, Sn, and Te [7, 8] in solution to form volatile hydrides [9], which are separated from the liquid reaction mixture and transported to the plasma. Therefore, the volatile hydrides not only have improved sensitivity due to the elimination of large droplets; they are also separated from the matrix which minimizes potential interferences. HG may encounter difficulties whereby different reaction conditions are required for each individual hydride [10, 11], meaning this technique is commonly only used for one element at a time [7]. However, MSIS allows for the simultaneous determination of hydrides and non-hydride forming elements. MSIS functions in three different modes: dual mode involves both HG and nebulisation; HG

mode involves only CVG; and nebulisation mode is in essence conventional nebulisation with a cyclonic spray chamber (no CVG) [12].

By equipping ICP-OES with MSIS [13, 14, 15], the goal is to improve on the sensitivity and detection limit of hydride-forming elements, without losing the robust qualities of the OES instrument. However, it is often the case that hydride-forming elements see a greater improvement in sensitivity than in detection limits [13, 16], and non-hydride forming elements experience degradation of analytical figures of merit [17, 18]. Moreover, the advantage of matrix separation by HG is lost when MSIS is operated in dual mode [18]. Following from past work in pre-evaporation techniques [2, 19, 20], attempts were made to couple MSIS with a PET, in hopes that the improvements in sensitivity and detection limit that are achieved by HG could be combined with the improvements in analytical performance demonstrated by PET setups in the past [9]. With the benefits of pre-vaporising the sample to remove large droplets which would otherwise cool the plasma, and the continuous introduction of water vapour, which has been demonstrated to improve sensitivity and detection limit [9], pre-evaporation avoids the difficulties afforded by other attempts to improve the detection limits of ICP-OES. For instance, USN-HC involves desolvation of the sample to pre-concentrate the analyte; but in doing so the matrix is also pre-concentrated, thereby increasing the matrix effects [3]. Additionally, water is removed by this method which strips the technique of water's beneficial characteristics in the ICP. In addition to acting as a load buffer to minimize matrix effects [21], the hydrogen atoms produced by water in the plasma help facilitate the energy transfer between the bulk of the plasma and the central channel where the analytes are located. Therefore, the combined effects of water vapour being generated and preserved by the PET setup, noise being reduced by the pre-evaporation of the aerosol, and the hydrogen by-product from HG increasing energy transfer within the plasma, are reported to account for the improvements in analytical performance for MSIS-PET(HT) [9].

The work described in this chapter builds off Asfaw's MSIS-PET(HT) method by replacing the heating tape with an infrared-heated ceramic rope. As IR radiation provides a more uniform heating temperature and high thermal efficiency [22, 23] by being directly converted to heat upon absorption by a material [24], it is expected that this replacement will improve detection capabilities further. Previously, this replacement of heating method proved successful with an ultrasonic nebuliser coupled to a PET [2, 20]. By comparing the MSIS(IR) method on two different ICP-OES instruments and referencing the new analytical figures of merit back to sensitivities, detection limits, and precisions achieved by conventional PN, conventional MSIS, and MSIS-PET(HT), the reasons for improvement (or lack thereof) are thoroughly investigated, and improvements are suggested for future MSIS(IR) setups.

3.2 Experimental

3.2.1 Instrumentation

Method development and application was performed on an ARCOS ICP-OES instrument (lateral view, SPECTRO Analytical Instruments, Kleve, Germany) and an Agilent 5100 ICP-OES (dual view, Agilent Technologies, Santa Clara, California, United States). These instruments were equipped with a cyclonic double-pass spray chamber and pneumatic Seaspray nebuliser (both Agilent Technologies, Santa Clara, California, United States), which were used for reference experiments. The conventional pneumatic nebulisation setup was replaced on both instruments with a multi-mode sample introduction system spray chamber. A OneNeb nebuliser (Agilent Technologies, Santa Clara, California, United States) was used for all MSIS experiments on the Agilent instrument, while a Mira-Mist parallel path nebuliser (Burgener Research, Mississauga, Ontario, Canada) was used for ARCOS MSIS experiments. For MSIS(IR) setups, an IR-heated pre-evaporation glass tube was inserted between the spray chamber and the torch. The optimal operating conditions for all setups are provided in Tables 3.1 to 3.4.

Table 3.1: Optimal conditions for MSIS(IR) with SPECTRO ARCOS

Condition	Dual Mode	HG Mode	Nebulisation Mode
RF Power (kW)	1.45	1.45	1.45
Plasma gas (L/min)	14	12	12
Aux gas (L/min)	1.0	1.0	1.0
Nebulizer gas (L/min)	1.0	0.8	0.8
Sample uptake (mL/min)	2.0	2.0	2.0
IR temperature (°C)	175	175	175
Plasma observation height (mm)	11	11	11

Table 3.2: Optimal conditions for Conventional MSIS with SPECTRO ARCOS

Condition	Dual Mode	HG Mode
RF Power (kW)	1.45	1.45
Plasma gas (L/min)	12	12
Aux gas (L/min)	1.0	1.0
Nebulizer gas (L/min)	0.7	0.8
Sample uptake (mL/min)	2.0	2.0
Plasma Observation Height (mm)	11	11

Table 3.3: Optimal conditions for MSIS (IR) with Agilent 5100

Condition	Dual Mode Lateral	Dual Mode Axial	HG Mode Lateral	HG Mode Axial	Nebulisation Mode Lateral	Nebulisation Mode Axial
RF Power (kW)	1.5	1.5	1.5	1.5	1.5	1.5
Plasma gas (L/min)	14	14	13	13	14	14
Aux gas (L/min)	1.0	1.0	1.0	1.0	1.0	1.0
Nebulizer gas (L/min)	0.6	0.5	0.6	0.5	0.6	0.5
Sample uptake (mL/min)	1.0	1.0	2.0	2.0	2.0	2.0
IR Temperature (°C)	100	100	100	100	80	80
Plasma Observation Height (mm)	2	N/A	2	N/A	2	N/A

Table 3.4: Optimal conditions for Conventional MSIS with Agilent 5100

Condition	Dual Mode Lateral	Dual Mode Axial	HG Mode Lateral	HG Mode Axial	Nebulisation Mode Lateral	Nebulisation Mode Axial
RF Power (kW)	1.4	1.5	1.5	1.5	1.5	1.5
Plasma gas (L/min)	13	12	14	12	12	14
Aux gas (L/min)	1.0	1.0	1.0	1.0	1.0	1.0
Nebulizer gas (L/min)	0.65	0.5	0.65	0.5	0.5	0.5
Sample uptake (mL/min)	1.0	1.0	2.0	2.0	2.0	2.0
Plasma Observation Height (mm)	4	NA	5	NA	2	NA

3.2.2 Multimode sample introduction system

Conventional MSIS and MSIS(IR) experiments were conducted in all three modes. Dual mode (Fig. 3.1) allowed for the simultaneous determination of hydride-forming and non-hydride forming elements. Samples and standards were pumped into both the vapour generation sample inlet and the nebuliser while the $NaBH_4$ was pumped through the reductant sample inlet, all via the instrument's peristaltic pump. Upon reaction of the acidified sample with $NaBH_4$, hydrides were formed in the MSIS chamber and aerosol was swept through the PET and into the ICP via the Ar carrier gas.

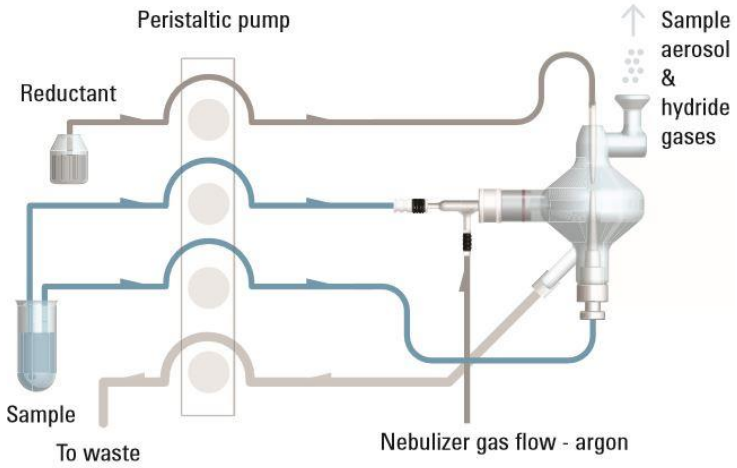

Figure 3.1: Dual mode schematic (© Agilent Technologies, Inc. 2016 Reproduced with Permission, Courtesy of Agilent Technologies, Inc.)

Hydride generation mode (Fig. 3.2) required blocking the nebuliser sample line, and only pumping the samples and standards through the vapour generation sample inlet, and $NaBH_4$ through the reductant sample inlet. Due to the self-aspirating nature of the OneNeb, this nebuliser line was clamped to an external peristaltic pump and the end of the line was submerged in DDW.

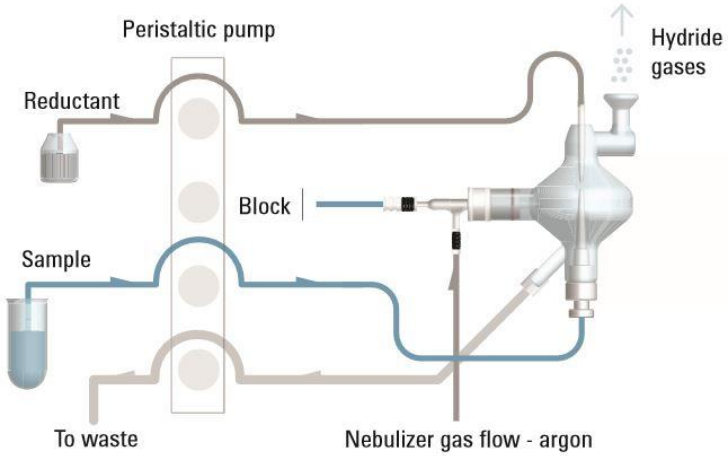

Figure 3.2: Hydride generation mode schematic (© Agilent Technologies, Inc. 2016 Reproduced with Permission, Courtesy of Agilent Technologies, Inc.)

Nebulisation mode (Fig. 3.3) involved blocking the vapour generation and reductant sample lines, and only pumping samples and standards through the nebuliser sample inlet. Hence, Nebulisation Mode worked as a conventional ICP-OES operation would, with sample aerosol being carried up to the ICP via Ar carrier gas.

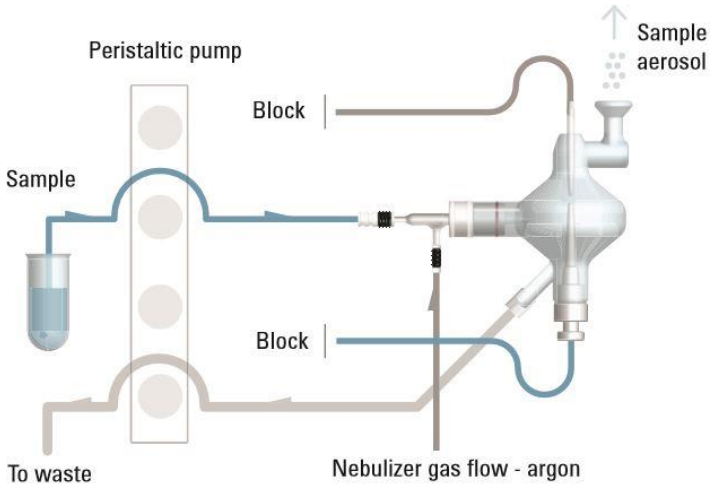

Figure 3.3: Nebulization mode schematic (© Agilent Technologies, Inc. 2016 Reproduced with Permission, Courtesy of Agilent Technologies, Inc.)

3.2.3 IR-heated pre-evaporation system

For the IR-heated pre-evaporation system, illustrated in Fig. 3.4, an 8 cm long glass tube with a 5 mm internal diameter and 12mm/5mm ground glass ball and socket joint was connected between the MSIS spray chamber and a conventional ICP torch (Agilent Technologies, Santa Clara, California, United States, and SCP Science, Baie d'Urfe, Quebec, Canada, for the 5100 and ARCOS, respectively).

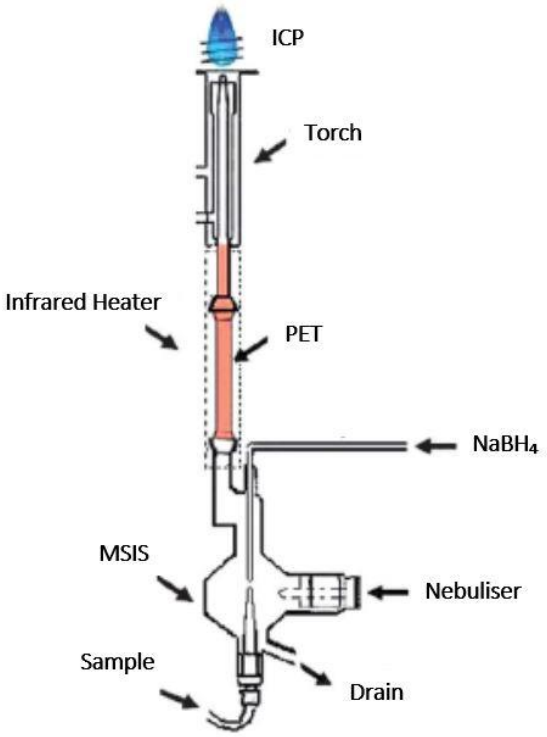

Figure 3.4: Multimode sample introduction system combined with an IR-heated pre-evaporation tube (Adapted from Ref. 9 with permission from The Royal Society of Chemistry).

All IR-heated setups involved tightly wrapping a heated wire strung with ceramic beads (a rope heater) (Marsh Beaded Heaters, Normangee, Texas, US) around the PET, and lower injector portion of the torch. The heater was then surrounded in aluminum foil to provide insulation. The lower 7 cm of the torch was heated in the case of ARCOS experiments (Fig. 3.5), while only the lower 3 cm of the torch was heated for the Agilent experiments (Fig. 3.6 and 3.7). The Agilent instrument required specialized torches with a plastic casing surrounding the injector. Hence a modified torch was used, in which the bottom 2 cm of plastic casing was cut off so that the exposed quartz could be heated. A thermocouple was attached to the outer heated portion of the torch and the temperature was controlled by two PL512 Mantle-Minder temperature controllers (GLAS-COL Apparatus Company).

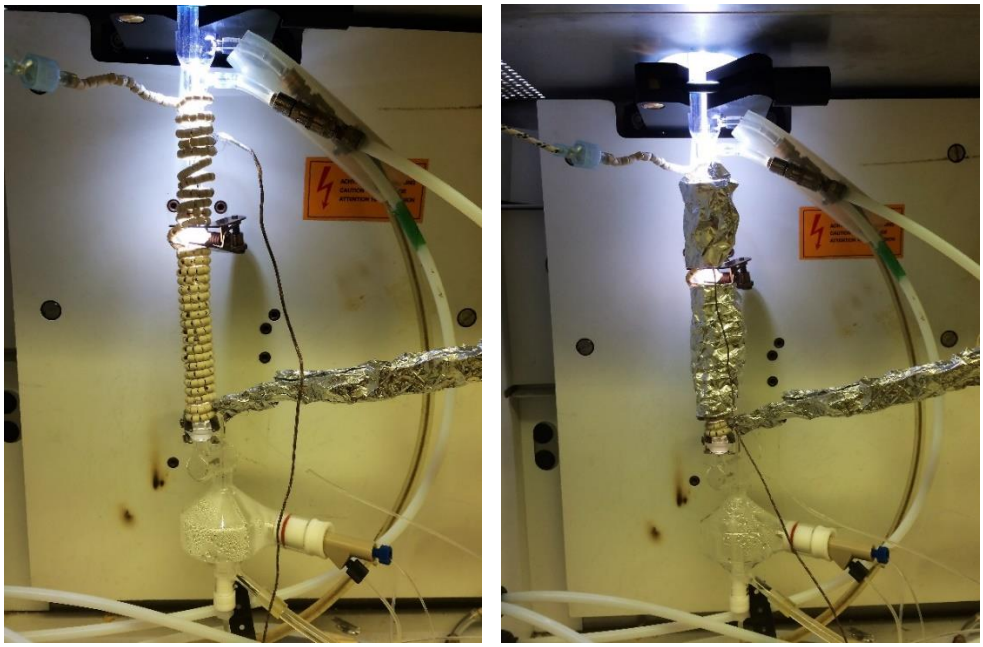

Figure 3.5: MSIS(IR) setup for the SPECTRO ARCOS, heating the 8cm pre-evaporation tube and the bottom 7cm of the torch; at right, foil is used for insulation.

To compare the effectiveness of heating the MSIS spray chamber in addition to the PET, two setups were used for the Nebulization Mode on the Agilent instrument. First, the upper region of the spray chamber, 8 cm pre-evaporation tube, and bottom 3 cm of the torch were heated (Fig 3.6).

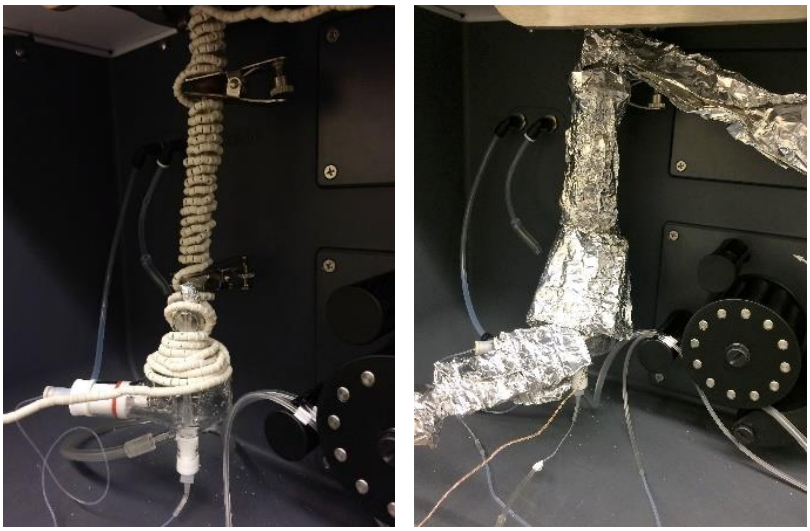

Figure 3. 6: MSIS(IR) setup for the Agilent 5100, heating the spray chamber, 8 cm pre-evaporation tube and bottom 3 cm of the torch; used as Setup 1 for Nebulization Mode.

A second setup (Fig 3.7) was tested in which the spray chamber was not heated. This second version of the IR setup was necessary for Dual Mode and HG Mode, as the upper sample entrance was needed for $NaBH_4$ entry. While this entrance can be blocked off and the sample and $NaBH_4$ can be mixed at a Y-connector prior to entering the spray chamber from the lower sample entrance (as could be done for the conventional setup), this does not suffice for the IR-heated method, as the plasma is overloaded during the sample's reaction with $NaBH_4$. Hence, Setup 2 is used for Dual Mode and HG Mode.

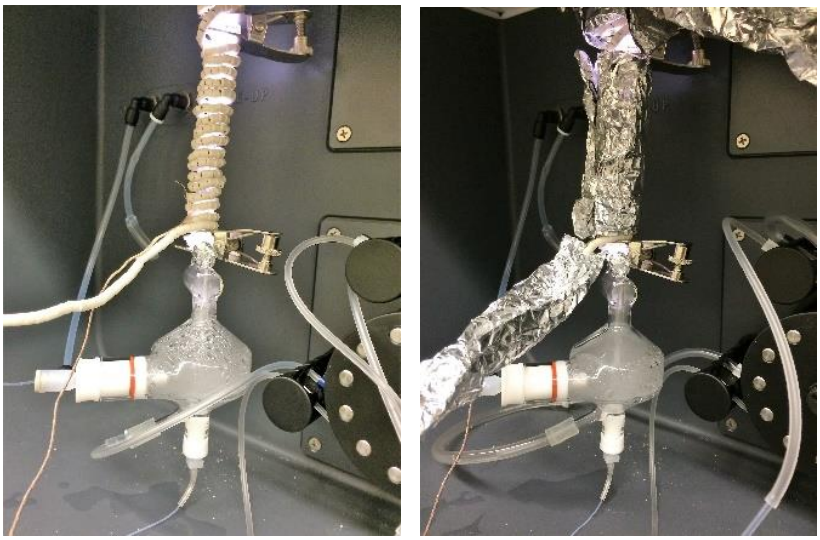

Figure 3. 7: MSIS(IR) setup for the Agilent 5100, heating the 8 cm pre-evaporation tube and bottom 3 cm of the torch; used as Setup 2 for Nebulisation Mode, and used for Dual Mode and HG Mode with upper and lower sample inlets in use.

3.2.4 Reagents and certified reference materials

18 Ω cm^{-1} double deionized water (DDW) (Pro UV/DI, Sartorius Stedim Biotech, Gottingen, Germany) and HNO_3 (ACS grade; Fisher Scientific, Ottawa, Canada) that was purified prior to use with a DST-1000 Teflon sub-boiling distillation system (Savillex, Minnetonka, USA), were used to prepare all standard solutions and samples. Multi-elemental 100 mg L^{-1} stock solutions were prepared by diluting 1000 and 10 000 mg L^{-1} mono-elemental plasma standard solutions (SCP Science, Baie d'Urfe, Quebec,

Canada) (Bi, Ga, Hg, Eu, Na, In, Se, Li, Y, Ge, Mo, Sb, Si, Ti, Zr, Al, As, Be, Cd, Co, Ce, Cr, Cu, Fe, K, La, Mg, Mn, Ni, P, Pb, S, Sr, V, Zn) in 4% HNO_3. From the 100 mg L^{-1} solutions, 10 mg L^{-1} stock solutions were made with 2% HNO_3. More dilute multi-element solutions as calibration standards were prepared daily via dilution with 1 mol L^{-1} HNO_3.

2.0% $NaBH_4$ for hydride generation was prepared from 98% pure $NaBH_4$ (ACROS ORGANICS, New Jersey, USA) in 0.1 mol L^{-1} ACS reagent grade NaOH (Bio Shop Canada Inc., Burlington, ON, Canada). 10% m/m L-Cysteine solution was made by dissolving ≥97% grade L-cysteine (Sigma-Aldrich, Steinhein, Germany) in DDW. Addition of the pre-reducing agent, L-cysteine, was necessary as HNO_3 is oxidizing and could therefore affect an analyte's HG efficiency [25]. For HG experiments (MSIS In dual and HG modes), the multi-element solutions and corresponding blanks were made with HNO_3 and L-cysteine solution added to give final concentrations of 1.0M HNO_3 and 1% m/m L-cysteine. Concentrations of $NaBH_4$ and HNO_3 for HG were previously optimized in work by Asfaw [9].

Certified reference Waste Water EU-L-3 (SCP Science, Baie d'Urfe, Quebec, Canada) was prepared by adding 10% m/m L-Cysteine solution to yield a final concentration of 1% L-cysteine. SRM 8433 Corn Bran (National Institute of Standards and Technology, Gaithersburg, MD, USA) was digested on a hot plate prior to analysis. About 0.3g of SRM was weighed into a Teflon decomposition vessel (Savillex) and 2.5 mL HNO_3 and 0.5 mL H_2O_2 (30 wt. % in H_2O, ACS reagent, Sigma-Aldrich, Steinhein, Germany) were added prior to placing the vessel on a hot plate at 50 °C for 2 hours. L-cysteine solution was added to each digest which was diluted to 60mL with DDW, yielding final concentrations of 1.0 M HNO_3 and 1% m/m L-cysteine. All standards and blanks for calibration were prepared with matching final acid and L-cysteine concentrations.

3.2.5 Optimization

To conduct multivariate optimizations, a 100 μg L^{-1} multi-elemental solution was aspirated and operating parameters were adjusted in order to find the local thermodynamic equilibrium (LTE). At this state, there is efficient energy transfer between the bulk and central channel of the plasma. By monitoring the Mg II 280.270 nm/ Mg I 285.213 nm ratio, operating parameters that provided the most robust conditions were chosen. Here, a ratio of 10 or more corresponded to a robust plasma, meaning that changes in matrix composition and solvent loading do not significantly impact plasma excitation. Hence, improved sensitivity and detection limit of analytes can be established. Optimization results were also analyzed for all 35 elemental analytes in order to find compromise conditions that provide both a robust plasma and best-case sensitivities for all elements. A face-centered central composite design was used for optimization of nebuliser gas flow rate, plasma gas flow rate, RF power, sample uptake rate, and IR temperature for all IR-heated experiments (Table 3.5).

Table 3.5: Central composite design for optimization of MSIS(IR) on Agilent 5100

Run Order	RF Power (kW)	Plasma Flow Rate (L/min)	Nebulizer Flow Rate (L/min)	Sample Uptake (mL/min)	IR Temperature (°C)
1	1.4	13	0.75	1.25	100
2	1.4	13	0.75	1.25	200
3	1.5	14	0.50	0.50	250
4	1.4	12	0.75	1.25	200
5	1.5	12	0.50	0.50	100
6	1.4	14	0.75	1.25	200
7	1.3	14	1.00	2.00	100
8	1.4	13	0.75	1.25	200
9	1.5	12	1.00	0.50	250
10	1.3	12	0.50	0.50	250
11	1.3	12	1.00	0.50	100
12	1.4	13	0.75	2.00	200
13	1.3	14	1.00	0.50	250
14	1.4	13	0.75	1.25	200
15	1.4	13	0.75	0.50	200
16	1.5	14	1.00	0.50	100
17	1.4	13	0.75	1.25	200

18	1.3	13	0.75	1.25	200
19	1.4	13	1.00	1.25	200
20	1.4	13	0.75	1.25	250
21	1.3	12	1.00	2.00	250
22	1.4	13	0.50	1.25	200
23	1.3	14	0.50	2.00	250
24	1.5	14	1.00	2.00	250
25	1.3	14	0.50	0.50	100
26	1.3	12	0.50	2.00	100
27	1.5	12	0.50	2.00	250
28	1.5	13	0.75	1.25	200
29	1.5	12	1.00	2.00	100
30	1.4	13	0.75	1.25	200
31	1.5	14	0.50	2.00	100
32	1.4	13	0.75	1.25	200

Comparable optimization experiments were conducted for the PN and conventional MSIS setups, in which IR temperature was not included as a factor. Following these multivariate optimizations, a univariate optimisation of plasma observation height was employed while holding all other operating parameters at their optimum values. The IR temperature was kept at a maximum of 175 °C for ARCOS experiments to prevent overloading of the plasma, while the temperature had to be kept at a maximum of 250 °C for Agilent experiments to prevent melting of the nebuliser and torch casing. Extra precautions in temperature settings had to be taken to ensure damage to the Agilent torch casing would not occur, since the rope heater provided both convective and IR heating. This resulted in the area downstream of the heater being a higher temperature than that measured by the thermocouple at the base of the torch.

3.2.6 Data Analysis

Sensitive atomic and ionic emission lines free from potential spectroscopic interference were selected for all 35 elemental analytes and were evaluated in terms of emission intensity for multivariate optimizations created with Minitab 17 Software. For all ARCOS experiments, the signals were corrected

using two points (one on either side of the emission peak) for polynomial background correction (Smart Analyzer Vision Software, SPECTRO Analytical Instruments, Kleve, Germany). A fitted background correction was selected with 3 pixels read per analyte line (ICP Expert Software, Agilent Technologies, Santa Clara, California, United States) for the experiments on the Agilent instrument. All experiments following the Minitab 17 multivariate optimizations were processed in Microsoft Excel 2013. The signal intensity of the blank was subtracted from the intensity of its corresponding multi-element standard solution or sample to give the net signal intensity for a given standard or sample. Detection limits were calculated as 3 times the standard deviation of the average signal intensity of at least 10 consecutive blanks divided by the slope of the calibration curve (known as the sensitivity).

3.3 Results and Discussion

3.3.1 Selection of optimum parameters

For the purpose of succinctness, only the optimization of MSIS(IR) HG Mode on the Agilent 5100 will be discussed in this section. Contour plots of blank-subtracted signal intensities and Mg II/ Mg I ratios are shown for both axial and lateral view optimizations (Fig. 3.8 and 3.9, respectively), where dark green indicates the highest values and dark blue indicates the lowest values. While only Hg 184.887nm and Mg 280.270 nm/ Mg 285.213 nm contour plots are shown, results for all 35 analytes were analyzed for optimization experiments. Similar contour plot trends were observed for all elemental lines, resulting in a simple compromise for optimal settings. The similarity of optimal conditions for different elemental analytes agrees with a previous work in which one sampling depth provided optimal sensitivity for practically all elements [25]. Due to instrumental limits, the “optimal” conditions are sometimes located at a maximum value (Fig. 3.8 and 3.9). For instance, RF power can be set to a maximum of 1.5 kW on the Agilent 5100.

Highest signal intensities and Mg II/ Mg I ratios were observed at an RF power of 1.5 kW. This follows from the literature, as a robust plasma is achieved when the RF power is at least 1400 W [26], and higher RF power increases robustness [27]. Optimal plasma gas flow rate, nebulizer gas flow rate, and sample uptake rate were found to be 13 L min^{-1}, 0.6 L min^{-1}, and 2 mL min^{-1}, respectively. The high-RF power combined with low-flow carrier gas directly correlates to the findings of Novotny et al. [28], in that a lower carrier gas flow is necessary to reduce the amount of aerosol (and in doing so, reduce the solvent loading), and to increase the residence time within the coil. With an increase in carrier gas flow rate and a decrease in power, the electron number density and temperature of the plasma will decrease, resulting in a degenerate plasma and increased matrix effects. Furthermore, a lower carrier gas flow rate increases the path of the aerosol discharge, allowing it to be more thoroughly vaporized by the IR heater prior to beginning atomization in the lower region of the plasma. As only the aerosol exiting the spray chamber is heated, not the aerosol in the spray chamber itself, the system can handle the high sample loading of 2 mL min^{-1}. Additionally, the MSIS spray chamber is larger in volume than that of a USN, hence the higher sample loading of MSIS(IR) in comparison to USN-PET(IR) [Chapter 2 and [2]].

The best IR temperature was 100 °C. While the Mg II/ Mg I ratio peaked at both 100 °C and 250 °C, the lower temperature was found to provide the highest signal intensities for all analyzed elements. This coincides with experiments on the SPECTRO ARCOS in which the plasma became overloaded at temperatures above 175 °C. In the case of the Agilent instrument, the lower temperature was still preferred, regardless of sample loading, because the higher temperatures risked melting the upper areas of the torch casing (i.e. the gas inlets) due to the convective nature of the rope heater. Areas of glass downstream of the rope heater were found to have temperatures 30-60 °C higher than the set heater temperature.

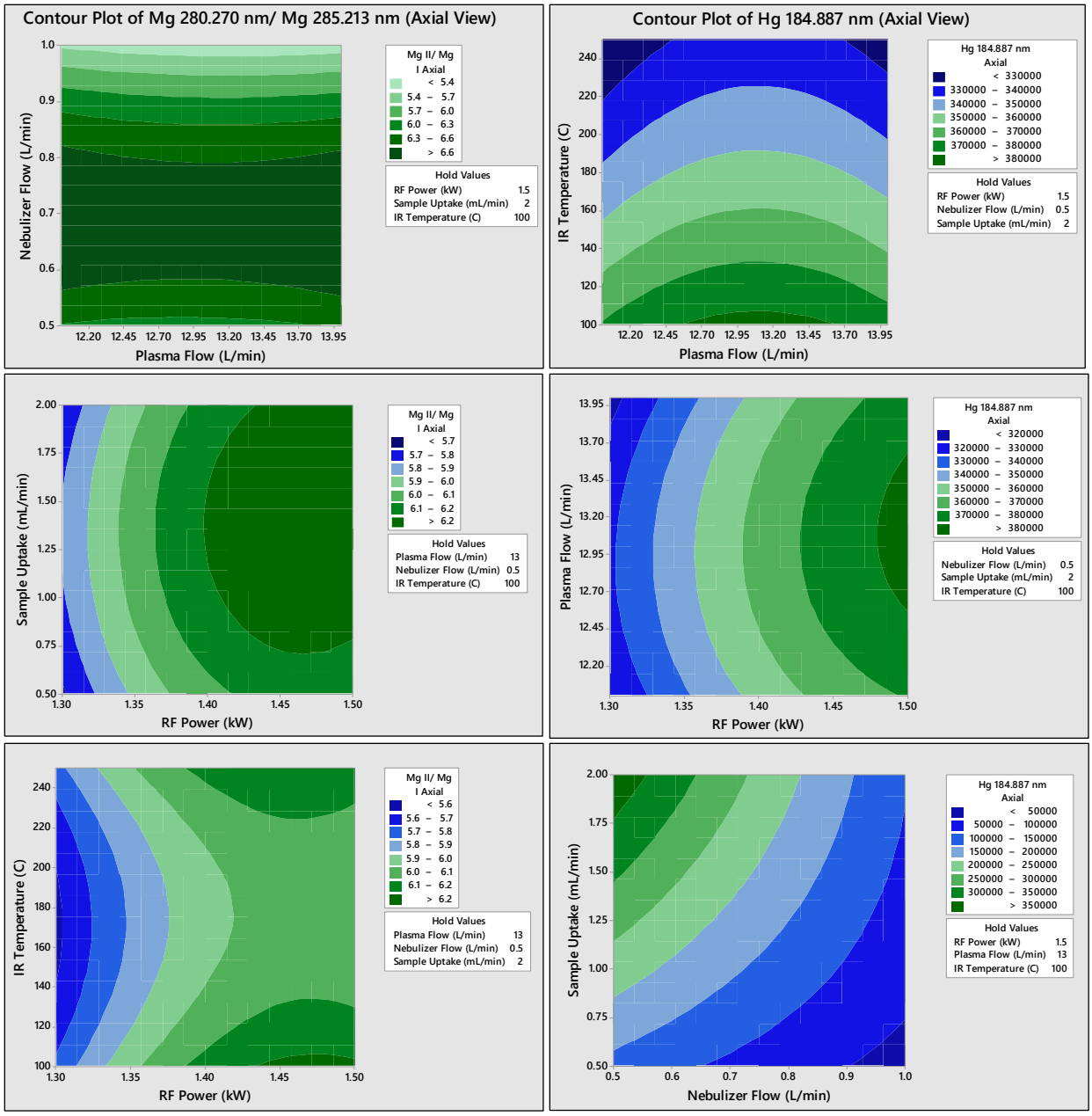

Figure 3.8: Contour plots for the multivariate optimization of MSIS(IR) HG Mode on Agilent 5100 in axial view. Values are held in order to find the optimal compromised conditions for two other parameters. At left, Mg 280.270nm and 285.213nm emission intensities have been blank subtracted, with the ratio providing an indication of robustness. At right, blank subtracted Hg 184.887 nm emission intensities are shown.

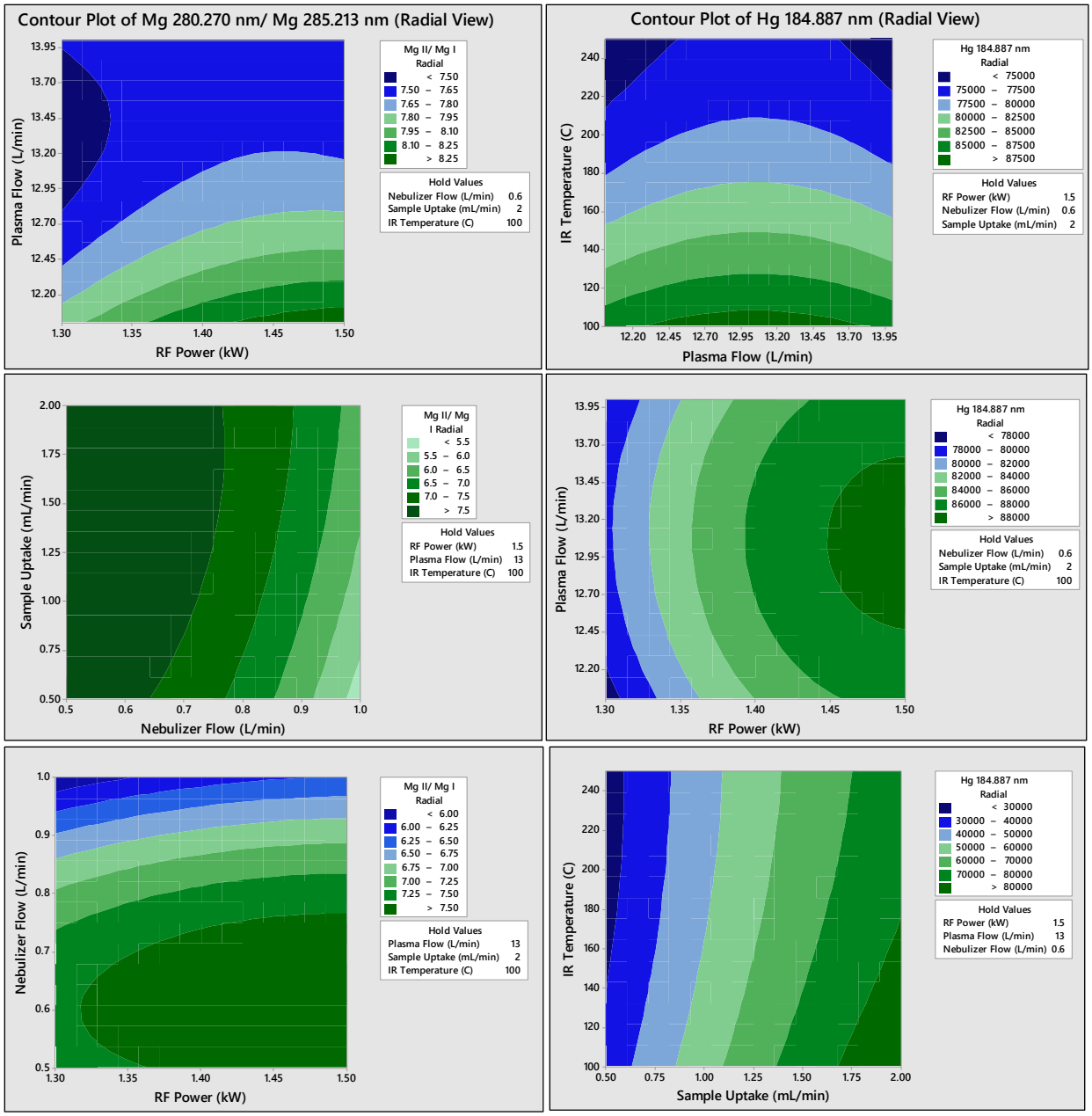

Figure 3.9: Contour plots for the multivariate optimization of MSIS(IR) HG Mode on Agilent 5100 in lateral view. Values are held in order to find the optimal compromised conditions for two other parameters. At left, Mg 280.270nm and 285.213nm emission intensities have been blank subtracted, with the ratio providing an indication of robustness. At right, blank subtracted Hg 184.887 nm emission intensities are shown.

Plasma observation height was optimized for lateral view in a univariate experiment following optimization of all other parameters (Fig. 3.10). Since adjusting the plasma observation height has a greater impact on signal intensities than changing the auxiliary gas flow rate, this gas flow was kept at

the conventionally used 1.0 L min^{-1} for all experimental setups. All other conditions were held at their optimum values and signal intensities were measured as the reading for the detector was directed deeper into the plasma. The optimal plasma observation height was found to be 2 mm for MSIS(IR) HG Mode. Although 5 mm appeared to be optimal for many of the hydride-forming elements, 2 mm was chosen as the optimal height because plasma robustness (indicated by Mg II/ Mg I ratio) decreased as the signal was measured deeper in the plasma. This is in agreement with the literature [28, 29] which reports that Mg II/ Mg I ratio decreases with an increased plasma observation height.

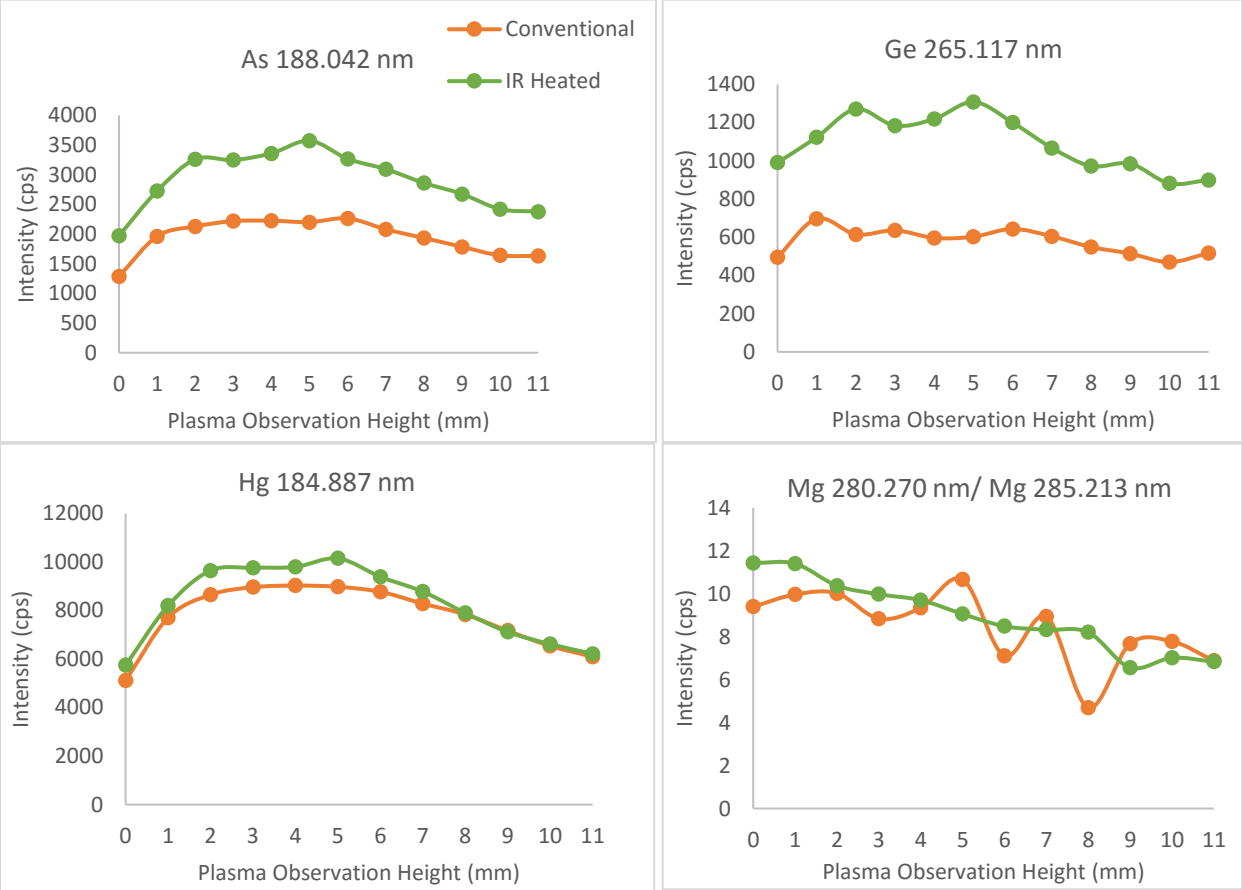

Figure 3.10: Height optimization plots for MSIS(IR) and conventional MSIS HG Mode on Agilent 5100. All other operating conditions were held at Table 2.3 and 2.4 values while plasma observation height was varied.

3.3.2 Sensitivity, detection limit, and precision

Sensitivities, defined as the slopes of the calibration curves for the individual elemental emission lines, and sensitivity ratios for all setups in dual mode, hydride generation mode, and nebulisation mode, are listed in Tables 3.6-3.11. Previously, Asfaw [9] reported an average sensitivity increase by a factor of 58 ± 20 when comparing his dual mode PN-MSIS-PET setup with heating tape, to a PN setup with a cross-flow nebulizer and Scott double-pass spray chamber. For comparison's sake, it should be noted that this sensitivity increase is reduced to 4.1 ± 7.4 when Asfaw's PN-MSIS-PET results are compared to the PN used in this work (which uses a Seaspray nebulizer and double-pass cyclonic spray chamber) on the same ARCOS instrument. The currently investigated MSIS(IR) on the Agilent instrument saw an average sensitivity increase by factors of 170 ± 990 (200 ± 1100), 28 ± 29 (74 ± 90), and 1.8 ± 3.2 (5 ± 11) for Dual Mode, HG Mode, and Nebulisation Mode (setup 2), respectively, when compared to the PN used in this work (where lateral view results are given first, followed by axial view results in brackets). Since setup 2 for Nebulisation Mode generally resulted in slightly lower detection limits than setup 1, only setup 2 will be discussed in detail. By heating the spray chamber in addition to the PET in setup 1, the plasma robustness was likely slightly degraded due to sample overloading (i.e. too much pre-evaporated sample being pushed into the plasma). MSIS(IR) on ARCOS had an average sensitivity increase of 9 ± 29 and 17 ± 20 for Dual Mode and HG Mode, respectively, when compared to the listed PN. With the exception of lateral view Nebulisation Mode, all currently investigated setups are seen to have greater average sensitivity improvements in comparison to PN, than that of the previous work with heating tape.

When compared to Asfaw's PN-MSIS-PET, the MSIS(IR) Dual Mode average sensitivity decreased, with MSIS(IR)/ PN-MSIS-PET average sensitivity ratios of 0.13 ± 0.11 (0.41 ± 0.34) for Agilent, and 0.8 ± 1 for ARCOS. However, when the average detection limits of PN-MSIS-PET and MSIS(IR) Dual

Mode are compared, some improvements are observed. PN-MSIS-PET/ MSIS(IR) average detection limit ratios were 0.51 ± 0.49 (1.5 ± 1.9) for Agilent and 2.3 ± 2.3 for ARCOS. Detection limit (Tables 3.12-3.17), calculated here as 3 times the standard deviation of the average signal intensity of at least 10 consecutive blanks divided by the slope of the calibration curve, is directly proportional to the noise level, and inversely proportional to sensitivity. Therefore, an improvement in detection limit but a degradation of sensitivity would suggest that the noise is reduced more in the MSIS(IR) method than the PN-MSIS-PET method, which follows from the notion that IR heating is more uniform than convective heating provided by heating tape [2]. This is the case for the ARCOS and Agilent axial view MSIS(IR) methods, while the lateral view on Agilent saw worsened results for both sensitivity and detection limit in comparison to PN-MSIS-PET.

In order to ensure any observed sensitivity increase was solely due to heating of the PET, and not due to a change in nebuliser, nor attributed to the products and by-products of HG with MSIS, all MSIS(IR) setups were compared to conventional MSIS on the same instrument, in the same mode. This comparison had not been done in the work by Asfaw, which should be noted in order to avoid drawing conclusions about heating tape vs. IR heating on MSIS. When compared to the conventional MSIS Dual Mode experiment on ARCOS in this work, PN-MSIS-PET experienced a sensitivity degradation, with a PN-MSIS-PET/ conventional MSIS ratio of 0.75 ± 0.31. Comparisons of Agilent conventional MSIS vs. MSIS(IR) gave average sensitivity increases of 1.2 ± 1.2 (1.2 ± 0.5), 4.1 ± 4.1 (4.6 ± 5.2), 1.5 ± 0.8 (1.2 ± 0.08) for Dual Mode, HG Mode, and Nebulisation Mode, respectively. Average detection limit improvements for conventional MSIS vs. MSIS(IR) on Agilent were 1.1 ± 0.4 (2.4 ± 4.6), 4.2 ± 4.0 (7 ± 10), and 2.2 ± 1.0 (1.3 ± 0.5) for Dual Mode, HG Mode, and Nebulisation Mode. For ARCOS when comparing conventional MSIS to MSIS(IR), infrared heating changed sensitivity by factors of 0.45 ± 0.27 (an average degradation) and 1.8 ± 1.2 (an average improvement) for Dual Mode and HG Mode, respectively, while average detection limit improved by 2.1 ± 1.9 for Dual Mode and 1.7 ± 1.5 for HG Mode.

When comparing ARCOS to Agilent results, there is an average sensitivity increase when using ARCOS over Agilent of 8 ± 1 (2.4 ± 3.0), and 16 ± 11 (8 ± 11) for Dual Mode and HG Mode, respectively, where the axial comparison results for Agilent are again shown in brackets. In terms of detection limits, these ratios are 7.0 ± 8.5 (2.3 ± 3.0) for Dual Mode, and 6.3 ± 5.8 (3.6 ± 5.7) for HG Mode, showing an improvement for the ARCOS setup over the Agilent setup. The greater improvements of ARCOS experiments over Agilent experiments can be attributed to the fact that only 3 cm of the torch injector were heated with the Agilent setup, while 7 cm of injector length were heated on the ARCOS. This additional 4 cm of heating is necessary to prevent the pre-vaporized sample from rapidly cooling in the path length between the IR heated region and the plasma. Furthermore, the ARCOS setup could be heated at an optimal temperature of 175 °C, while the Agilent setups were only heated at 80 °C and 100 °C, as higher temperatures overloaded the plasma and affected the upper plastic casing of the torch. As follows from previous work [2, 9, 20], higher heater temperatures result in more efficient sample introduction efficiency, as the aerosol is more thoroughly vaporized prior to reaching the plasma. Additionally, all above comparisons indicate that axial view typically provided greater sensitivities and lower detection limits than lateral view on the Agilent instrument, which agrees with the principle that axial view gives lower detection limits for most elements, but lateral view is more robust [5].

The average ratios above demonstrate that although there may be a large improvement in analytical performance for certain elements, other elements may see a degradation in sensitivity or detection limit since compromise conditions were chosen when optimizing for the 37 elements. Therefore, rather than averaging ratios, improvement factors may also be viewed element-by-element while comparing ionic and atomic lines. Sensitivity enhancements are typically greater for ionic lines than atomic lines, as lines with a higher total excitation potential (TEP) are more sensitive to changes in the excitation conditions of the ICP [30, 31]. For instance, when comparing the Agilent MSIS(IR) results to PN, there is a detection limit improvement factor when using a recommended ionic line over a

recommended atomic line of 2.8 (4.0), 4.5 (0.82), and 2.0 (3.0) for Be, Cu, and Zn, respectively, in Dual Mode, 2.1 (5.8) for Be in HG Mode, and 0.83 (1.2), 2.5 (1.2), 2.7 (2.5) for Mg, Cu, and Zn, respectively, in Nebulisation Mode. These factors of improvement in terms of sensitivity are 1.2 (1.0), 1.6 (2.2), and 1.4 (1.5) for Be, Cu, and Zn, respectively, in Dual Mode, 1.2 (1.0) for Be in HG Mode, and 1.2 (1.2), 1.6 (2.2), and 1.4 (1.5) for Mg, Cu, and Zn, respectively, in Nebulisation Mode. Again, lateral view results are given first and axial view results are given in brackets.

The most significant detection limit improvements with Nebulisation Mode were in axial view with setup 2, in which Hg, Al, Cd, and P improved by factors of 60, 20, 10, and 9, respectively, when compared to PN in axial view (column B/H in Table 3.17). These same levels of improvement are not seen in lateral view (column A/G in Table 3.17), highlighting the greater improvement IR-heating had on axial view over lateral view. On the ARCOS instrument, the largest improvements in detection limit in Dual Mode are factors of 170, 130, 70, and 40 for the hydrides of Sb, Bi, As, and Ge, respectively, when compared to PN. Additionally, comparing to conventional MSIS gives a 10-fold improvement for the non-hydride Li. In HG Mode on ARCOS, MSIS(IR) improved detection limit over PN by factors of 100, 80, 70, 33, 20, and 20 for the hydride-generating elements Sb, Ge, As, Bi, Hg, and Se, respectively. On the Agilent instrument in Dual Mode, factors of improvement for detection limit with MSIS(IR) over PN are 15 (83) for As, 30 (43) for Bi, 17 (38) for Ge, 20 (86) for Hg, 3300 (3500) for S, and 25 (50) for Sb, where improvement ratios for lateral view are listed first, and axial factors are listed second. Additionally, axial view saw additional improvements with Zn having a 10-fold improvement in detection limit, and Al having a 20-fold improvement. In HG Mode, detection limit improved by factors of 38 (170) for As, 75 (100) for Bi, 25 (60) for Ge, 40 (86) for Hg, 63 (150) for Sb, and 10 (10) for Se in comparison to PN. Axial view had an additional 20-fold improvement for Cd.

While typically Be is not regarded as a hydride-generating element, this work indicated that beryllium hydride could be generated by MSIS(IR) in Dual and HG Modes. When compared to

conventional MSIS, MSIS(IR) gave a 27-fold improvement in detection limit of Be in Dual Mode in axial view, and up to a 25-fold improvement with HG Mode in axial view. Given that the detection limits of Be are much higher in conventional MSIS, it is possible that high temperatures of the PET in combination with the hydride-generating reaction between $NaBH_4$ and HNO_3 resulted in the production of beryllium hydride. This is supported by the fact that all analyzed lines of Be experienced an improvement (columns E/G and F/H of Table 3.15). It should be noted that Be was not detectable by conventional MSIS on ARCOS, but was detected with MSIS(IR). Hence, improvement ratios are not listed. According to the literature, the gaseous BeH_2 molecule has been synthesized before by means of an electrical discharge inside a high-temperature furnace [32], detected via its IR spectrum when stabilized in an argon matrix [33], and found as an impurity on a silicon crystal [34]. Hence, the formation of the free, gaseous BeH_2 molecule is an area of little discovery, despite the interest it inspires in ab initio quantum mechanics [32].

Moreover, several elements were previously undetectable in Dual and HG Modes when using MSIS without IR heating. These undetectable elements are listed as “n/a” throughout the following tables, while “---“ indicates that the element was not determined for the given experiment. As these undetected elements were not listed in Asfaw’s work, it is unclear as to whether they could be detected when using a heating tape setup. With most of these previously undetectable elements being hydride-forming, and the majority of improvements with IR heating being seen in hydride-forming elements, it may be asserted that IR heating provided a greater improvement on the detection capabilities on hydride-generating analytes. In the case of improvements for non-hydride-generating elements, the plasma excitation efficiency likely was improved by the combination of MSIS and PET, i.e. because a higher electron number density is reported with the simultaneous introduction of aerosol and hydride [35]. This results in all elements being more efficiently excited.

Precision, measured as the relative standard deviation (RSD, n = 10 for Dual Mode and HG Mode, n = 5 for Nebulisation Mode) of a 100 ng mL^{-1} is listed for all experiments in Table 3.18-3.20). The average precisions for all elements with MSIS(IR) were 2.3 ± 2.1% for Dual Mode, and 1.3 ± 1.1% for HG Mode on ARCOS. On the Agilent instrument, average precisions were 3.1 ± 3.7% (2.6 ± 2.2%), 6.3 ± 7.2% (7.2 ± 12.6%), and 5.7 ± 7.0% (3.1 ± 4.2%) for Dual Mode, HG Mode, and Nebulisation Mode, respectively, with lateral values listed first, and axial values in brackets. Comparing MSIS(IR) Dual Mode on ARCOS to the average instrumental precision of 2.4 ± 1.5% (n = 5) for PN-MSIS-PET on the same instrument, it is clear that IR heating provides similar precision values as heating tape. Furthermore, the Dual Mode results correspond with other reports of RSD for the simultaneous determination of hydride-forming and non hydride-forming elements by ICP-OES [36]. During the MSIS(IR) experiments, no drift in line emission was observed, indicating that if decomposition of unstable hydrides occurred, it did not have an apparent negative impact.

Table 3.6: Sensitivity (cps per ng mL^{-1}) for MSIS in Dual Mode

	A	B	C	D	E	F	G	H	I	J
Element Line (nm)	**PN (ARCOS)**	**PN Lateral (Agilent)**	**PN Axial (Agilent)**	**PN-MSIS-PET [9] ARCOS**	**MSIS Conventional ARCOS**	**MSIS Conventional Lateral (Agilent)**	**MSIS Conventional Axial (Agilent)**	**MSIS IR Lateral (Agilent)**	**MSIS IR Axial (Agilent)**	**MSIS IR (ARCOS)**
Al II 167.019	160	3.4	0.57	---	210	8	6.9	14	11	52
As I 189.042	16	0.49	0.42	280	510	13	46	15	44	280
Be I 234.861	2300	60	58	990	1400	78	200	110	250	740
Be II 313.042	8900	1200	1100	---	5500	1700	3700	2500	4800	2600
Be II 313.107	4300	600	600	---	2800	850	1800	1200	2400	1300
Bi I 223.061	11	0.46	0.84	220	590	9.5	44	12	58	340
Cd II 214.439	410	12	12	410	450	20	74	33	100	79
Co II 228.615	310	6.9	9	160	130	10	36	15	46	44
Cr II 267.716	84	11	15	60	60	15	49	21	63	24
Cu II 224.700	47	0.74	0.95	40	37	1.1	4.4	1.8	5.5	12
Cu I 324.754	230	8.2	20	---	110	9.5	40	12	51	69
Eu II 420.505	750	72	190	---	290	73	250	83	330	210
Fe II 238.204	210	13	17	110	160	4.6	16	6.4	20	55
Ga I 294.364	19	2	4.3	---	6.7	2.5	11	2.8	14	5.1
Ge I 265.117	11	0.28	0.59	---	260	6.6	33	8	35	210
Hg I 184.887	95	3.7	3	1500	3500	75	240	140	340	1700
In II 230.606	7.9	0.51	0.83	---	2.9	0.53	2.7	0.7	2.4	3.3
K I 766.491	0.17	1.4	38	---	n/a	n/a	27	n/a	86	n/a
La II 408.672	280	22	55	---	100	25	82	31	110	76
Li I 670.783	160	83	2000	---	54	120	8100	130	8900	50
Mg II 280.270	1400	55	72	---	1100	80	270	130	450	450
Mg I 285.213	180	6.1	15	---	110	7.8	45	12	50	59
Mn II 257.610	610	57	76	310	420	77	260	100	310	180
Mo II 202.032	65	2.6	3.3	40	46	3.4	12	4.8	16	16
Ni II 231.604	81	1.8	2.4	70	64	2.8	10	4	13	21
P I 177.434	11	0.38	0.18	---	10	0.73	1.2	0.81	1.9	2.7

Pb II 220.353	16	1.2	1.6	13	15	1.9	8.2	2.9	11	4.3
S I 180.669	13	0.17	0.11	---	13000	610	1100	1000	770	2100
Sb I 217.582	11	0.26	0.42	---	760	9.2	39	12	50	650
Se I 196.026	9.6	0.49	0.47	---	n/a	n/a	n/a	3	6.6	77
Si I 251.611	44	1	1.7	---	25	1.1	5.8	1.2	4.7	n/a
Sr II 421.552	5400	550	1300	---	2500	610	2100	750	2800	1500
Ti II 334.941	580	81	140	---	300	98	300	130	400	150
V II 292.464	740	68	100	50	470	9.4	32	13	43	220
Y II 371.029	1700	35	78	---	870	41	150	55	200	450
Zn II 206.200	260	1.7	1.6	160	180	2.8	10	4.5	13	36
Zn I 213.857	360	14	16	---	280	19	65	26	82	92
Zr II 339.198	300	17	32	---	160	19	71	27	92	77

Table 3.7: Sensitivity Ratios for MSIS in Dual Mode

Element Line (nm)	J/A	J/E	J/D	H/D	I/D	H/B	I/C	H/F	I/G
Al II 167.019	0.32	0.24	---	---	---	4.3	19	1.8	1.5
As I 189.042	17	0.55	1	0.054	0.16	31	100	1.2	0.97
Be I 234.861	0.32	0.52	0.75	0.11	0.26	1.8	4.4	1.4	1.2
Be II 313.042	0.3	0.48	---	---	---	2.1	4.4	1.5	1.3
Be II 313.107	0.31	0.48	---	---	---	2.1	4	1.5	1.3
Bi I 223.061	31	0.58	1.6	0.053	0.26	26	69	1.2	1.3
Cd II 214.439	0.19	0.18	0.19	0.08	0.25	2.7	8.4	1.7	1.4
Co II 228.615	0.14	0.35	0.27	0.094	0.29	2.2	5.1	1.5	1.3
Cr II 267.716	0.29	0.4	0.4	0.35	1.1	1.9	4.1	1.4	1.3
Cu II 224.700	0.27	0.34	0.31	0.044	0.14	2.4	5.8	1.6	1.3
Cu I 324.754	0.3	0.61	---	---	---	1.5	2.6	1.3	1.3
Eu II 420.505	0.28	0.74	---	---	---	1.2	1.7	1.1	1.3
Fe II 238.204	0.26	0.34	0.5	0.058	0.18	0.48	1.1	1.4	1.3
Ga I 294.364	0.28	0.77	---	---	---	1.4	3.2	1.1	1.2
Ge I 265.117	19	0.83	---	---	---	28	59	1.2	1.1
Hg I 184.887	18	0.48	1.1	0.091	0.23	36	120	1.8	1.4

In II 230.606	0.41	1.1	---	---	---	1.4	2.9	1.3	0.89
K I 766.491	1.3	---	---	---	---	---	2.3	---	3.2
La II 408.672	0.27	0.73	---	---	---	1.4	2	1.2	1.3
Li I 670.783	0.31	0.93	---	---	---	1.5	4.5	1.1	1.1
Mg II 280.270	0.32	0.39	---	---	---	2.4	6.2	1.6	1.7
Mg I 285.213	0.33	0.52	---	---	---	2	3.4	1.5	1.1
Mn II 257.610	0.29	0.42	0.58	0.33	1	1.8	4.1	1.3	1.2
Mo II 202.032	0.24	0.35	0.4	0.12	0.39	1.8	4.7	1.4	1.3
Ni II 231.604	0.27	0.33	0.31	0.058	0.18	2.2	5.3	1.4	1.2
P I 177.434	0.24	0.26	---	---	---	2.1	10	1.1	1.5
Pb II 220.353	0.28	0.3	0.33	0.23	0.82	2.5	6.5	1.5	1.3
S I 180.669	170	0.16	---	---	---	6000	7100	1.7	0.72
Sb I 217.582	59	0.84	---	---	---	46	120	1.3	1.3
Se I 196.026	8.1	---	---	---	---	6	14	---	---
Si I 251.611	---	---	---	---	---	1.1	2.8	1.1	0.81
Sr II 421.552	0.27	0.6	---	---	---	1.4	2.1	1.2	1.3
Ti II 334.941	0.27	0.5	---	---	---	1.7	2.8	1.4	1.3
V II 292.464	0.3	0.48	4.5	0.26	0.86	0.19	0.41	1.4	1.3
Y II 371.029	0.26	0.52	---	---	---	1.6	2.6	1.3	1.3
Zn II 206.200	0.14	0.2	0.23	0.028	0.079	2.6	7.9	1.6	1.3
Zn I 213.857	0.26	0.33	---	---	---	1.8	5.1	1.4	1.3
Zr II 339.198	0.26	0.49	---	---	---	1.6	2.8	1.4	1.3

Table 3.8: Sensitivity (cps per ng mL^{-1}) for MSIS in HG Mode

	A	B	C	D	E	F	G	H	I
Element Line (nm)	**PN (ARCOS)**	**PN Lateral (Agilent)**	**PN Axial (Agilent)**	**MSIS Conventional (ARCOS)**	**MSIS Conventional Lateral (Agilent)**	**MSIS Conventional Axial (Agilent)**	**MSIS IR Lateral (Agilent)**	**MSIS IR Axial (Agilent)**	**MSIS IR (ARCOS)**
As I 189.042	16	0.49	0.42	490	29	110	35	110	640
Be I 234.861	2300	60	58	n/a	0.11	0.3	1.1	3.9	30
Be II 313.042	8900	1200	1100	n/a	3	6.8	28	78	74
Be II 313.107	4300	600	600	n/a	1.7	4.5	13	37	66
Bi I 223.061	11	0.46	0.84	390	19	94	15	69	260
Cd II 214.439	410	12	12	n/a	n/a	n/a	23	130	61
Ge I 265.117	11	0.28	0.59	160	12	72	13	63	350
Hg I 184.887	95	3.7	3	1900	110	350	160	430	2400
Pb II 220.353	16	1.2	1.6	n/a	n/a	n/a	n/a	0.39	16
Sb I 217.582	11	0.26	0.42	450	16	71	18	76	620
Se I 196.026	9.6	0.49	0.47	19	n/a	n/a	5.2	10	77

Table 3.9: Sensitivity Ratios for MSIS in HG Mode

Element Line (nm)	I/A	I/D	G/B	H/C	G/E	H/F
As I 189.042	40	1.3	72	260	1.2	1
Be I 234.861	0.013	---	0.019	0.068	10	13
Be II 313.042	0.0083	---	0.023	0.07	9.4	11
Be II 313.107	0.016	---	0.022	0.062	7.7	8.2
Bi I 223.061	23	0.67	34	82	0.82	0.73
Cd II 214.439	0.15	---	1.9	10	---	---
Ge I 265.117	31	2.1	47	110	1.1	0.87
Hg I 184.887	25	1.2	42	150	1.4	1.2
Pb II 220.353	1	---	---	0.24	---	---
Sb I 217.582	56	1.4	69	180	1.1	1.1
Se I 196.026	8.1	4	10	22	---	---

Table 3.10: Sensitivity (cps per ng mL^{-1}) for MSIS in Nebulisation Mode with Agilent 5100

	A	B	C	D	E	F	G	H
Element Line (nm)	**PN Lateral (Agilent)**	**PN Axial (Agilent)**	**MSIS Conv. Lateral**	**MSIS Conv. Axial**	**MSIS Setup 1 (IR) Lateral**	**MSIS Setup 1 (IR) Axial**	**MSIS Setup 2 (IR) Lateral**	**MSIS Setup 2 (IR) Axial**
Al II 167.019	3.4	0.57	7.5	6.3	11	8.2	10	7.9
As I 189.042	0.49	0.42	0.54	1.5	0.61	2.1	0.59	1.9
Be II 313.042	1200	1100	1000	2900	1900	3700	1600	3600
Bi I 223.061	0.46	0.84	0.37	2	0.48	2.9	0.58	2.4
Cd II 214.439	12	12	16	55	24	73	21	70
Co II 228.615	6.9	9	7	28	11	37	10	35
Cr II 267.716	11	15	10	41	17	51	15	50
Cu II 224.700	0.74	0.95	0.87	3.2	1.4	4.4	1.2	4.1
Cu I 324.754	8.2	20	5.7	33	9.4	40	8.5	40
Eu II 420.505	72	190	34	220	64	260	59	270
Fe II 238.204	13	17	13	51	20	64	18	63
Ga I 294.364	2	4.3	0.73	9.3	2.3	12	2	11
Ge I 265.117	0.28	0.59	0.21	1.3	0.41	1.5	0.36	1.5
Hg I 184.887	3.7	3	70	170	74	200	73	190
In II 230.606	0.51	0.83	0.41	2.1	0.63	3.1	0.65	3.2
K I 766.491	1.4	38	n/a	23	0.66	27	0.18	29
La II 408.672	22	55	14	76	25	87	22	91
Li I 670.783	83	2000	62	7400	87	9400	64	9800
Mg II 280.270	55	72	54	220	88	280	78	280
Mg I 285.213	6.1	15	5.3	38	8.2	47	7.2	49
Mn II 257.610	57	76	51	210	83	260	74	260
Mo II 202.032	2.6	3.3	2.1	9.1	3.7	12	3.3	11
Ni II 231.604	1.8	2.4	2	7.9	3.2	10	3	9.8
P I 177.434	0.38	0.18	0.47	0.98	0.79	1.3	0.66	1.2
Pb II 220.353	1.2	1.6	1.8	6.3	2.3	8.3	2	7.9
S I 180.669	0.17	0.11	0.081	0.37	0.34	0.8	0.18	0.57
Sb I 217.582	0.26	0.42	0.059	1	0.39	1.3	0.33	1.3

Se I 196.026	0.49	0.47	0.63	1.8	0.93	2.5	0.8	2.3
Si I 251.611	1	1.7	0.84	4	1.2	5.3	1.2	4.9
Sr II 421.552	550	1300	340	1900	590	2300	540	2300
Ti II 334.941	81	140	58	250	100	310	90	310
V II 292.464	68	100	5.8	26	9.9	32	8.8	32
Y II 371.029	35	78	24	130	42	160	38	160
Zn II 206.200	1.7	1.6	2.3	7.3	3.5	9.8	3	9.3
Zn I 213.857	14	16	14	53	21	67	18	65
Zr II 339.198	17	32	11	58	19	71	18	72

Table 3.11: Sensitivity Ratios for MSIS in Nebulisation Mode (Agilent 5100)

Element Line (nm)	E/A	G/A	E/C	G/C	F/B	H/B	F/D	H/D
Al II 167.019	3.3	3	1.5	1.3	15	14	1.3	1.3
As I 189.042	1.3	1.2	1.1	1.1	4.9	4.4	1.4	1.3
Be II 313.042	1.6	1.4	1.8	1.6	3.4	3.3	1.3	1.2
Bi I 223.061	1	1.3	1.3	1.6	3.4	2.9	1.4	1.2
Cd II 214.439	2	1.8	1.5	1.4	5.9	5.6	1.3	1.3
Co II 228.615	1.6	1.5	1.6	1.4	4.1	3.9	1.3	1.2
Cr II 267.716	1.5	1.3	1.6	1.5	3.3	3.2	1.2	1.2
Cu II 224.700	1.8	1.6	1.6	1.3	4.6	4.3	1.4	1.3
Cu I 324.754	1.1	1	1.7	1.5	2	2	1.2	1.2
Eu II 420.505	0.88	0.81	1.9	1.7	1.3	1.4	1.2	1.2
Fe II 238.204	1.5	1.4	1.6	1.5	3.7	3.6	1.3	1.2
Ga I 294.364	1.1	1	3.1	2.8	2.7	2.6	1.3	1.2

Ge I 265.117	1.4	1.3	1.9	1.7	2.5	2.5	1.2	1.2
Hg I 184.887	20	20	1.1	1	67	65	1.2	1.1
In II 230.606	1.2	1.3	1.5	1.6	3.7	3.8	1.5	1.5
K I 766.491	0.47	0.12	---	---	0.72	0.76	1.2	1.3
La II 408.672	1.1	0.99	1.8	1.6	1.6	1.7	1.1	1.2
Li I 670.783	1	0.78	1.4	1	4.8	5	1.3	1.3
Mg II 280.270	1.6	1.4	1.6	1.4	3.9	3.9	1.2	1.2
Mg I 285.213	1.3	1.2	1.6	1.4	3.3	3.3	1.2	1.3
Mn II 257.610	1.5	1.3	1.6	1.5	3.5	3.5	1.2	1.2
Mo II 202.032	1.4	1.2	1.7	1.5	3.6	3.5	1.3	1.3
Ni II 231.604	1.8	1.6	1.6	1.5	4.4	4.1	1.3	1.2
P I 177.434	2.1	1.7	1.7	1.4	7	6.8	1.3	1.3
Pb II 220.353	1.9	1.7	1.3	1.1	5	4.8	1.3	1.3
S I 180.669	2	1	4.2	2.2	7.3	5.2	2.2	1.5
Sb I 217.582	1.5	1.3	6.7	5.5	3	3	1.2	1.2
Se I 196.026	1.9	1.6	1.5	1.3	5.3	4.8	1.4	1.2
Si I 251.611	1.2	1.1	1.5	1.4	3.1	2.9	1.3	1.2
Sr II 421.552	1.1	0.98	1.7	1.6	1.7	1.7	1.2	1.2
Ti II 334.941	1.2	1.1	1.7	1.6	2.2	2.2	1.2	1.2
V II 292.464	0.15	0.13	1.7	1.5	0.31	0.31	1.2	1.2
Y II 371.029	1.2	1.1	1.7	1.6	2	2.1	1.2	1.2

Zn II 206.200	2.1	1.8	1.5	1.3	6.1	5.9	1.3	1.3
Zn I 213.857	1.4	1.3	1.5	1.3	4.1	4	1.3	1.2
Zr II 339.198	1.1	1.1	1.7	1.6	2.2	2.2	1.2	1.2

Table 3.12: Detection Limits (ng/mL) for MSIS in Dual Mode

Ratio Label	**A**	**B**	**C**	**D**	**E**	**F**	**G**	**H**	**I**	**J**
Element Line (nm)	**PN (ARCOS)**	**PN Lateral (Agilent)**	**PN Axial (Agilent)**	**PN-MSIS-PET [9] ARCOS**	**MSIS Conventional ARCOS**	**MSIS Conventional Lateral (Agilent)**	**MSIS Conventional Axial (Agilent)**	**MSIS IR Lateral (Agilent)**	**MSIS IR Axial (Agilent)**	**MSIS IR (ARCOS)**
Al II 167.019	0.2	7	20	---	0.2	2	3	2	1	0.3
As I 189.042	7	30	50	0.2	0.2	2	0.4	2	0.6	0.1
Be I 234.861	0.1	0.7	0.1	0.2	0.1	0.5	0.4	0.6	0.2	0.1
Be II 313.042	0.09	0.1	0.06	---	0.2	0.03	0.8	0.03	0.03	0.09
Be II 313.107	0.2	0.2	0.06	---	0.3	0.1	0.07	0.05	0.06	0.2
Bi I 223.061	10	60	30	0.5	0.2	2	0.6	2	0.7	0.08
Cd II 214.439	0.4	0.6	2	0.5	0.3	0.7	0.6	0.7	0.3	0.4
Co II 228.615	1	8	3	0.7	2	3	2	6	1	1
Cr II 267.716	1	3	2	2	2	3	2	2	1	1
Cu II 224.700	2	20	7	3	5	10	4	10	4	3
Cu I 324.754	3	4	2	---	6	6	3	9	0.9	2
Fe II 238.204	0.7	3	2	8	1	2	1	4	1	1
Ge I 265.117	8	50	30	---	0.4	4	0.8	3	0.8	0.2
Hg I 184.887	0.6	4	6	0.1	0.01	0.3	0.2	0.2	0.07	0.3
K I 766.491	4000	200	4	---	n/a	n/a	20	n/a	6	n/a
Li I 670.783	3	10	0.1	---	10	10	0.1	10	0.1	1
Mg II 280.270	0.5	0.3	0.1	---	0.1	0.3	0.2	0.2	0.08	0.07
Mg I 285.213	0.6	7	1	---	0.8	4	0.5	4	1	0.7
Mn II 257.610	0.2	1	0.3	0.3	0.3	0.7	0.2	0.4	0.3	0.2
Mo II 202.032	2	10	9	2	2	20	3	9	2	2

Ni II 231.604	2	20	5	3	2	10	2	10	4	2
P I 177.434	3	60	90	---	6	30	10	20	8	8
Pb II 220.353	7	20	6	8	9	10	3	10	4	9
S I 180.669	5	100	70	---	0.004	0.04	0.02	0.03	0.02	0.06
Sb I 217.582	10	50	30	---	0.2	1	0.6	2	0.6	0.06
Se I 196.026	10	30	20	---	n/a	n/a	n/a	10	5	0.4
Si I 251.611	3	30	20	---	50	30	40	30	7	n/a
Sr II 421.552	0.3	0.2	0.06	---	0.7	0.3	0.08	0.3	0.1	0.2
Ti II 334.941	1	2	0.3	---	2	1	0.3	1	0.5	0.5
V II 292.464	0.3	1	0.3	1	0.8	4	3	4	1	0.2
Y II 371.029	0.9	0.9	0.3	---	2	0.8	0.4	1	0.3	0.5
Zn II 206.200	0.8	8	10	0.6	0.5	6	2	4	1	1
Zn I 213.857	0.3	2	2	---	0.6	1	0.8	2	0.6	0.4
Zr II 339.198	2	5	0.7	---	3	2	0.9	3	2	1

Table 3.13: Detection Limit Ratios for MSIS in Dual Mode

Element Line (nm)	A/J	E/J	D/J	D/H	D/I	B/H	C/I	F/H	G/I
Al II 167.019	0.67	0.67	---	---	---	3.5	20	1	3
As I 189.042	70	2	2	0.1	0.33	15	83	1	0.67
Be I 234.861	1	1.3	2	0.34	0.95	1.2	0.5	0.9	2
Be II 313.042	1	2.2	---	---	---	3.3	2	1	27
Be II 313.107	0.77	1.3	---	---	---	3.7	0.94	2.3	1.2
Bi I 223.061	130	2.5	6.3	0.25	0.71	30	43	1	0.86
Cd II 214.439	1	0.75	1.3	0.71	1.7	0.86	6.7	1	2
Co II 228.615	1	2	0.7	0.12	0.7	1.3	3	0.5	2
Cr II 267.716	1	2	2	1	2	1.5	2	1.5	2
Cu II 224.700	0.67	1.7	1	0.3	0.75	2	1.8	1	1
Cu I 324.754	1.5	3	---	---	---	0.44	2.2	0.67	3.3
Fe II 238.204	0.7	1	8	2	8	0.75	2	0.5	1
Ge I 265.117	40	2	---	---	---	17	38	1.3	1

Hg I 184.887	2	0.033	0.33	0.5	1.4	20	86	1.5	2.9
K I 766.491	---	---	---	---	---	---	0.67	---	3.3
Li I 670.783	3	10	---	---	---	1	1	1	1
Mg II 280.270	7.1	1.4	---	---	---	1.5	1.3	1.5	2.5
Mg I 285.213	0.86	1.1	---	---	---	1.8	1	1	0.5
Mn II 257.610	1	1.5	1.5	0.75	1	2.5	1	1.8	0.67
Mo II 202.032	1	1	1	0.22	1	1.1	4.5	2.2	1.5
Ni II 231.604	1	1	1.5	0.3	0.75	2	1.3	1	0.5
P I 177.434	0.38	0.75	---	---	---	3	11	1.5	1.3
Pb II 220.353	0.78	1	0.89	0.8	2	2	1.5	1	0.75
S I 180.669	83	0.067	---	---	---	3300	3500	1.3	1
Sb I 217.582	170	3.3	---	---	---	25	50	0.5	1
Se I 196.026	25	---	---	---	---	3	4	---	---
Si I 251.611	---	---	---	---	---	1	2.9	1	5.7
Sr II 421.552	1.5	3.5	---	---	---	0.67	0.6	1	0.8
Ti II 334.941	2	4	---	---	---	2	0.6	1	0.6
V II 292.464	1.5	4	5	0.25	1	0.25	0.3	1	3
Y II 371.029	1.8	4	---	---	---	0.9	1	0.8	1.3
Zn II 206.200	0.8	0.5	0.6	0.15	0.6	2	10	1.5	2
Zn I 213.857	0.75	1.5	---	---	---	1	3.3	0.5	1.3
Zr II 339.198	2	3	---	---	---	1.7	0.35	0.67	0.45

Table 3.14: Detection Limits (ng/mL) for MSIS in HG Mode

Ratio Label	A	B	C	D	E	F	G	H	I
Element Line (nm)	**PN (ARCOS)**	**PN Lateral (Agilent)**	**PN Axial (Agilent)**	**MSIS Conventional (ARCOS)**	**MSIS Conventional Lateral (Agilent)**	**MSIS Conventional Axial (Agilent)**	**MSIS IR Lateral (Agilent)**	**MSIS IR Axial (Agilent)**	**MSIS IR (ARCOS)**
As I 189.042	7	30	50	0.1	1	0.2	0.8	0.3	0.1
Be I 234.861	0.1	0.7	0.1	n/a	300	90	30	4	3
Be II 313.042	0.09	0.1	0.06	n/a	20	10	2	0.4	4
Be II 313.107	0.2	0.2	0.06	n/a	60	20	7	2	4
Bi I 223.061	10	60	30	0.1	0.9	0.3	0.8	0.3	0.3
Cd II 214.439	0.4	0.6	2	n/a	n/a	n/a	2	0.1	1
Ge I 265.117	8	50	30	0.3	2	0.4	2	0.5	0.1
Hg I 184.887	0.6	4	6	0.02	0.2	0.04	0.1	0.07	0.03
Pb II 220.353	7	20	6	n/a	n/a	n/a	n/a	80	4
Sb I 217.582	10	50	30	0.09	1	0.3	0.8	0.2	0.1
Se I 196.026	10	30	20	2	n/a	n/a	3	2	0.5

Table 3.15: Detection Limit Ratios for MSIS in HG Mode

Element Line (nm)	A/I	D/I	B/G	C/H	E/G	F/H
As I 189.042	70	1	38	170	1.3	0.67
Be I 234.861	0.036	---	0.024	0.026	8.8	22
Be II 313.042	0.023	---	0.05	0.15	10	25
Be II 313.107	0.042	---	0.026	0.035	8.2	12
Bi I 223.061	33	0.33	75	100	1.1	1
Cd II 214.439	0.4	---	0.3	20	---	---
Ge I 265.117	80	3	25	60	1	0.8
Hg I 184.887	20	0.67	40	86	2	0.57

Pb II 220.353	1.8	---	---	0.075	---	---
Sb I 217.582	100	0.9	63	150	1.3	1.5
Se I 196.026	20	4	10	10	---	---

Table 3.16: Detection Limits (ng/mL) for MSIS in Nebulisation Mode with Agilent 5100

Ratio Label	**A**	**B**	**C**	**D**	**E**	**F**	**G**	**H**
Element Line (nm)	**PN Lateral (Agilent)**	**PN Axial (Agilent)**	**MSIS Conv. Lateral**	**MSIS Conv. Axial**	**MSIS Setup 1 (IR) Lateral**	**MSIS Setup 1 (IR) Axial**	**MSIS Setup 2 (IR) Lateral**	**MSIS Setup 2 (IR) Axial**
Al II 167.019	7	20	3	2	3	4	3	1
As I 189.042	30	50	50	20	30	10	30	10
Be II 313.042	0.1	0.06	0.2	0.07	0.2	0.3	0.06	0.2
Bi I 223.061	60	30	80	20	110	10	60	10
Cd II 214.439	0.6	2	1	0.3	1	0.4	0.9	0.2
Co II 228.615	8	3	8	1	3	3	4	1
Cr II 267.716	3	2	7	1	4	1	3	1
Cu II 224.700	20	7	20	5	10	6	10	6
Cu I 324.754	4	2	20	3	10	3	5	2
Fe II 238.204	3	2	10	2	3	1	2	2
Ge I 265.117	50	30	160	30	50	20	80	30
Hg I 184.887	4	6	0.5	0.2	0.4	0.4	0.3	0.1
K I 766.491	200	4	n/a	20	500	20	100	20
Li I 670.783	10	0.1	20	0.6	5	0.2	60	0.3
Mg II 280.270	0.3	0.1	0.8	0.2	0.3	0.2	0.3	0.08
Mg I 285.213	7	1	10	0.8	6	1	6	0.9
Mn II 257.610	1	0.3	1	0.4	1	0.5	0.5	0.4
Mo II 202.032	10	9	30	3	9	3	8	2
Ni II 231.604	20	5	20	5	20	5	8	3
P I 177.434	60	90	30	20	40	30	30	10
Pb II 220.353	20	6	30	5	20	5	10	7
S I 180.669	100	70	190	50	160	70	80	30
Sb I 217.582	50	30	100	30	80	30	70	20

Se I 196.026	30	20	70	10	50	20	30	10
Si I 251.611	30	20	40	8	60	120	20	7
Sr II 421.552	0.2	0.06	0.7	0.08	0.7	0.1	0.6	0.2
Ti II 334.941	2	0.3	3	1	1	0.9	2	0.8
V II 292.464	1	0.3	20	2	10	5	6	6
Y II 371.029	0.9	0.3	3	0.5	1	0.5	1	0.5
Zn II 206.200	8	10	6	2	6	1	3	2
Zn I 213.857	2	2	6	1	2	0.7	2	1
Zr II 339.198	5	0.7	10	3	5	2	5	3

Table 3.17: Detection Limit Ratios for MSIS in Nebulisation Mode (Agilent 5100)

Element Line (nm)	A/E	A/G	C/E	C/G	B/F	B/H	D/F	D/H
Al II 167.019	2.3	2.3	1	1	5	20	0.5	2
As I 189.042	1	1	1.7	1.7	5	5	2	2
Be II 313.042	0.5	1.7	1	3.3	0.2	0.3	0.2	0.4
Bi I 223.061	0.5	1	0.7	1.3	3	3	2	2
Cd II 214.439	0.6	0.7	1	1.1	5	10	0.8	1.5
Co II 228.615	2.7	2	2.7	2	1	3	0.3	1
Cr II 267.716	0.8	1	1.8	2.3	2	2	1	1
Cu II 224.700	2	2	2	2	1.2	1.2	0.8	0.8
Cu I 324.754	0.4	0.8	2	4	0.7	1	1	1.5
Fe II 238.204	1	1.5	3.3	5	2	1	2	1
Ge I 265.117	1	0.6	3.2	2	1.5	1	1.5	1
Hg I 184.887	10	13	1.3	1.7	15	60	0.5	2
K I 766.491	0.4	2	---	---	0.2	0.2	1	1
Li I 670.783	2	0.2	4	0.3	0.5	0.3	3	2
Mg II 280.270	1	1	2.7	2.7	0.5	1.3	1	2.5
Mg I 285.213	1.2	1.2	1.7	1.7	1	1.1	0.8	0.9
Mn II 257.610	1	2	1	2	0.6	0.8	0.8	1
Mo II 202.032	1.1	1.3	3.3	3.8	3	4.5	1	1.5
Ni II 231.604	1	2.5	1	2.5	1	1.7	1	1.7

P I 177.434	1.5	2	0.8	1	3	9	0.7	2
Pb II 220.353	1	2	1.5	3	1.2	0.9	1	0.7
S I 180.669	0.6	1.3	1.2	2.4	1	2.3	0.7	1.7
Sb I 217.582	0.6	0.7	1.3	1.4	1	1.5	1	1.5
Se I 196.026	0.6	1	1.4	2.3	1	2	0.5	1
Si I 251.611	0.5	1.5	0.7	2	0.2	2.9	0.07	1.1
Sr II 421.552	0.3	0.3	1	1.2	0.6	0.3	0.8	0.4
Ti II 334.941	2	1	3	1.5	0.3	0.4	1.1	1.3
V II 292.464	0.1	0.2	2	3.3	0.06	0.05	0.4	0.3
Y II 371.029	0.9	0.9	3	3	0.6	0.6	1	1
Zn II 206.200	1.3	2.7	1	2	10	5	2	1
Zn I 213.857	1	1	3	3	2.9	2	1.4	1
Zr II 339.198	1	1	2	2	0.4	0.2	1.5	1

Table 3.18: Instrumental precision (% relative standard deviation for 100ppb, n=10) for MSIS in Dual Mode

Element Line (nm)	PN (ARCOS)	PN Lateral (Agilent)	PN Axial (Agilent)	PN-MSIS-PET [9] ARCOS (n = 5)	MSIS Conventional ARCOS	MSIS Conventional Lateral (Agilent)	MSIS Conventional Axial (Agilent)	MSIS IR Lateral (Agilent)	MSIS IR Axial (Agilent)	MSIS IR (ARCOS)
Al II 167.019	1	1.7	1.4	---	3.3	3	1.6	1.9	1.8	12
As I 189.042	0.5	2	1.5	4.1	0.96	1.6	1.5	1.2	1.8	1.4
Be I 234.861	1.2	0.93	1.1	1.5	2	1	1.6	0.85	0.3	3.1
Be II 313.042	1.3	0.87	0.41	---	1.9	1.1	1.5	2.1	1	3.8
Be II 313.107	1.3	0.93	0.46	---	1.7	1.1	1.5	1.9	1.1	3.7
Bi I 223.061	0.49	7	3.7	1.4	1.4	1.6	2.9	0.41	3.8	2.1
Cd II 214.439	0.8	0.85	0.7	1.4	0.94	0.89	1.5	0.29	0.61	6.9
Co II 228.615	0.53	0.32	0.61	2.3	0.67	1.7	2.3	0.7	2.5	1.5
Cr II 267.716	0.73	1.3	1.4	2	0.49	1.1	1.6	1.3	0.26	1.4
Cu II 224.700	0.63	0.83	1.2	1.9	0.66	6.8	1.9	5.6	2.8	1.2
Cu I 324.754	0.54	1.5	0.98	---	0.51	1.3	2	1.1	0.95	1.3
Eu II 420.505	0.6	0.8	1.4	---	0.51	2.1	5.7	2.2	2.1	1.1

Fe II 238.204	0.73	0.7	0.54	1.6	0.99	1.3	1.3	1.4	0.49	1.7
Ga I 294.364	0.61	2.4	1.2	---	0.98	9.6	3.4	15	3.9	0.84
Ge I 265.117	0.46	5	1.3	---	1.1	4.2	2.5	2	3.3	2.2
Hg I 184.887	2.2	5.3	6	1.3	2.1	1.6	2.3	1.1	8.1	0.97
In II 230.606	0.42	5.8	2.2	---	0.96	11	7.7	18	9.3	0.53
K I 766.491	0.72	1.3	1.5	---	1	3.8	9.6	3.5	5.1	0.82
La II 408.672	0.5	0.78	0.78	---	0.63	2.1	5.2	3.6	3.4	0.97
Li I 670.783	0.49	1	0.35	---	0.78	1.2	1.7	0.99	1.5	0.83
Mg II 280.270	0.67	0.52	0.29	---	4.1	2.4	5.9	3.5	5.2	3
Mg I 285.213	0.45	0.57	0.73	---	3.3	1.6	3.7	4.3	4.8	1.5
Mn II 257.610	0.62	0.52	0.91	1.4	2.2	1.3	1.5	0.72	0.99	3.3
Mo II 202.032	0.83	0.79	0.8	1.6	0.98	3.2	1.7	3.3	1.5	1.7
Ni II 231.604	0.74	0.92	0.84	1.1	0.5	2.5	1.7	3	3.1	1.2
P I 177.434	0.69	2	4.4	---	0.82	17	7.1	10	7.4	1.5
Pb II 220.353	0.99	2	0.96	3.7	0.81	1.7	1.7	5	2.6	0.86
S I 180.669	0.73	3.7	3.7	---	2.7	1.1	1.2	1	0.69	3.2
Sb I 217.582	0.41	4.7	2.2	---	1.7	3	2.6	1.6	4.9	1.8
Se I 196.026	0.55	2.5	1.5	---	9.4	6.1	6.8	3	3.3	1.3
Si I 251.611	0.63	1.4	0.82	---	0.83	4.2	0.8	6.4	3.2	5.8
Sr II 421.552	1.4	1.3	0.65	---	1.1	2.6	4.6	1.4	1.4	3.4
Ti II 334.941	0.7	0.65	1.2	---	0.67	0.79	2.4	1.2	1.6	1.8
V II 292.464	0.63	0.57	1	2.8	1.7	1.2	0.82	3.7	1.1	2.4
Y II 371.029	0.81	0.56	0.47	---	0.61	1.1	1.6	1.4	0.87	1.8
Zn II 206.200	0.6	0.74	0.69	1.4	1.6	2.8	1.6	1.6	0.74	2.1
Zn I 213.857	0.56	0.64	0.69	---	1.6	1.4	1.2	1	0.67	3
Zr II 339.198	0.55	0.54	0.33	---	0.4	3.6	1.6	1.7	0.58	1.1

Table 3.19: Instrumental precision (% relative standard deviation for 100ppb, n=10) for MSIS in HG Mode

Element Line (nm)	PN (ARCOS)	PN Lateral (Agilent)	PN Axial (Agilent)	MSIS Conventional (ARCOS)	MSIS Conventional Lateral (Agilent)	MSIS Conventional Axial (Agilent)	MSIS IR Lateral (Agilent)	MSIS IR Axial (Agilent)	MSIS IR (ARCOS)
As I 189.042	0.5	2	1.5	0.9	2.4	2.1	1.7	0.79	1
Be I 234.861	1.2	0.93	1.1	0.51	16	15	15	4.3	0.83
Be II 313.042	1.3	0.87	0.41	0.64	34	10	7.3	1	0.73
Be II 313.107	1.3	0.93	0.46	0.55	15	7.9	5.3	1.4	0.73
Bi I 223.061	0.49	7	3.7	0.43	1.5	3	2.6	1.1	2.4
Cd II 214.439	0.8	0.85	0.7	2.7	13	10	3.7	1.8	1.8
Co II 228.615	0.53	0.32	0.61	0.66	20	13	11	21	0.98
Ge I 265.117	0.46	5	1.3	1.5	5.3	1.7	1.5	1.4	1.6
Hg I 184.887	2.2	5.3	6	1.3	1.5	1.5	1.4	6.1	0.8
Pb II 220.353	0.99	2	0.96	0.97	23	16	24	43	0.48
Sb I 217.582	0.41	4.7	2.2	0.41	0.93	2	0.77	0.32	0.37
Se I 196.026	0.55	2.5	1.5	5.7	5.1	6.6	0.79	3.9	4.1

Table 3.20: Instrumental precision (% relative standard deviation for 100ppb, n=5) for MSIS in Nebulisation Mode with Agilent 5100

Element Line (nm)	PN Lateral (Agilent)	PN Axial (Agilent)	MSIS Conv. Lateral	MSIS Conv. Axial	MSIS Setup 1 (IR) Lateral	MSIS Setup 1 (IR) Axial	MSIS Setup 2 (IR) Lateral	MSIS Setup 2 (IR) Axial
Al II 167.019	1.7	1.4	2.3	3.2	2.6	1.8	1.7	1.5
As I 189.042	2	1.5	7.9	9.1	9.9	5.2	6.7	6.6
Be II 313.042	0.87	0.41	3.1	1.7	2.2	3	1.2	0.32
Bi I 223.061	7	3.7	31	8	32	8.2	9.8	8.1
Cd II 214.439	0.85	0.7	2.4	1.9	1.4	1.1	1.7	0.81
Co II 228.615	0.32	0.61	6.4	2.6	3.3	2.7	2.3	0.49
Cr II 267.716	1.3	1.4	3.2	2.1	1.6	1.7	1.7	0.49
Cu II 224.700	0.83	1.2	5.6	3.5	5.4	1.7	6.1	3.1
Cu I 324.754	1.5	0.98	1.9	1.6	2.5	1.5	2.4	0.68

Eu II 420.505	0.8	1.4	5.6	1.7	4.3	1.6	4.3	0.74
Fe II 238.204	0.7	0.54	3	2.3	1.4	2.1	2.7	0.78
Ga I 294.364	2.4	1.2	24	4.3	11	4.4	13	3.9
Ge I 265.117	5	1.3	25	7.2	11	7.1	7.7	5.8
Hg I 184.887	5.3	6	1.2	5.2	0.65	5.5	0.95	4.5
In II 230.606	5.8	2.2	22	10	22	27	35	13
K I 766.491	1.3	1.5	n/a	2.5	2.2	7.6	1.8	6.1
La II 408.672	0.78	0.78	5	2.9	4.7	2.2	3	1.3
Li I 670.783	1	0.35	1.2	3.6	0.75	1.7	0.37	1.7
Mg II 280.270	0.52	0.29	2.5	1.8	0.81	1.7	1.1	0.66
Mg I 285.213	0.57	0.73	3.5	1.6	2.3	1.3	1.2	0.84
Mn II 257.610	0.52	0.91	2.7	1.5	1.2	1.2	1.5	0.32
Mo II 202.032	0.79	0.8	4.5	1.6	2.3	1.9	2.8	2.4
Ni II 231.604	0.92	0.84	7.7	1.3	3.4	1.5	3.5	1.3
P I 177.434	2	4.4	11	5.4	18	1.6	6.3	2.3
Pb II 220.353	2	0.96	9.3	3.9	4.4	6.1	7.8	1.3
S I 180.669	3.7	3.7	16	15	12	3	21	20
Sb I 217.582	4.7	2.2	22	10	26	13	12	11
Se I 196.026	2.5	1.5	8.5	2.5	3.7	6.3	9.3	4.1
Si I 251.611	1.4	0.82	7.5	2.1	8.7	4.3	18	2
Sr II 421.552	1.3	0.65	2.3	1.4	2.2	1.1	1.9	0.56
Ti II 334.941	0.65	1.2	2	1.6	2.5	2	1.1	0.97
V II 292.464	0.57	1	4.4	1.2	4	1.8	2.7	0.97
Y II 371.029	0.56	0.47	2.9	1.6	1.2	1.1	1.7	0.54
Zn II 206.200	0.74	0.69	2.5	1.5	3.2	2.2	4.3	0.72
Zn I 213.857	0.64	0.69	2.6	3.4	2	1.6	1.9	0.61
Zr II 339.198	0.54	0.33	6.2	2.4	2	0.9	4.2	0.54

3.3.3 Plasma robustness

Plasma robustness is represented by Mg 280.270 nm/ Mg 285.213 nm ratios in Figures 3.11-3.13 (n = 5). Again, a Mg II/ Mg I ratio of 10 or greater is representative of a robust plasma, as defined by Mermet [26], where Mg is used for measures of robustness due to the high sensitivity of both lines to changes in experimental parameters, and the simplicity of using the energetically similar Mg 280.270 nm and 285.213 nm line in terms of the Saha equation. In all cases for Dual Mode, HG Mode, and Nebulisation Mode, the IR heated method provides improved plasma robustness when compared to the conventional MSIS method. Hence, pre-evaporation of the sample aerosol results in plasma excitation conditions that are closer to the LTE. Following from previous reports [18, 35, 37], the hydrogen by-product of HG provides a more robust plasma, as the MSIS setups have enhanced Mg II/Mg I ratios over other methods. For instance, the Agilent PN used in this work has a Mg ratio of 9.3 ± 0.1 in lateral mode, while Agilent MSIS conventional lateral view Mg ratios are 10.1 ± 0.1, and 9.9 ± 0.3 for Dual Mode and HG Mode, respectively. For Agilent MSIS(IR) lateral view, these ratios are 10.8 ± 0.1 for Dual Mode, and 10.5 ± 0.1 for HG Mode. These are comparable to previous work in which a USN-PET(IR) setup had a Mg ratio of 10.5 [2]. Furthermore, Chapter 2 Mg II/ Mg I ratios on the Agilent instrument are defeated by the MSIS(IR) setup, where lateral view ratios are 10.23 ± 0.03 for USN-HC, and 8.7 ± 0.3 for USN-PET(IR). The poor Mg II/ Mg I ratios for ARCOS MSIS(IR) is likely due to overloading of the plasma when heating to 175 °C. The previous PN-MSIS-PET on ARCOS had a Mg ratio of about 12, while MSIS(IR) Dual Mode on ARCOS has a Mg ratio of 6.4 ± 0.3. By heating with a rope heater (both IR and convective heating), instead of just heating tape (only convective heating), in addition to heating a larger portion of the torch (only 3cm of the torch are heated for PN-MSIS-PET, while 7cm are heated on ARCOS MSIS(IR)), too much sample may be pre-vapourized too quickly. However, in comparison to the conventional MSIS on ARCOS, MSIS(IR) still sees some improvements to robustness. The results in the following graphs also agree with

the repeatedly reported findings that axial view provides lower detection limits, while lateral view provides greater plasma robustness [5].

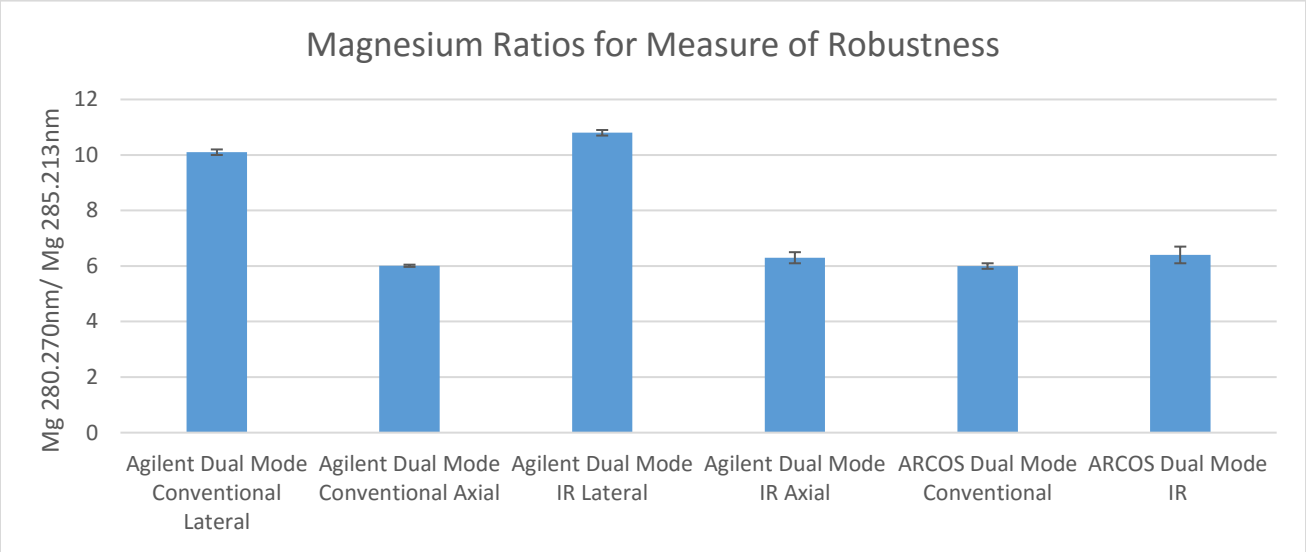

Figure 3.11: Magnesium ratios (Mg 280.270nm/ Mg 285.213) for measure of robustness for MSIS Dual Mode Setups

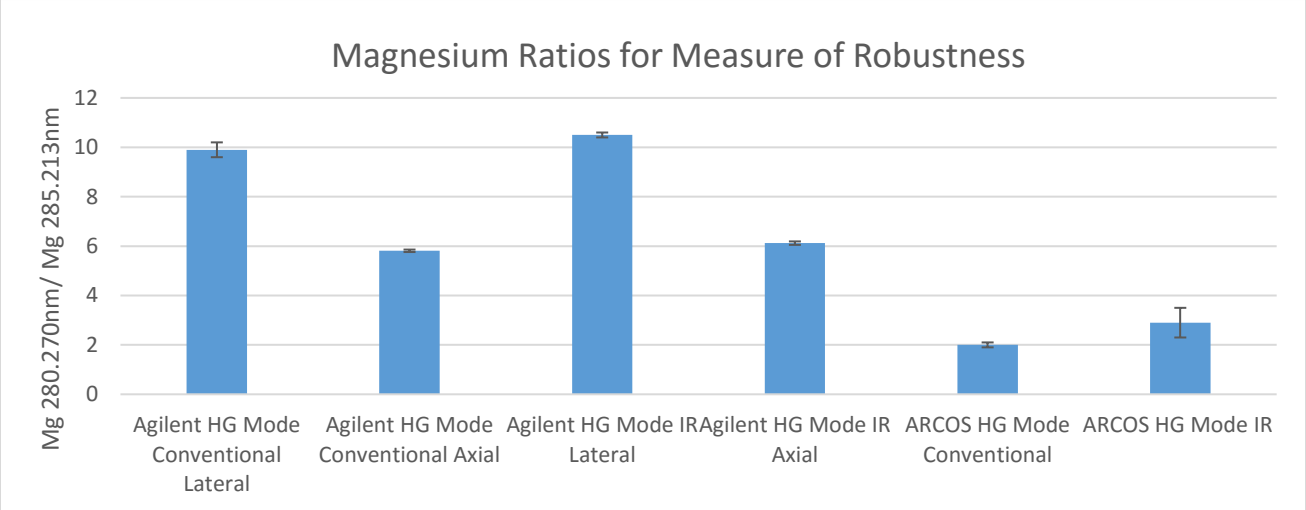

Figure 3.12: Magnesium ratios (Mg 280.270nm/ Mg 285.213) for measure of robustness for MSIS HG Mode Setups

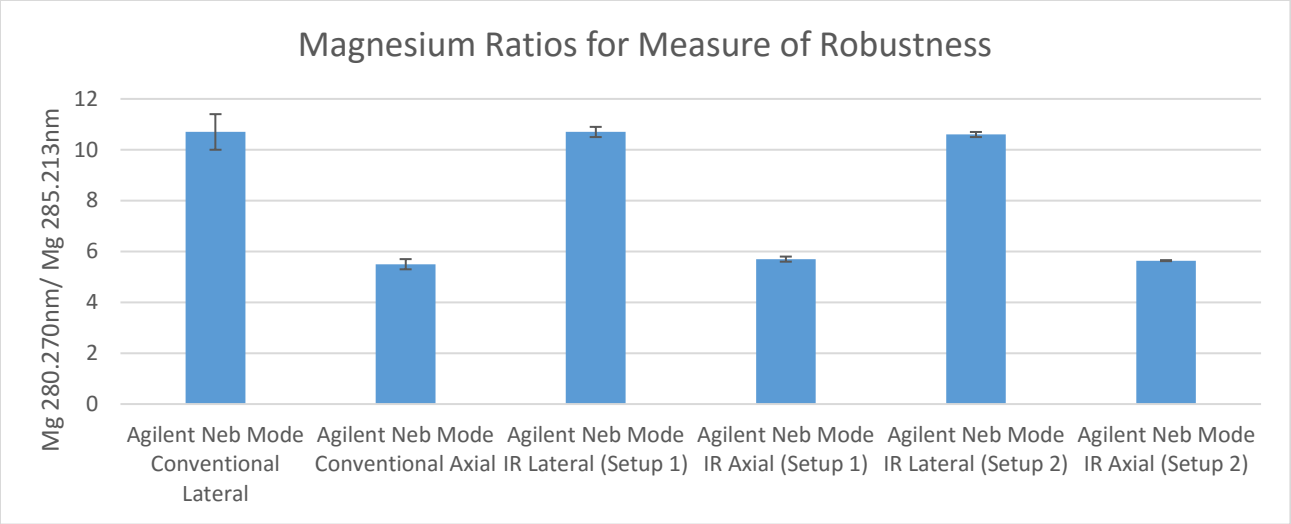

Figure 3.13: Magnesium ratios (Mg 280.270nm/ Mg 285.213) for measure of robustness for MSIS Nebulization Mode Setups

3.3.4 Analysis of food and water samples

In order to further investigate plasma robustness, waste water and food samples were analysed and verified by MSIS(IR) on the Agilent instrument (Tables 3.21-3.23). Due to the requirement of having final concentrations of 1.0M HNO_3 for HG, corn bran digests had to be diluted more than is typically done for food samples [38]. This resulted in many elemental analytes having extremely low concentrations that cannot be detected by ICP-OES, and the number of elements listed for the corn bran SRM 8433 is therefore reduced. An external calibration with matrix matching, but without internal standardisation, was conducted and values were compared to the certified reference values and the corresponding confidence limits at the 95% confidence level. No significant buildup of condensed material in the torch injector, PET, nor MSIS chamber was observed following a single experiment (i.e. one mode), and the setup could be left without dismantling and cleaning for several series of experiments. While previously [9] internal standardisation using an Ar emission line had been used without matrix matching, internal standardisation was found to not be beneficial in this work. Since 1.0 M HNO_3 and 1% m/m L-cysteine already had to be added for HG, the only additional step in the

procedure for matrix matching was the inclusion of 0.8% v/v H_2O_2 to standards and blanks for the measurement of the SRM 8433 samples.

Table 3.21: Concentrations ± standard deviation (n = 5) determined in certified reference materials by MSIS(IR) Agilent Dual Mode, where (a) = axial view and (l) = lateral view

	Waste Water, Low (EU-L-3) (mg/L)		Corn Bran SRM 8433 (mg/kg)	
Element	**MSIS(IR) M1**	**Certified ± Confidence Limit**	**MSIS(IR) M1**	**Certified ± Confidence Limit**
Al	6.47 ± 0.09 (a)	6.28 ± 0.19		
Cd	2.32 ± 0.02 (a) 2.24 ± 0.02 (l)	2.28 ± 0.05		
Cr	6.24 ± 0.06 (a) 6.21 ± 0.10 (l)	6.26 ± 0.15		
Cu	10.89 ± 0.09 (l)	10.6 ± 0.2	2.15 ± 0.27 (a)	2.47 ± 0.40
Fe	5.94 ± 0.08 (l)	5.80 ± 0.09	15.4 ± 1.8 (a) 13.5 ± 1.7 (l)	14.8 ± 1.8
K	219 ± 12 (a)	207 ± 5	485 ± 31 (a) 515 ± 43 (l)	566 ± 75
Mg	92.62 ± 0.66 (a) 91.29 ± 1.00 (l)	93.8 ± 2.3		
Mo	3.94 ± 0.07 (a) 4.00 ± 0.06 (l)	3.97 ± 0.08		
P			198 ± 20 (a)	171 ± 11
Pb	4.15 ± 0.22 (a) 4.26 ± 0.02 (l)	4.18 ± 0.06		
Sb	1.76 ± 0.04 (a) 1.88 ± 0.04 (l)	1.84 ± 0.07		
Se	2.70 ± 0.26 (a) 2.98 ± 0.32 (l)	2.79 ± 0.16		
Sr	13.98 ± 0.32 (a)	14.0 ± 0.4	4.77 ± 0.59 (a)	4.62 ± 0.56
Zn	3.06 ± 0.05 (a) 3.09 ± 0.03 (l)	3.05 ± 0.21	21.6 ± 1.3 (a)	18.6 ± 2.2

Table 3.22: Concentrations ± standard deviation (n = 5) determined in certified reference materials by MSIS(IR) Agilent HG Mode, where (a) = axial view and (l) = lateral view

	Waste Water, Low (EU-L-3) (mg/L)		Corn Bran SRM 8433 (mg/kg)	
Element	**MSIS(IR) M2**	**Certified ± Confidence Limit**	**MSIS(IR) M2**	**Certified ± Confidence Limit**
As	8.48 ± 0.33 (a) 8.39 ± 0.33 (l)	8.40 ± 0.12		
Al	6.70 ± 0.73 (a) 6.27 ± 0.48 (l)	6.28 ± 0.19		
Be	1.20 ± 0.04 (a) 1.24 ± 0.03 (l)	1.23 ± 0.02		
Co	8.93 ± 0.78 (a) 8.60 ± 0.89 (l)	8.25 ± 0.08		
Cr	6.63 ± 0.30 (l)	6.26 ± 0.15		
K			530 ± 110 (a) 669 ± 98 (l)	566 ± 75
Mg	91.86 ± 3.09 (a)	93.8 ± 2.3		
Mn	12.67 ± 0.68 (a) 12.35 ± 0.46 (l)	12.2 ± 0.2		
Mo	4.14 ± 0.35 (l)	3.97 ± 0.08		
Ni	8.34 ± 0.09 (a) 8.49 ± 0.24 (l)	8.34 ± 0.12		
Pb	3.49 ± 1.1 (a) 4.08 ± 0.58 (l)	4.18 ± 0.06		
S			740 ± 130 (l)	860 ± 150
Se	2.63 ± 0.18 (a)	2.79 ± 0.16		
Sr	13.66 ± 0.50 (a) 14.46 ± 0.51 (l)	14.0 ± 0.4		
Zn	3.06 ± 0.09 (a) 2.98 ± 0.10 (l)	3.05 ± 0.21	16.6 ± 8.4 (a) 18.1 ± 4.9 (l)	18.6 ± 2.2

Table 3.23: Concentrations ± standard deviation (n = 5) determined in certified reference materials by MSIS(IR) Agilent Nebulisation Mode (Setup 2) , where (a) = axial view and (l) = lateral view

	Waste Water, Low (EU-L-3) (mg/L)		Corn Bran SRM 8433 (mg/kg)	
Element	**MSIS(IR) M3**	**Certified ± Confidence Limit**	**MSIS(IR) M3**	**Certified ± Confidence Limit**
Al	6.03 ± 0.07 (a) 6.43 ± 0.11 (l)	6.28 ± 0.19	0.99 ± 0.15 (l)	1.01 ± 0.55
As	8.66 ± 0.19 (l)	8.40 ± 0.12		
Cd	2.20 ± 0.04 (a) 2.32 ± 0.04 (l)	2.28 ± 0.05		
Co	8.16 ± 0.23 (a) 8.19 ± 0.17 (l)	8.25 ± 0.08		
Cu	10.34 ± 0.16 (a) 10.77 ± 0.23 (l)	10.6 ± 0.2	2.72 ± 0.21 (a) 2.21 ± 0.21 (l)	2.47 ± 0.40
Cr	6.31 ± 0.11 (a) 6.20 ± 0.14 (l)	6.26 ± 0.15		
Fe	5.68 ± 0.07 (a) 5.72 ± 0.10 (l)	5.80 ± 0.09	14.43 ± 0.74 (a) 14.77 ± 0.39 (l)	14.8 ± 1.8
K			616 ± 15 (l)	566 ± 75
Mg	92.59 ± 2.07 (l)	93.8 ± 2.3	828 ± 43 (a) 865 ± 14 (l)	818 ± 59
Mn	12.45 ± 0.18 (a) 12.06 ± 0.16 (l)	12.2 ± 0.2	2.58 ± 0.10 (a) 2.64 ± 0.04 (l)	2.55 ± 0.29
Mo	3.89 ± 0.08 (a) 3.95 ± 0.06 (l)	3.97 ± 0.08	0.37 ± 0.11 (l)	0.252 ± 0.039
Na	517.3 ± 10.1 (l)	522 ± 9	430 ± 42 (a) 443 ± 18 (l)	430 ± 31
Ni	8.21 ± 0.15 (a) 8.47 ± 0.16 (l)	8.34 ± 0.12		
P	100.93 ± 1.62 (a) 102.1 ± 1.8 (l)	99.0 ± 1.5	168.2 ± 8.8 (a) 163.0 ± 2.6 (l)	171 ± 11
Pb	4.22 ± 0.07 (a) 4.16 ± 0.07 (l)	4.18 ± 0.06		
S			738.3 ± 31.3 (a) 753.5 ± 9.9 (l)	860 ± 150
Se	2.73 ± 0.11 (a) 2.86 ± 0.06 (l)	2.79 ± 0.16		
Sr	13.98 ± 0.37 (a) 14.20 ± 0.24 (l)	14.0 ± 0.4	4.55 ± 0.16 (a) 4.70 ± 0.06 (l)	4.62 ± 0.56
Zn	3.04 ± 0.05 (a) 3.03 ± 0.05 (l)	3.05 ± 0.21	18.52 ± 0.55 (a) 18.49 ± 0.42 (l)	18.6 ± 2.2

3.4 Conclusion

Addition of an IR-heated PET to an MSIS setup is found to increase plasma robustness, sensitivity, and detection limits in all three operating modes (dual mode, hydride generation mode, and nebulisation mode). Improvements are especially seen when HG is employed, as indicated by the greater factors of improvement for Dual Mode and HG Mode over Nebulisation Mode. Of particular interest are the improvements found for Be when MSIS(IR) is compared to conventional MSIS, indicating that beryllium hydride could be produced with the addition of heat. Overall improvements in analytical capabilities throughout this work must be correlated to HG enhancing sensitivity in hydride-forming elements (i.e. when compared to PN), the hydrogen by-product of MSIS HG improving plasma excitation efficiency, and the pre-evaporation of the aerosol resulting in preserved water vapour for improved plasma excitation characteristics and reduced sample droplet size. Although ARCOS experiments indicated slightly lower detection limits, the experiments on the Agilent instrument proved to be much more robust and therefore were investigated in more depth. It is likely that a change in the Agilent torch model would benefit future work with pre-evaporation. The plastic casing around the torch could be hollowed out to make a tunnel around the injector, and the casing could be made out of a more heat-resistant material (i.e. Teflon). In doing so, a full 7 cm of the torch injector could be heated, rather than just the current 3 cm, and deformation of the gas inlets could be prevented. The tunnel could also be lined with aluminum foil to further reduce the probability of melting. By heating a greater area, cooling and condensation of the pre-vaporized aerosol would be prevented, resulting in greater improvements in sensitivity. In other words, the benefits of using the ARCOS setup could be revamped on the Agilent setup

3.5 References

[1] J. D. Winefordner, I. B. Gornushkin, T. Correll, E. Gibb, B. W. Smith and N. Omenetto, J. Anal. At. Spectrom, Comparing several atomic spectrometric methods to the super stars: special emphasis on laser induced breakdown spectrometry, LIBS, a future super star, (2004), 19, 1061–1083.

[2] A. Asfaw, W. MacFarlane and D. Beauchemin, Ultrasonic nebulization with infrared heated preevaporation tube for sample introduction in ICP-OES: application to geological and environmental samples, J. Anal. At. Spectrom., 27 (2012) 1254-1263.

[3] J. Mora, S. Maestre, V. Hernandis and J. L. Todoli, Liquid-sample introduction in plasma spectrometry, TrAC Trends Anal. Chem., (2003), 22, 123–132.

[4] R.I.J. McLaughlin, I.D. Brindle, Multimode Sample Introduction System, U.S Patent number 6,891,605; May 10, 2005

[5] C. B. Boss and K. J. Fredeen, Concepts, Instrumentation, and Techniques in Inductively Coupled Plasma Optical Emission Spectrometry, 2nd Edition, The Perkin-Elmer Corporation, 1997.

[6] R. McLaughlin, P. Cheese, M. Ding, A. Ptolemy, A. Conn, D. Brindle, (2006) Am. Lab., 13–17 41.

[7] P. Pohl, Hydride generation – recent advances in atomic emission spectrometry, TrAC, Trends Anal. Chem., (2004), 23, 87–101.

[8] R. E. Sturgeon and Z. Mester, Analytical applications of volatile metal derivatives, Appl. Spectrosc., (2002), 56, 202A–213A.

[9] A. Asfaw and D. Beauchemin, Combination of a multimode sample introduction system with a preevaporation tube to improve multi-element analysis by ICP-OES, J. Anal. At. Spectrom. 27 (2012) 80-91.

[10] M. Grotti, C. Lagomarsino and R. Frache, Multivariate study in chemical vapor generation for simultaneous determination of arsenic, antimony, bismuth, germanium, tin, selenium, tellurium and mercury by inductively coupled plasma optical emission spectrometry, J. Anal. At. Spectrom., (2005), 20, 1365–1373.

[11] G. Centineo, M. M. Bayon and A. Sanz-Medel, Flow injection analysis with inductively coupled plasma time-of-flight mass spectrometry for the simultaneous determination of elements forming hydrides and its application to urine, J. Anal. At. Spectrom., (2000), 15, 1357–1362.

[12] I. Brindle, Vapour-generation analytical chemistry: from Marsh to multimode sample-introduction system, Anal Bioanal Chem (2007) 388:735–741

[13] A. Asfaw and G. Wibetoe, A new demountable hydrofluoric acid resistant triple mode sample introduction system for ICP-AES and ICP-MS, J. Anal. At. Spectrom., (2007), 22, 158–163.

[14] M. Mulugeta, G. Wibetoe, C. J. Engelsen and A. Asfaw, Multivariate optimization and simultaneous determination of hydride and non-hydride-forming elements in samples of a wide pH range using dual-mode sample introduction with plasma techniques: application on leachates from cement mortar material, Anal. Bioanal. Chem., (2009), 393, 1015–1024.

[15] A. Asfaw and G. Wibetoe, Dual mode sample introduction for multi-element determination by ICP-MS: the optimization and use of a method based on simultaneous introduction of vapor formed by NaBH4 reaction and aerosol from the nebulizer, J. Anal. At. Spectrom., (2006), 21, 1027– 1035.

[16] R. L. J. McLaughlin and I. D. Brindle, A new sample introduction system for atomic spectrometry combining vapour generation and nebulization capacities, J. Anal. At. Spectrom., (2002), 17, 1540–1548.

[17] L. R. Gomez, G. D. Marquez and J. R. Chirinos, Dual nebulizer sample introduction system for simultaneous determination of volatile elemental hydrides and other elements, Anal. Bioanal. Chem., (2006), 386, 188–195.

[18] H. Wiltsche, I. B. Brenner, K. Prattes and G. Knapp, Characterization of a multimode sample introduction system (MSIS) for multielement analysis of trace elements in high alloy steels and nickel alloys using axially viewed hydride generation ICP-AES, J. Anal. At. Spectrom., (2008), 23, 1253-1262.

[19] G. Peters and D. Beauchemin, Effect of Pre-evaporating the Solvent on the Analytical Performance of Inductively Coupled Plasma Mass Spectrometry, Spectrochim. Acta, Vol. 48B. No 12, (1993) 1481-1494.

[20] A. Asfaw and D. Beauchemin, Improvement of the capabilities of inductively coupled plasma optical emission spectrometry by replacing the desolvation system of an ultrasonic nebulization system with a pre-evaporation tube. Spectrochim. Acta B, 65, (2010), 376 – 384.

[21] T. Prohaska, S. Hann, C. Latkoczy and G. Stingeder, Determination of rare earth elements U and Th in environmental samples by inductively coupled plasma double focusing sectorfield mass spectrometry (ICP-SMS), J. Anal. At. Spectrom., (1999), 14, 1–8.

[22] A. Belhamra, R. Diabi and A. Moussaoui, Technology and applications of infrared heating in the industrial area, J. Eng. Appl. Sci., (2007), 2, 1183–1187.

[23] K. Krishnamurthy, H. K. Khurana, S. Jun, J. Irudayaraj and A. Demirci, Infrared heating in food processing: an overview, Compr. Rev. Food Sci. Food Saf., (2008), 7, 2–13.

[24] A. Risnes and W. Lund, Comparison of systems for eliminating interferences in the determination of arsenic and antimony by hydride generation inductively coupled plasma atomic emission spectrometry, J. Anal. At. Spectrom., (1996), 11, 943-948.

[25] S. Liu and D. Beauchemin, The effect of pre-evaporation on ion distributions in inductively coupled plasma mass spectrometry. Spectrochim. Acta B, 61, (2006), 157 – 163.

[26] J. M. Mermet, Use of magnesium as a test element for inductively coupled plasma atomic emission spectrometry diagnostics. Anal. Chim. Acta, 250, (1991), 85 – 94.

[27] X. Romero, E. Poussel and J. M. Mermet, Influence of the operating conditions on the efficiency of internal standardization in inductively coupled plasma atomic emission spectrometry. Spectrochim. Acta B, 52, (1997), 487 – 493.

[28] I. Novotny, J. C. Farinas, J. L. Wan, E. Poussel and J. M. Mermet, Effect of power and carrier gas flow rate on the tolerance to water loading in inductively coupled plasma atomic emission spectrometry. Spectrochim. Acta B, 51, (1996), 1517 – 1526.

[29] M.T. Cicerone, P.B. Farnsworth, A simple, non-invasive method for the measurement of gas flow velocities in the inductively coupled plasma, Spectrochimica Acta. Vol. 44B, No. 9, (1989), 897-907.

[30] I. B. Brenner, A. T. Zander, Axially and radially viewed inductively coupled plasmas – a critical review, Spectrochim. Acta B, (2000), 55, 1195 - 1240.

[31] Y. Ralchenko, A. Kramida, J. Reader, NIST Atomic Spectra Database (ver. 5.1), http://physics.nist.gov/asd.

[32] P. Bernath, A. Shayesteh, K. Tereszchuk, R. Colin, The vibration-rotation emission spectrum of free BeH_2, Science, 297, (2002), 1323-1324.

[33] T.J. Tague Jr., L. Andrews, Reactions of beryllium atoms with hydrogen. Matrix infrared spectra of novel product molecules, J. Am. Chem. Soc., 115, (1993), 12111-12116.

[34] R. Mori, N. Fukata, M. Suezawa, A. Kasuya, Optical absorption spectra of Be–H and Zn–H complexes in Si, Physica B, 206, (2001), 302-303.

[35] P. Pohl and J.A.C. Broekaert, Spectroscopic and analytical characteristics of an inductively coupled argon plasma combined with hydride generation with or without simultaneous introduction of the sample aerosol for optical emission spectrometry, Anal. Bioanal. Chem., (2010), 398, 537-545.

[36] P. Pohl and R.E. Sturgeon, Simultaneous determination of hydride- and non-hydride-forming elements by inductively coupled plasma optical emission spectrometry, TrAC, Trends Anal. Chem., (2010), 29, 1376-1389.

[37] K. A. Wolnik, F. L. Fricke, M. H. Hahn and J. A. Caruso, Sample introduction system for simultaneous determination of volatile elemental hydrides and other elements in foods by inductively coupled argon plasma emission spectrometry, Anal. Chem., (1981), 53, 1030-1035.

[38] N. Sadiq and D. Beauchemin, Optimization of the operating conditions of solid sampling electrothermal vaporization coupled to inductively coupled plasma optical emission spectrometry for the sensitive direct analysis of powdered rice, Analytica Chimica Acta, (2014), 851, 23-29.

Chapter 4: Development of Methods for the Characterization of a 12 M KOH Zincate Fuel for Green Energy Backup Systems

4.1 Introduction

ZincNyx Energy Solutions manufactures battery backup systems, which support solar and wind energy generation systems to ensure continuous operation without a drop in energy levels. In order to advance and monitor the performance of these backup systems, ZincNyx requires a method for the overall analysis of their 12 M KOH zincate electrolyte fuel. Rather than shipping samples for analysis, the company is looking to purchase an instrument for in-house analysis with a set and conclusive method, saving both time and money for long-term operation. With the goals of verifying KOH concentration, and measuring the fuel's content of additives (i.e. Al, In, Fe, Si, and Mg), corrosions products (such as Zn^{2+} and CO_3^{2-} in solution), dislodged catalyst/carbon particles, and ZnO particles, a method was prepared on an Agilent 5100 ICP-OES for the elemental analysis of Al, Fe, C, In, Mg, Si, Zn and K in the 12 M KOH fuel.

Very little research has been published on the issue at hand. While early groundwork with ICP-OES employed the neutralization of KOH prior to analysis [1] in order to prevent the attack of a high pH solution on the nebuliser, spray chamber, and torch, this in turn dilutes the sample, resulting in diminished detection capabilities. Furthermore, lengthy sample preparation requiring the use of a strong acid such as HCl is not ideal. Other more recent work includes an off-line CO_2 vapour generation for the determination of carbonate in KOH by ICP-OES [2], and the determination of Si, Ni, Fe, Na, Al, and Ca in KOH by ICP-OES [3]. However, in the case of the latter, many important details are missing from the paper. Similarly, details concerning the analytical procedure and all ICP-OES instrumental conditions are entirely left out in publications [4, 5, 6] in which the leaching of elements into alkaline solution was monitored. The trace analysis of metals in a 11.25% KOH solution was achieved with ICP-MS; however, this required an on-line electrodialyzer to remove K^+ and OH^- from the trace analytes, so as to prevent

the KOH from expending matrix effects and damaging the sample introduction system. Additionally, in order to enable the trace metal separation from K^+, analytes had to be transformed into anionic chelates through complexation with ethylene diamine tetraacetic acid [7].

Conversely, the present work does not require such a complex procedure in terms of sample preparation and analysis. Using an inert setup with two varieties of plastic nebulisers, a Teflon spray chamber, and a torch with a ceramic injector, the 12 M (45 m/m) KOH fuel solution could be directly analyzed, without fear of degrading the sample introduction system. Several methods were attempted in both axial and lateral views, including direct undiluted analysis of the fuel with flow injection, diluting the fuel with DDW for analysis without flow injection, and adding ZnO and KNO_3 to series of undiluted and diluted fuel samples for standard additions. From these trials, an optimal procedure for the overall analysis of the fuel (including both the solution and the ZnO particles) was constructed. In addition to forming this procedure, experiments were conducted to confirm the validity of using the provided 12 M KOH as a blank, and to investigate the effects of exposing the fuel to air. Consequently, the current work provides ZincNyx with an overview of the changes to their fuel's composition over time, as well as a ready-made method for their in-house analysis.

4.2 Experimental

4.2.1 Instrumentation

Method development and application was performed on an Agilent 5100 ICP-OES (dual view, Agilent Technologies, Santa Clara, California, United States). The instrument was equipped with an inert Teflon spray chamber, a prototype V-groove nebuliser, and an inert torch with ceramic injector (all from Agilent Technologies, Santa Clara, California, United States). The V-groove nebuliser was later replaced with a OneNeb nebuliser (Agilent Technologies, Santa Clara, California, United States) for comparison of nebuliser efficiency. For direct analysis of the 12 M KOH fuel, a flow injection device was coupled to the

sample introduction system. The experimental setup with and without FI is shown in Fig. 4.1 and the two nebulisers are shown in Fig. 4.2. The optimal operating conditions when using the two different nebulisers are provided in Tables 4.1 and 4.2.

Table 4.1: Optimal conditions with prototype (V-groove) nebuliser

Viewing Mode	**Axial**	**Lateral**
RF Power (kW)	1.5	1.5
Plasma gas flow (L/min)	12	12
Nebulizer gas flow (L/min)	0.6	0.8
Auxiliary gas flow (L/min)	0.5	0.5
Sample Uptake Rate (mL/min)	2.0	2.0
Plasma Observation Height (mm)	N/A	5

Table 4.2: Optimal conditions with OneNeb nebuliser

Viewing Mode	**Axial**	**Lateral**
RF Power (kW)	1.5	1.5
Plasma gas flow (L/min)	15	12
Nebulizer gas flow (L/min)	0.6	0.6
Auxiliary gas flow (L/min)	0.5	0.5
Sample Uptake Rate (mL/min)	2.0	2.0
Plasma Observation Height (mm)	N/A	4

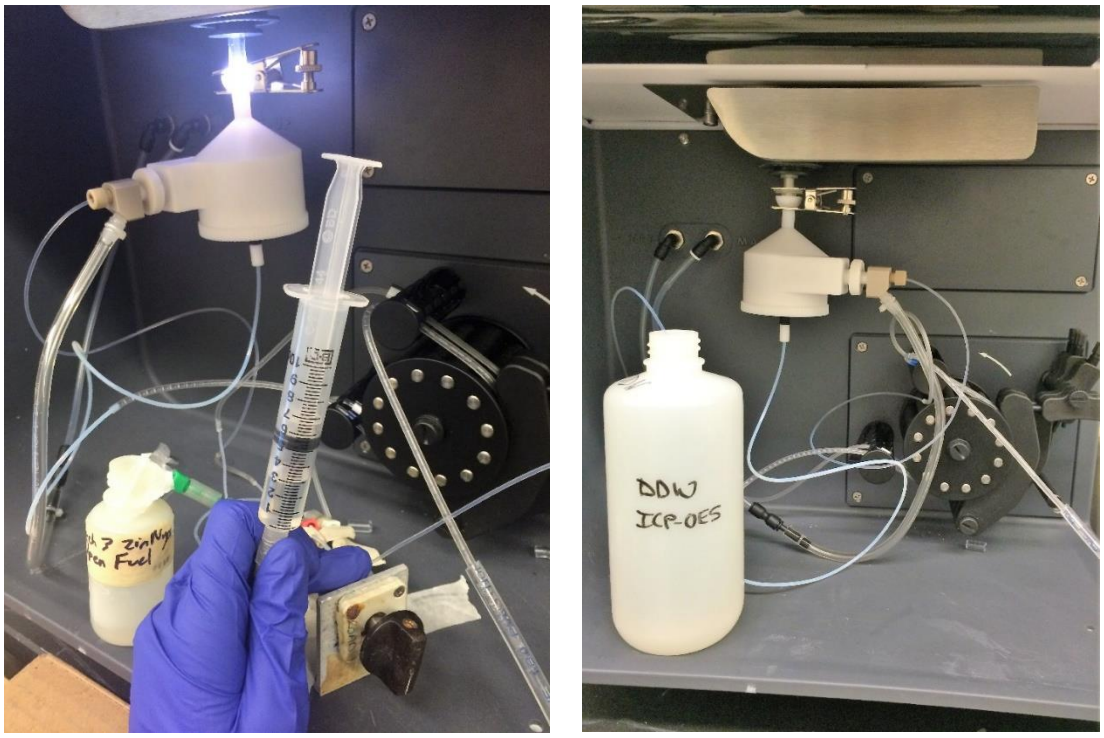

Figure 4.1: Sample introduction system consisting of a prototype V-groove nebuliser and an inert Teflon spray chamber; at left with a flow-injection switching valve, and at right without FI for dilution methods.

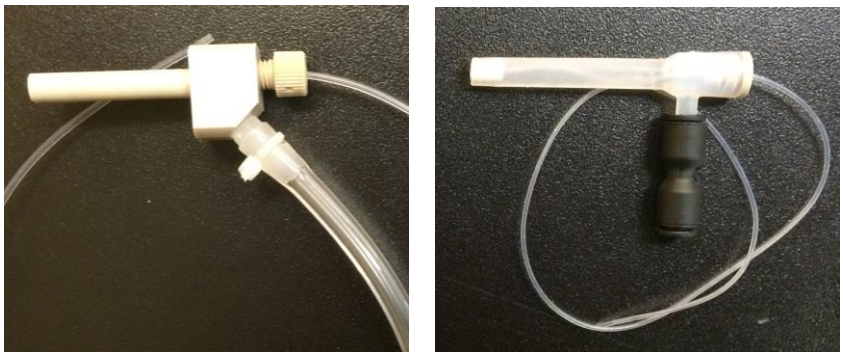

Figure 4.2: Prototype V-groove nebuliser (left) and OneNeb nebuliser (right), both from Agilent Technologies

4.2.2 Flow Injection

Flow injection analysis was used throughout this work to prevent attack by the undiluted 12 M KOH on the quartz torch. 100-µL aliquots of fuel (or pure 12 M KOH) were injected using an electronically actuated valve (Universal module, Anachem Ltd., Luton, England) equipped with a 100- µL

injection loop and rapidly washed away by the DDW carrier, thereby minimizing the degradation the base could have on the sample introduction system. With the benefits of low sample consumption, continuous washout and rapid analysis time [8], flow injection analysis was an ideal accessory for analysis of the 12 M KOH samples and standards, providing reproducible injection peaks in both lateral and axial view (Fig. 4.3 and 4.4).

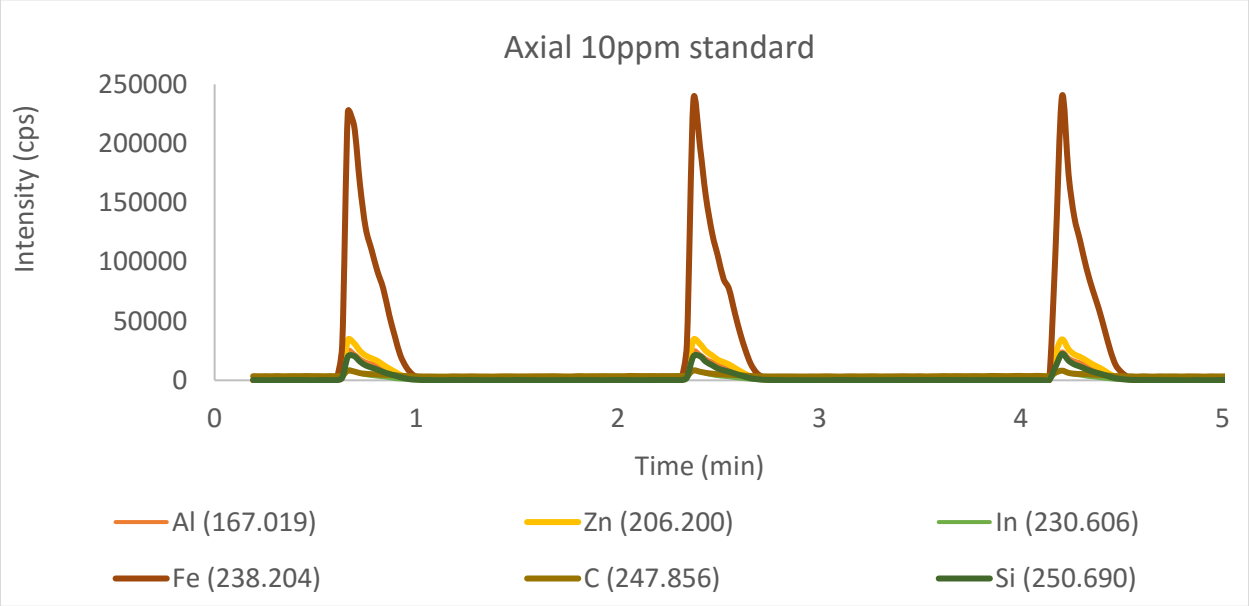

Figure 4.3: Axial view flow injection profiles of a 10 ppm multi-element standard in 12 M KOH. Emission lines are in nm.

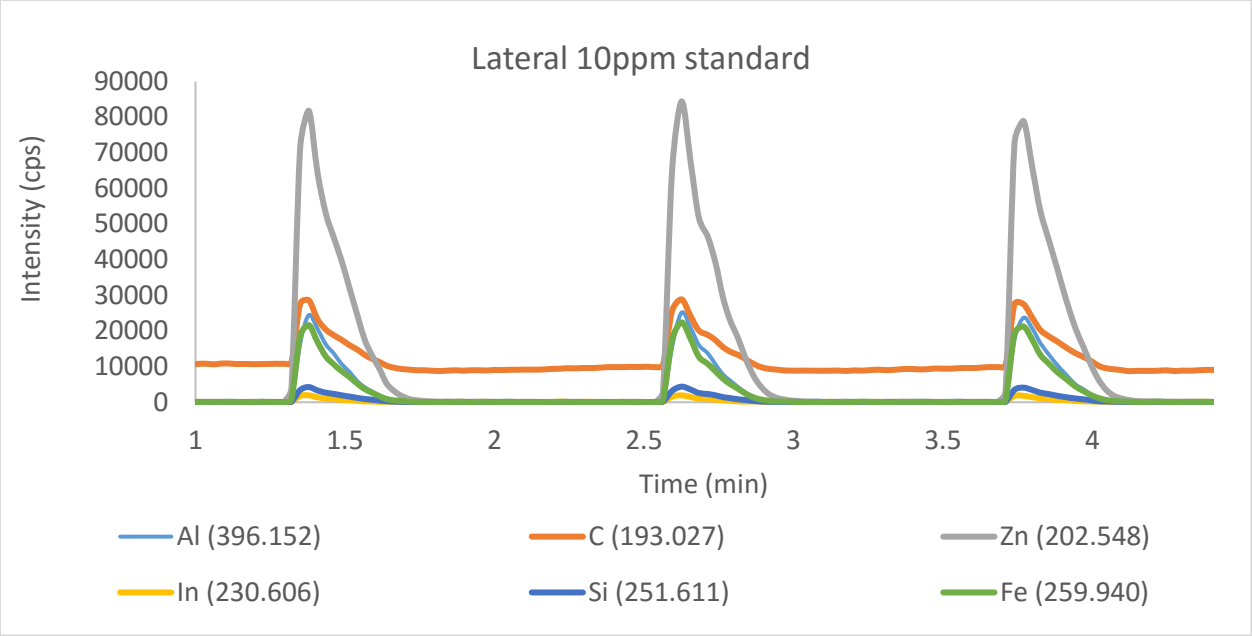

Figure 4.4: Lateral view flow injection profiles of a 10 ppm multi-element standard in 12 M KOH. Emission Lines are in nm.

Flow injection works by injecting a liquid sample into a continuously flowing carrier, which pushes the plug of sample through the sample line as carrier is pumped into the sample introduction system [9]. The goal in this work is to keep the sample and carrier un-mixed, creating clearly defined analyte peaks. A sample injection is conducted by first loading sample into the 100 µL sample loop (Fig. 4.5). While carrier DDW flows directly from the peristaltic pump to the nebuliser, sample is simultaneously suctioned up from the sample bottle, through the sample loop, and into the syringe. While typically sample would be injected from the syringe, the reverse approach is used to prevent the rubber end of the syringe from being in contact with the 12 M KOH (i.e. in Figure 4.1 a headspace is left between the rubber stopper and the fuel sample). Once the sample loop is full, the FI is switched to inject mode, whereby the carrier flows through the loop and pushes the sample plug through to the nebuliser (Fig. 4.6).

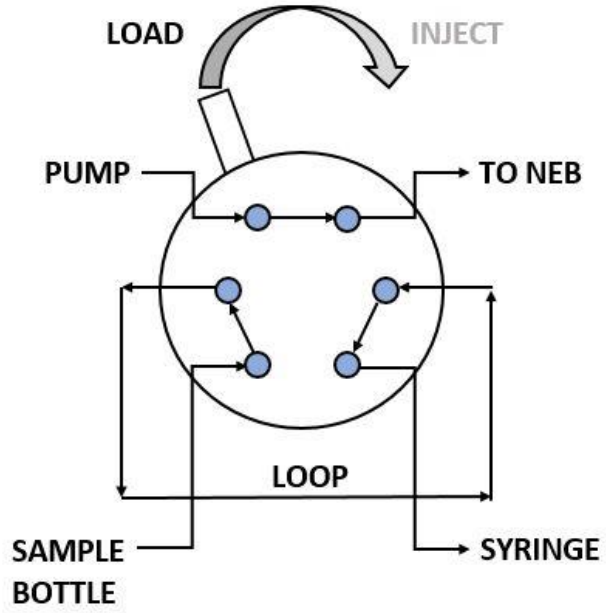

Figure 4.5: Flow injection/ switching valve system in the load position

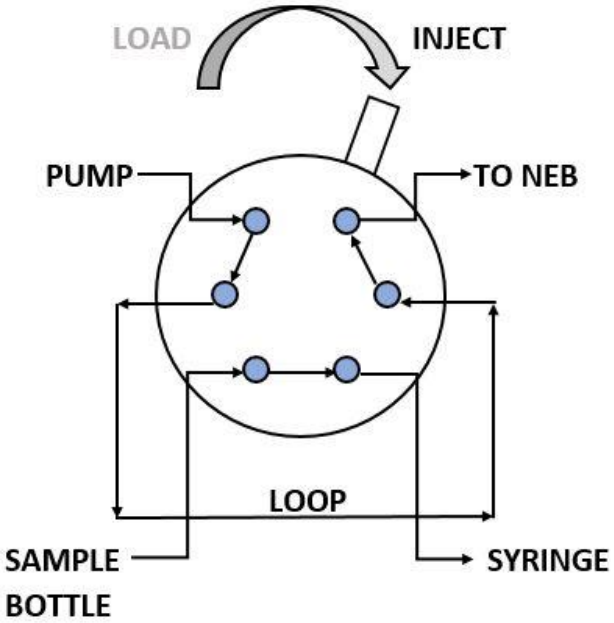

Figure 4.6: Flow injection/ switching valve system in the inject position

4.2.3 Reagents

All samples and standard solutions were prepared with 18 Ω cm^{-1} double deionized water (DDW) (Pro UV/DI, Sartorius Stedim Biotech, Gottingen, Germany) and HNO_3 (ACS grade; Fisher Scientific, Ottawa, Canada) that was purified prior to use with a DST-1000 Teflon sub-boiling distillation system (Savillex, Minnetonka, USA). 1000 and 10 000 mg L^{-1} mono-elemental plasma standard solutions (SCP Science, Baie d'Urfe, Quebec, Canada) (Al, Fe, In, Mg, Zn, K, Si) were diluted with DDW and HNO_3 to make a multi-elemental 100 mg L^{-1} stock solution of 4% HNO_3. From this stock, 10 mg L^{-1} stock solutions were made through further dilutions with DDW. Additionally, a 10 mg L^{-1} carbon stock was prepared by dissolving ≥97% grade L-cysteine (Sigma-Aldrich, Steinhein, Germany) in DDW. More dilute multi-element solutions were made from the 10 mg L^{-1} stocks and used as calibration standards. For diluted method experiments, these calibration standards were prepared in DDW, while the standards were prepared in 45 wt% (12 M) KOH (ZincNyx Energy Solutions, Vancouver, BC, Canada) for undiluted/flow injection experiments.

The potassium zincate electrolyte fuel ($Zn(OH)_4^{2-}$ in 45 wt% KOH with additives) (ZincNyx Energy Solutions, Vancouver, BC, Canada) was prepared for analysis by filtering the fuel through ashless Whatman 40 filter paper (Fisher Scientific, Ottawa, Ontario, Canada) to remove the ZnO particles. These portions of particles were thoroughly washed with DDW, and air-dried prior to being transferred into glass vials. For diluted method experiments, the filtered fuel (or 12 M KOH in the case of pure KOH experiments) was diluted 10 and 100-fold with DDW. For particle analysis, approximately 0.2 g of air-dried particles were weighed and added to 5 mL of DDW. The particles were then dissolved with the addition of 4 mL HNO_3 and brought to final concentrations of approximately 10 % v/v HNO_3.

Standard additions experiments for zinc and potassium determinations involved the additions of ZnO (99.9% Aldrich Chemical Company, Milwaukee, Wisconsin, USA) and KNO_3 (Certified A.C.S., Fair

Lawn, New Jersey, USA, Fisher Scientific) to undiluted and diluted samples of fuel, in which the highest concentration standards had concentrations of Zn or K matching that expected to be in the fuel. The four other standards were made to have equally spaced concentrations, with a 0 g addition being the lowest added.

4.2.4 Exposure tests and precipitate preparation

To investigate the effects of leaving the potassium zincate electrolyte fuel exposed to air, freshly filtered fuel was transferred into 60-mL plastic bottles and a 40-mL beaker. One bottle was closed off with the lid while the other bottle was left open, and all samples were left in a fume hood for the set interval of time (i.e. 12 hours, 24 hours, 96 hours, and 10 days). For initial analysis of exposed fuel, these samples were analyzed directly (without shaking the sample prior to analysis). In this case, the sample line was directed to avoid pumping up any precipitate that collected on the top of the fuel sample and along the edges of the sample container. In subsequent analysis of both the fuel and the precipitate, a filtered sample of fresh fuel was weighed and left in a beaker for 96 hours. The formed precipitate was then decanted off of the fuel, weighed, dissolved in 1 mL HNO_3, and diluted with DDW to a final nitric acid concentration of approximately 6 % v/v. The leftover fuel was also weighed in order to conduct mass balance calculations.

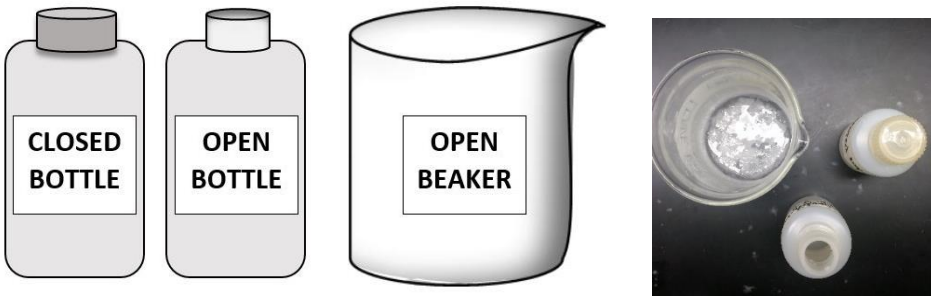

Figure 4.7: Schematic of closed and open 60-mL plastic bottles and a 40-mL glass beaker for exposure analysis (left). At right, a bird's-eye view showing potassium carbonate precipitate forming in the exposed fuel.

4.2.5 Optimization of experimental parameters

A 1 mg L^{-1} multi-elemental solution was used for multivariate optimizations, with the objective of finding the local thermodynamic equilibrium (LTE). Here, there is efficient energy transfer between the bulk and central channel of the plasma, resulting in high sensitivities and robustness. By monitoring the Mg II 280.270 nm/ Mg I 285.213 nm ratio, operating parameters that provided the most robust conditions were chosen, where a ratio of 10 or above indicated a robust plasma. At this level of robustness, changes in matrix composition and solvent loading do not significantly affect plasma excitation. Therefore, improved sensitivity and detection limit of analytes can be established. Various ionic and atomic lines of Al, C, Fe, In, K, Mg, Si, and Zn were also surveyed for changes in emission intensity. A face-centered central composite design was used for optimisation of RF power, plasma gas flow rate, nebulizer gas flow rate, auxiliary gas flow rate, and sample uptake rate. Separate optimization experiments were conducted in axial and lateral view for both the prototype V-groove nebuliser, and the OneNeb nebuliser. Following these multivariate optimisations, plasma observation height was optimized in transient mode by tracking intensity signals for all elemental analytes while slowly decreasing the height setting to take signal readings from deeper in the plasma.

4.2.6 Data analysis

Minitab 17 Software was used in constructing and analyzing experimental designs for multivariate optimizations. A large variety of atomic and ionic emission lines free from possible spectroscopic interference were selected for all 8 elemental analytes. The signals were corrected using a fitted background correction with 3 pixels read per analyte line (ICP Expert Software, Agilent Technologies, Santa Clara, California, United States). All subsequent experiments were processed in Microsoft Excel 2013. The signal intensity of the matrix-matched blank was subtracted from that of its

corresponding standard or sample to give the net signal intensity for the specified standard or sample. Detection limits for all analytes were calculated as 3 times the standard deviation of the average signal intensity of at least 10 consecutive blanks divided by the slope of the calibration curve (i.e. the sensitivity). Experiments involving highly diluted fuel (i.e. 10 or 100-fold dilution in DDW), or those involving analysis of a sample diluted in DDW, such as dissolved precipitate or particles, were conducted in analysis mode on the ICP Expert Software. Each signal was peak picked following the experiment in order to take readings defined by the centre of the intensity peak. All experiments involving undiluted fuel, fuel diluted in pure KOH, or fuel diluted 4-fold in DDW were operated in transient mode on the ICP Expert Software. In this mode all flow injection peaks from samples, standards, and blanks were defined on Excel according to individual time intervals, and averages of the areas under each peak were taken. All measured values were compared to concentrations provided to ZincNyx by a service laboratory. These concentrations, referred throughout this chapter as "ZincNyx values", are therefore not certified, but rather provided a reference which ZincNyx sought after for the newly-developed methods. It should be further noted that these "reference" values were reported to ZincNyx without error.

4.3 Results and discussion

4.3.1 Selection of optimum parameters

Sample introduction systems using either the prototype V-groove nebuliser or the OneNeb nebuliser with an inert Teflon spray chamber and inert torch with ceramic injector were optimized according to contour plots generated with Minitab 17 software (Fig. 4.8-4.11), where dark green indicates the highest range of values and dark blue indicates the lowest range of values. While three emission lines per element were analyzed for all 8 elements, only the In 230.606 nm emission signal and Mg 280.270 nm/ 285.213 nm ratio are shown as examples. The Mg II/ Mg I ratio was used as an indicator of robustness [10], where a set of experimental parameters generating ratio of at least 10

constitute a robust plasma setting. The Mg 280.270 nm and Mg 285.213 nm lines are most widely chosen for this purpose because of their close excitation energies (35 051 cm^{-1} and 35 669 cm^{-1}, respectively). The optimization of this ratio was of particular importance in this work due to the complex matrix of the fuel sample. In cases where a robust plasma is not achieved, large matrix effects can be expected [11]. Fig. 4.8-4.11 demonstrate that while Mg ratios above 9 can be achieved for lateral view with both nebulizers, axial view indicates ratio results above approximately 6 or 7 for the OneNeb and V-groove, respectively. This falls in accordance with the principle that axial view generally provides greater sensitivities, while lateral view is more robust [12].

In order to achieve a greater robustness, 1.5 kW was chosen as the RF power setting for all sets of optimum conditions. As highlighted by Mermet [10], a robust plasma is achieved when the RF power is at least 1.4 kW, and generally, a greater RF power increases robustness [13]. The below contour plots indicate similarities to Novotny [14], in which a low flow (0.6 L min^{-1}) carrier gas flow rate coupled with a high RF power provided the highest values of Mg ratio and Fe excitation temperature, and to work by Grotti [15, 16] and Brenner [11] in which Pb and Mg ratios showed an increase with increased carrier gas flow rate up to a certain maximum, and then decreased. This suggests that a minimum amount of solvent must reach the ICP for providing improvements to thermal conductivity; however, past this point, the residence time of the sample is too greatly reduced by the high speed gas. Sample uptake rates of 2 mL min^{-1} were consistently found to provide the greatest sensitivities and Mg ratio, which was also advantageous later for moving aliquots of the strongly basic fuel through the system at a faster rate. The given experimental parameters were optimized with the plasma observation height set to 8 mm; however, this height was later optimized in lateral view by observing the change of line intensity signals in transient mode as the signal was read from deeper into the plasma. This sequence of optimizations was chosen since changes to plasma observation height settings have a greater impact on plasma height (and therefore on analyte sensitivities) than auxiliary gas flow rate does.

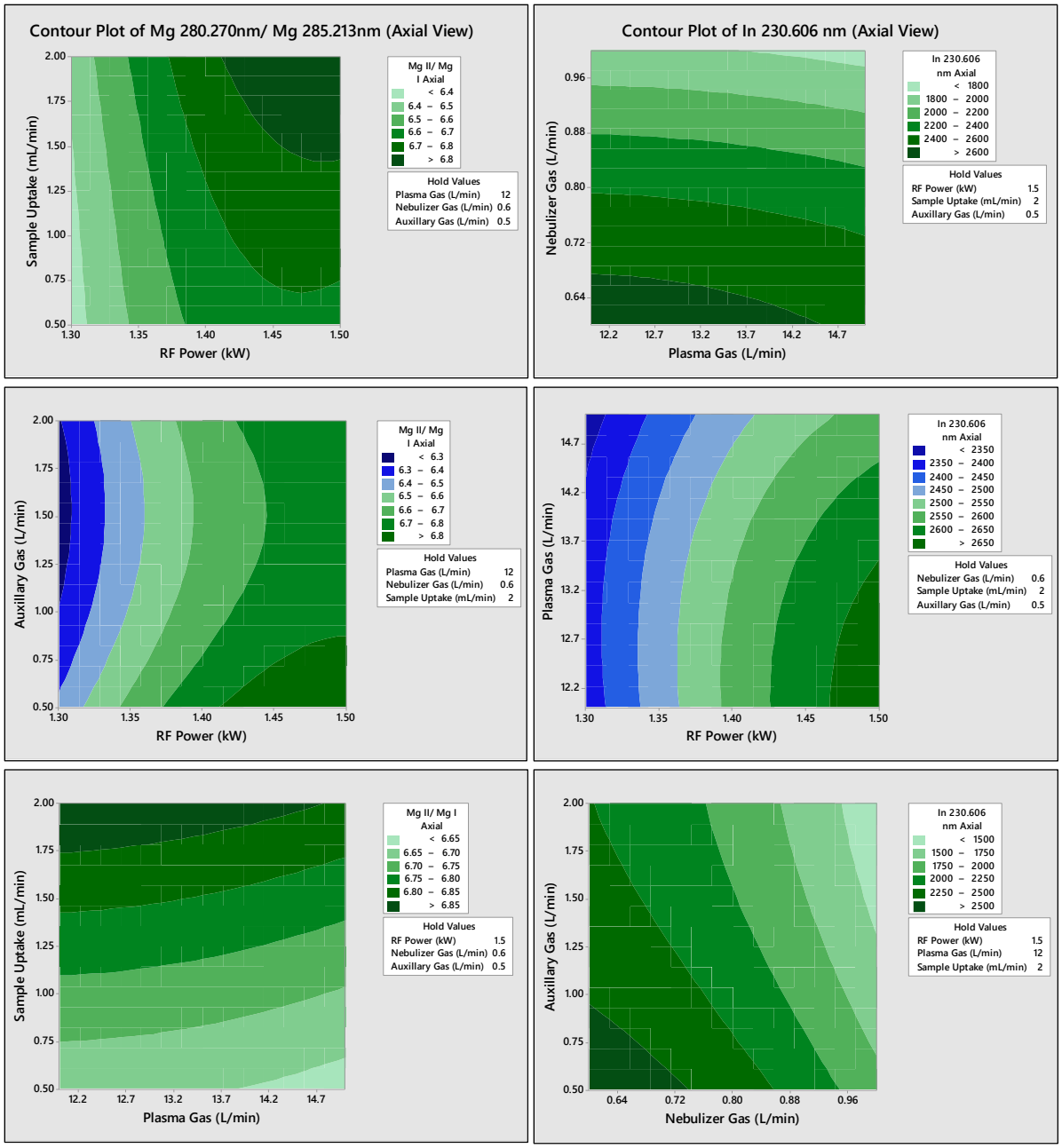

Figure 4.8: Contour plots for the multivariate optimization of the inert plastic setup with prototype (V-groove) nebuliser in axial viewing mode. Values are held in order to find the optimal compromised conditions for two other parameters. At left, Mg 280.270 nm and 285.213 nm emission intensities have been blank-subtracted, with the ratio providing an indication of robustness. At right, blank-subtracted In 230.606 nm emission intensities are shown.

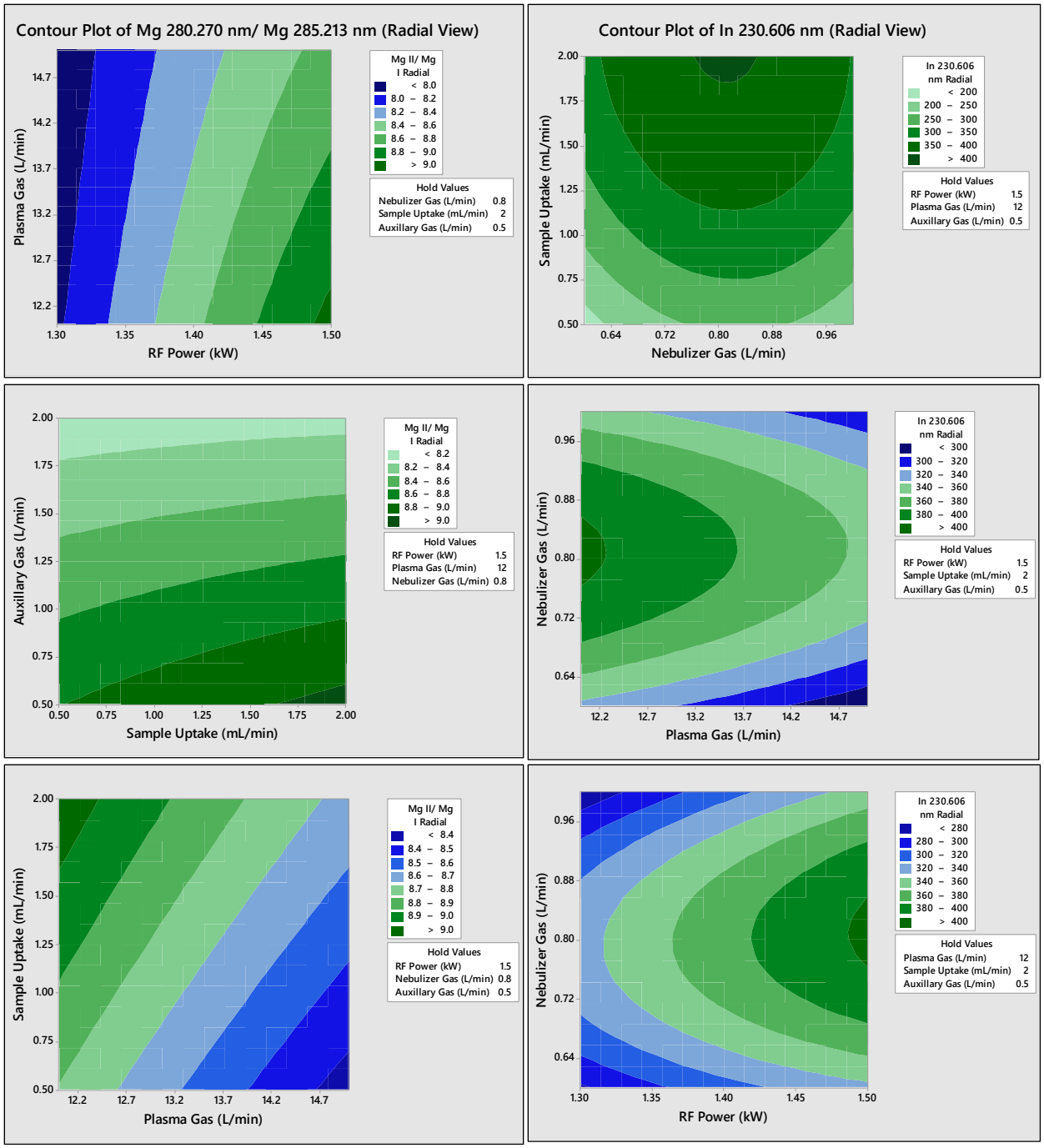

Figure 4.9: Contour plots for the multivariate optimization of the inert plastic setup with prototype (V-groove) nebuliser in lateral viewing mode. Values are held in order to find the optimal compromised conditions for two other parameters. At left, Mg 280.270 nm and 285.213 nm emission intensities have been blank-subtracted, with the ratio providing an indication of robustness. At right, blank-subtracted In 230.606 nm emission intensities are shown.

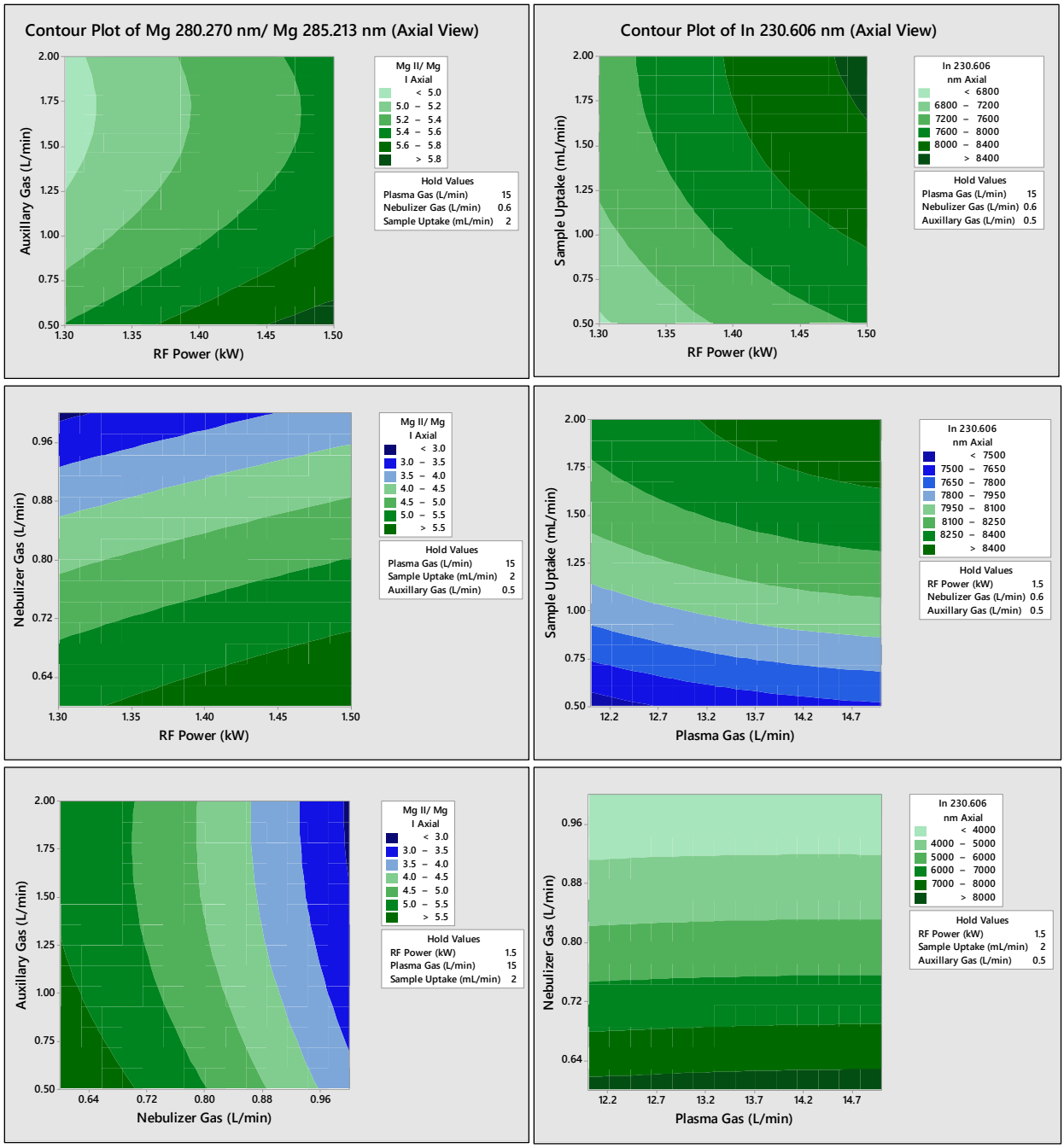

Figure 4.10: Contour plots for the multivariate optimization of the inert plastic setup with OneNeb nebuliser in axial viewing mode. Values are held in order to find the optimal compromised conditions for two other parameters. At left, Mg 280.270 nm and 285.213 nm emission intensities have been blank-subtracted, with the ratio providing an indication of robustness. At right, blank-subtracted In 230.606 nm emission intensities are shown.

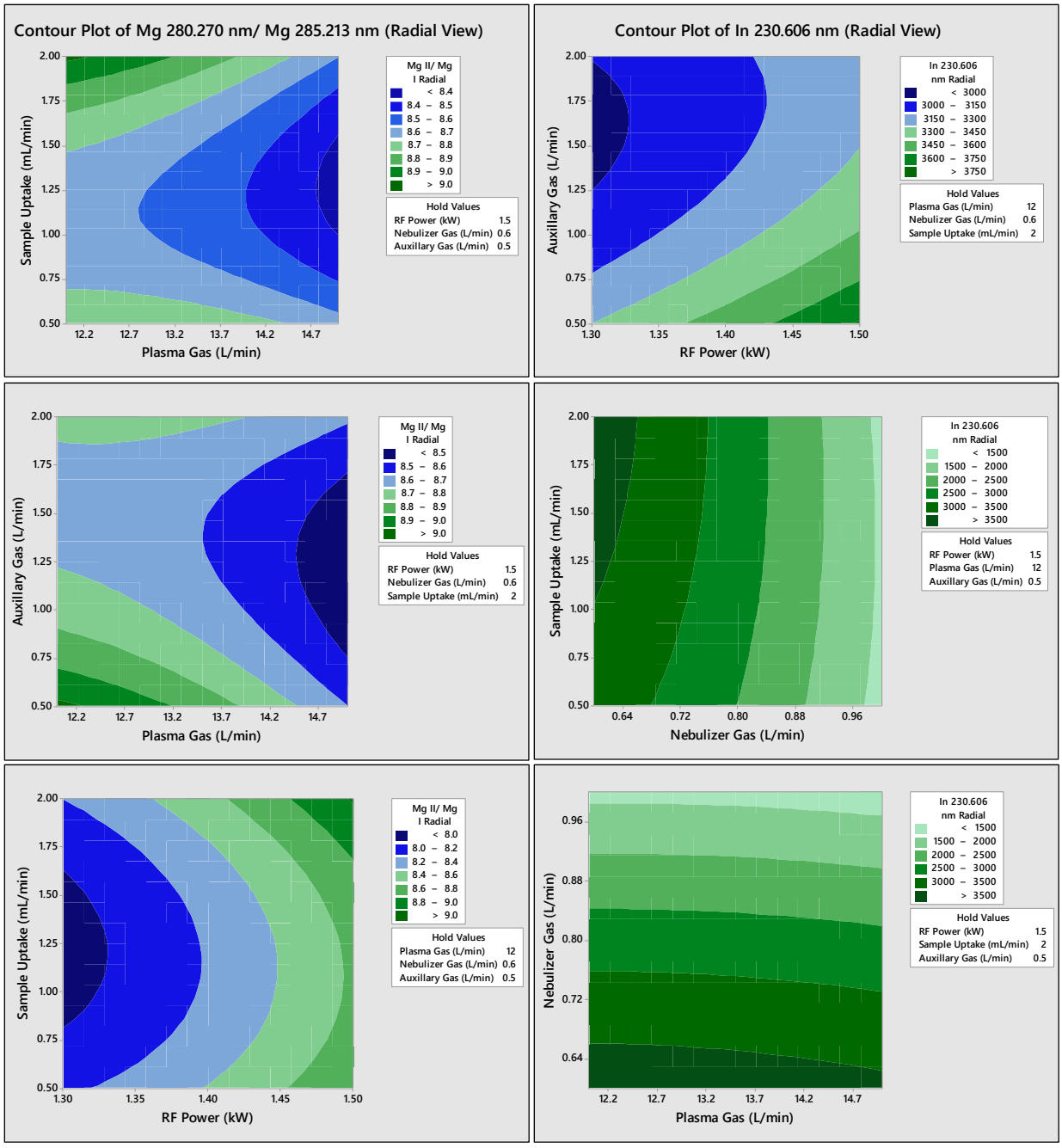

Figure 4.11: Contour plots for the multivariate optimization of the inert plastic setup with OneNeb nebuliser in lateral viewing mode. Values are held in order to find the optimal compromised conditions for two other parameters. At left, the ratio of blank-subtracted Mg 280.270 nm and 285.213 nm emission indicates robustness. At right, blank subtracted In 230.606 nm emission intensities are shown.

4.3.2 Sensitivity, detection limit, and precision

Sensitivity, defined as the slope of the calibration curve, was compared with several lines of each elemental analyte for axial and lateral modes of both the prototype V-groove and OneNeb nebulisers (Table 4.3), in addition to detection limits (Table 4.4) and instrumental precision (Table 4.5). As the V-groove nebuliser is not yet on the market, this information was important to Agilent Technologies. Currently, the company markets the OneNeb as a revolutionary nebuliser providing high sensitivity with its Flow Blurring technology, improved detection limits, and precisions under 1% RSD. The goal herein was to explore if the V-groove's analytical capabilities are comparable to that of the OneNeb. Tables 4.3-4.5 are colour-coded to demonstrate the comparisons of methods for each element line (each row) where dark green indicates the best value (i.e. highest sensitivity, lowest detection limit, and lowest %RSD), yellow indicates a middle-ground value, and red indicates the worst value (i.e. lowest sensitivity, highest detection limit, and highest %RSD). From this colour scale, it is clear that axial view with the OneNeb generally provided the highest sensitivities, lowest detection limits, and lowest %RSD, while lateral view with the V-groove had the lowest sensitivities, and highest detection limits. Axial view with the V-groove appeared to result in the largest %RSD. Since the element lines are ranked from lowest wavelength to highest, it is also interesting to note that lateral view tended to have greater sensitivities and lower detection limits for elements of lower wavelength, while axial view saw the opposite trend.

Average improvement factors for the OneNeb method over the V-groove method were 1.9 ± 0.2 (1.5 ± 0.2) for sensitivity, 1.8 ± 1.3 (3.2 ± 4.3) for detection limit, and 1.4 ± 0.6 (1.9 ± 2.1) for %RSD, where lateral view comparisons are given first, and axial view comparisons are in brackets. While these averages agree with the colour coding in terms of the OneNeb providing enhanced analytical proficiency, it is apparent that the level of improvement is not drastic. Generally speaking, an

improvement factor of 10 or more is considered to be noteworthy. Therefore, the results on the prototype V-groove are comparable to the OneNeb.

Table 4.3: Sensitivities with Inert Setups (cps per ng mL^{-1})

Element Line (nm)	Lateral OneNeb	Lateral V-Groove	Axial OneNeb	Axial V-Groove
Al 167.019	6.9	3	1.5	1.6
C 175.122	0.12	0.057	0.037	0.028
C 193.027	9.4	4.4	5.2	3.7
Zn 202.548	29	13	25	17
Zn 206.200	3.8	1.7	3.3	2.8
Zn 213.857	26	15	31	20
In 230.606	0.86	0.47	1.6	1
Fe 234.350	6.4	3.4	9.5	6.3
Al 237.312	0.73	0.46	1.5	0.81
Fe 238.204	26	14	35	24
C 247.856	1.1	0.49	0.79	0.52
Si 250.690	1.8	1	3.3	1.9
Si 251.611	1.7	0.94	2.9	1.8
Fe 259.940	10	5.4	15	10
Mg 279.553	410	210	620	370
Mg 280.270	85	48	150	73
Mg 285.213	9.8	5.8	20	14
Si 288.158	3.5	1.9	6	3.6
In 303.936	0.34	0.19	0.94	0.58
In 325.609	1.3	0.71	3.5	2.1
Al 396.152	10	5.8	33	21
K 404.721	0.0024	0.0015	0.016	0.0097
K 766.491	2.4	1.3	46	33
K 769.897	1.8	0.97	41	28

Table 4.4: Detection Limits with Inert Setups (ng/mL)

Element Line (nm)	Lateral OneNeb	Lateral V-Groove	Axial OneNeb	Axial V-Groove
Al 167.019	0.8	3	7	3
C 175.122	200	200	300	500
C 193.027	50	30	60	30

Zn 202.548	1	3	0.6	10
Zn 206.200	3	10	4	9
Zn 213.857	1	3	0.6	10
In 230.606	50	40	20	30
Fe 234.350	7	4	2	5
Al 237.312	30	30	20	40
Fe 238.204	1	2	0.7	1
C 247.856	80	70	60	80
Si 250.690	30	20	9	20
Si 251.611	10	30	4	10
Fe 259.940	4	7	1	2
Mg 279.553	0.1	0.1	0.04	0.08
Mg 280.270	0.3	0.4	0.2	0.4
Mg 285.213	5	4	1	2
Si 288.158	20	20	5	7
In 303.936	100	200	20	50
In 325.609	70	60	20	30
Al 396.152	10	9	1	5
K 404.721	20000	40000	3000	4000
K 766.491	100	600	4	20
K 769.897	500	600	100	60

Table 4.5: Instrumental precisions (% relative standard deviation for 100ppb, n=10) with Inert Setups

Element Line (nm)	Lateral OneNeb	Lateral V-Groove	Axial OneNeb	Axial V-Groove
Al 167.019	1	0.83	0.98	0.49
C 175.122	1.2	1.4	2.2	1.9
C 193.027	0.95	1.3	0.79	0.48
Zn 202.548	0.55	0.52	0.33	0.71
Zn 206.200	0.43	0.46	0.36	0.75
Zn 213.857	0.37	0.52	0.3	0.76
In 230.606	0.51	1.5	0.55	0.95
Fe 234.350	0.31	0.56	0.42	0.74
Al 237.312	0.67	0.71	0.86	0.87
Fe 238.204	0.66	1.5	0.32	1.1
C 247.856	0.89	1.3	0.87	0.45
Si 250.690	0.5	0.6	0.82	6.1
Si 251.611	0.46	0.67	0.95	3.8
Fe 259.940	0.48	0.62	0.4	0.74

Mg 279.553	0.63	0.59	0.5	0.97
Mg 280.270	0.72	0.61	0.64	0.85
Mg 285.213	0.59	0.53	1.3	0.78
Si 288.158	0.42	0.61	0.66	5.7
In 303.936	0.5	1.3	1	0.61
In 325.609	0.39	0.7	1.2	0.56
Al 396.152	0.42	0.56	1.7	0.73
K 404.721	110	69	30	43
K 766.491	0.96	1.2	1.5	0.63
K 769.897	0.66	0.81	1.4	0.53

4.3.3 Flow injection method

Tables 4.6 and 4.7 list results for flow injection experiments using the prototype V-groove nebuliser method (Table 4.1). Fuel was analyzed both as undiluted samples, and as samples diluted 4-fold with pure 12 M KOH. While the diluted method typically resulted in concentrations closer to the values provided by ZincNyx, it was also noticed that these measured values were sometimes far above the given values (i.e. in the case of In for both axial and lateral viewing modes). On the other hand, concentrations found by the undiluted experiment never exceeded the concentrations specified by ZincNyx. In fact, the concentrations found by the undiluted method were all less than the ZinxNyx value, suggesting that the dissolved analytes (Al, C, Fe, In, Mg, Si) were decreasing in concentration. This idea was investigated further in section 4.3.6. Since zinc concentrations were consistently drastically lower than the ZincNyx value for all methods attempted, and because potassium concentration could not be determined by this method, as 12 M KOH was used as the blank, other methods were required for further investigation of all analytes.

Table 4.6: Axial view results (mg/L, n=5) for undiluted liquid fuel and liquid fuel diluted 1/4 with 12 M KOH. N/A denotes values not provided by ZincNyx.

Line (nm)	Undiluted	Undiluted Error (±)	Diluted	Diluted Error (±)	ZincNyx
Al (167.019)	4.88	0.085	6.70	0.25	7.7
Al (237.312)	4.78	0.15	6.15	0.27	7.7
Al (396.152)	3.89	0.1	4.45	0.08	7.7
C (175.122)	694	15	1050	31	N/A
C (193.027)	318	8	454	12	N/A
C (247.856)	289	10	404	14	N/A
Fe (234.350)	0.247	0.140	0.405	0.034	<2.0
Fe (238.204)	0.170	0.150	0.161	0.014	<2.0
Fe (259.940)	0.217	0.150	0.319	0.018	<2.0
In (230.606)	0.844	0.170	2.46	0.078	<2.0
In (303.936)	1.46	0.25	5.05	0.39	<2.0
In (325.609)	0.720	0.210	2.49	0.22	<2.0
Mg (279.553)	0.920	0.086	1.07	0.011	3.6
Mg (280.270)	0.932	0.083	1.08	0.062	3.6
Mg (285.213)	0.895	0.073	1.26	0.019	3.6
Si (250.690)	2020	81	2200	60	2021
Si (251.611)	1890	74	2180	56	2021
Si (288.158)	1990	62	2160	36	2021
Zn (202.548)	1950	27	4670	160	77051
Zn (206.200)	3430	43	7980	340	77051
Zn (213.857)	2380	32	5350	210	77051

Table 4.7: Lateral view results (mg/L, n=5) for undiluted liquid fuel and liquid fuel diluted 1/4 with 12 M KOH. N/A denotes values not provided by ZincNyx.

Line (nm)	Undiluted	Undiluted Error (±)	Diluted	Diluted Error (±)	ZincNyx
Al (167.019)	4.20	0.08	4.57	0.07	7.7
Al (237.312)	5.84	0.40	10.2	1.0	7.7
Al (396.152)	4.27	0.10	4.15	0.10	7.7
C (175.122)	181	4	196	2	N/A
C (193.027)	142	3	142	2	N/A
C (247.856)	140	3	138	3	N/A
Fe (234.350)	0.254	0.050	0.652	0.10	<2.0
Fe (238.204)	0.203	0.060	0.488	0.03	<2.0

Fe (259.940)	0.250	0.060	0.697	0.06	<2.0
In (230.606)	2.32	0.10	8.83	0.90	<2.0
In (303.936)	4.75	0.60	15.8	2.0	<2.0
In (325.609)	2.86	0.20	9.23	0.80	<2.0
Mg (279.553)	0.770	0.030	0.924	0.02	3.6
Mg (280.270)	0.860	0.020	1.27	0.03	3.6
Mg (285.213)	0.960	0.040	1.61	0.02	3.6
Si (250.690)	1980	60	1810	40	2021
Si (251.611)	1970	60	1820	30	2021
Si (288.158)	1950	60	1780	30	2021
Zn (202.548)	6130	200	12200	100	77051
Zn (206.200)	10200	200	18500	200	77051
Zn (213.857)	6530	200	13500	200	77051

4.3.4 Dilution method

In order to measure the concentration of K in the potassium zincate electrolyte fuel, and explore alternative methods of analyzing the dissolved analytes in the fuel, samples of fuel were diluted 10 and 100-fold in DDW and analyzed in a conventional operation (without flow injection) with both the OneNeb and prototype V-groove nebuliser (Table 4.8). While Mg and Fe were undetectable in the fuel when diluted 10 and 100-fold, In was only detectable when using the prototype V-groove nebuliser. However, when comparing different element lines for the same element and same method, the results via the dilution methods appeared less reliable than those of the FI method. Moreover, the results showed increased concentrations for all analytes when compared to FI results. It was also observed that diluting 100-fold resulted in even larger concentration increases than diluting 10-fold did, indicating that a change in nebulizer efficiency with the changes in sample viscosity was resulting in changes to the element signals. This reasoning follows from the fact that only the different samples would vary in viscosity, while the standards were prepared in DDW rather than diluted KOH. The rate of uptake by a nebuliser is affected by a solution's viscosity, and the surface tension impacts the size distribution of droplets produced by the nebulizer. For instance in one analysis, signal responses of a 5 ppm Fe

standard in a glacial acetic acid solvent were monitored as increasing percentages of a viscous mineral oil were added. This analysis proved that an increase in oil resulted in a decreased Fe intensity signal [17]. In other words, an aerosol generated from a solution of high viscosity generally has a larger average droplet size than that of water, meaning that the inertial, gravitational, and centrifugal losses of larger droplets in the spray chamber are higher, and aerosol transport efficiency is reduced [18]. The 10-fold dilution, being more viscous, therefore felt a greater loss in nebulizer efficiency, and a resulting greater decrease in signal intensity, in comparison to the 100-fold diluted fuel. Despite this disruption to nebuliser efficiency, this preparation technique had to be used in order to measure the K concentration while simultaneously measuring the content of dissolved analytes, and to avoid assumptions that the "pure" 12 M KOH was in fact free of contamination (section 4.3.8).

Since Si was the only dissolved analyte to not have drastically lower concentrations (when compared to ZincNyx values) via the FI method, it was used as a reference point in investigating the enhancement of signal by the dilution methods (Fig 4.12). In other words, it was assumed that if the dissolved analytes were in fact being "lost" from the fuel, Si was exempt from this problem, and could be observed from a purely method-based comparison.

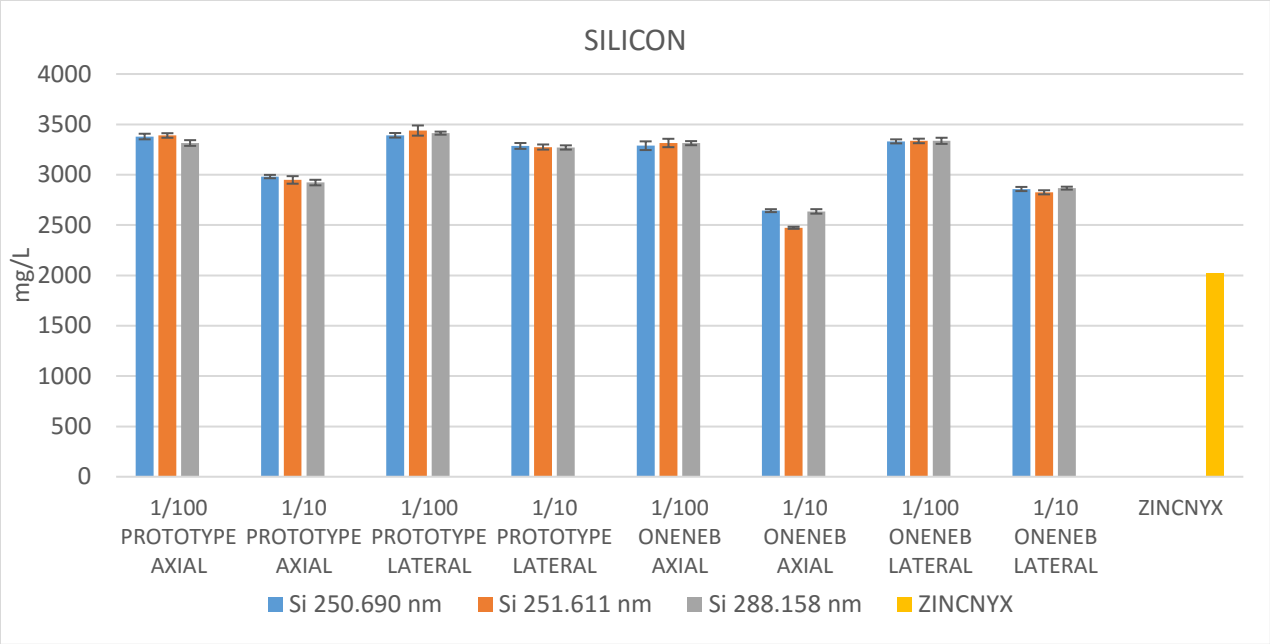

Figure 4.12: Comparisons of dilution methods, using silicon as a reference analyte (n=5).

While Zn concentration readings were also seen to increase compared to the FI method, the results were still far below the value given by ZincNyx, hence the further investigations of section 4.3.5. K concentrations were found to be far lower than expected when monitoring the most sensitive lines (766.491 nm and 769.897 nm); however, the 404.721 nm emission line appeared promising when analyzing the 10-fold diluted fuel in axial mode. Using a less-sensitive line, free from the possibility of saturating the detector (as was the case for the 766.491 nm and 769.897 nm lines), with the most-sensitive viewing mode was therefore chosen as the best prospect for K analysis.

Table 4 8: Comparison of methods for analysing fuel diluted with DDW (mg/L, n=5). N/A denotes values not provided by ZincNyx, and empty sections indicate the analyte was undetectable.

Element Line (nm)	1/100 PROTOTYPE AXIAL	1/10 PROTOTYPE AXIAL	1/100 PROTOTYPE LATERAL	1/10 PROTOTYPE LATERAL	1/100 ONENEB AXIAL	1/10 ONENEB AXIAL	1/100 ONENEB LATERAL	1/10 ONENEB LATERAL	ZINCNYX
C 175.122	658 ± 28	326 ± 5	471 ± 8	349 ± 3	573 ± 18	284 ± 1	522 ± 8	298 ± 1	N/A
C 193.027	579 ± 36	333 ± 2	441 ± 2	351 ± 2	510 ± 20	287 ± 1	477 ± 2	296 ± 1	N/A
C 247.856	400 ± 31	300 ± 2	359 ± 2	341 ± 2	353 ± 19	251 ± 1	399 ± 5	283 ± 2	N/A
Zn 202.548	20400 ± 67	2390 ± 9	44700 ± 200	11800 ± 33	12000 ± 40	1310 ± 5	36500 ± 160	6530 ± 16	77100
Zn 206.200	28700 ± 167	3760 ± 13	50900 ± 170	18800 ± 60	21900 ± 72	2440 ± 13	44200 ± 190	10700 ± 24	77100
Zn 213.857	25100 ± 61	3280 ± 13	44600 ± 300	12900 ± 74	13900 ± 45	1700 ± 4	36700 ± 170	8420 ± 33	77100
In 230.606			20.1 ± 1.6	2.06 ± 0.27					<2
In 303.936	26.5 ± 0.9	2.76 ± 0.23	6.4 ± 3.2	1.44 ± 1.00					<2
In 325.609	9.29 ± 1.23	0.842 ± 0.065	6.2 ± 2.6	0.58 ± 0.36					<2
Al 237.312		2.9 ± 0.2		6.18 ± 0.24		2.23 ± 0.11		5.12 ± 0.32	7.7
Al 396.152	34.7 ± 0.3	7.57 ± 0.04		5.12 ± 0.11		2.91 ± 0.04	6.82 ± 1.04	5.55 ± 0.037	7.7
Si 250.690	3380 ± 28	2980 ± 17	3390 ± 23	3290 ± 29	3290 ± 43	2640 ± 15	3330 ± 20	2860 ± 21	2020
Si 251.611	3390 ± 23	2950 ± 38	3440 ± 51	3270 ± 25	3320 ± 42	2470 ± 11	3340 ± 22	2830 ± 20	2020
Si 288.158	3310 ± 28	2920 ± 28	3410 ± 15	3270 ± 21	3310 ± 20	2640 ± 22	3340 ± 30	2870 ± 15	2020
K 404.721	706000 ± 8300	488000 ± 2300	591000 ± 2000	569000 ± 2700	688000 ± 4800	465000 ± 4000	616000 ± 6000	548000 ± 2600	477000
K 766.491			382000 ± 4320	99600 ± 1190			162000 ± 1400	32600 ± 793	477000
K 769.897			404000 ± 2760	169000 ± 1490			250000 ± 1900	53800 ± 1270	477000

4.3.5 Standard additions method

Since zinc concentrations were still far below the expected value when using the dilution method and flow injection method, a third method was attempted in which ZnO powder was dissolved in fuel samples for standard additions analysis. Examples of flow injection peak replicates of 0.28 g ZnO added to a fuel sample diluted 4-fold with DDW are shown in Fig. 4.13. The standard additions method proved to be the most successful in determining Zn concentration, particularly when the least sensitive Zn lines were monitored (i.e. Zn 210.442 nm, 330.258 nm, and 334.502 nm). The more sensitive emission lines were likely to produce drastically enhanced concentration readings due to saturation of the detector, and the subsequent inability to read a true signal. Since axial results had a greater deviation from the known Zn concentration than lateral results did when comparing the 10-fold standard addition dilution experiments, future standard addition experiments were only investigated in lateral view. The results of all Zn standard additions experiments are presented in Fig. 4.14-4.17. These experiments were done with the V-groove prototype alone.

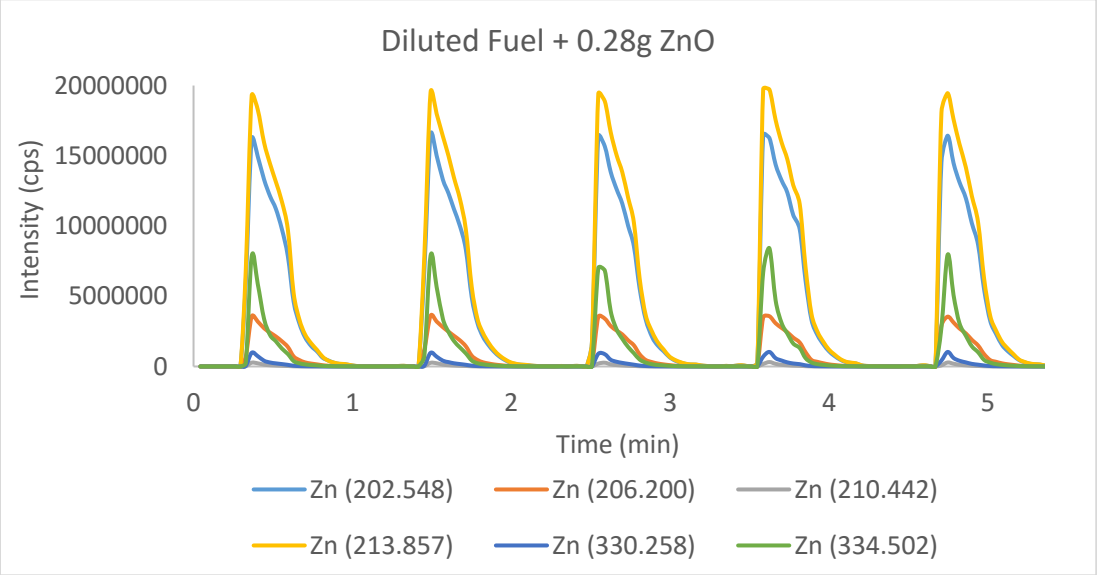

Figure 4.13: Example of flow injection profiles in lateral view for 4-fold diluted fuel with ZnO added for standard additions of Zn. Emission lines are in nm.

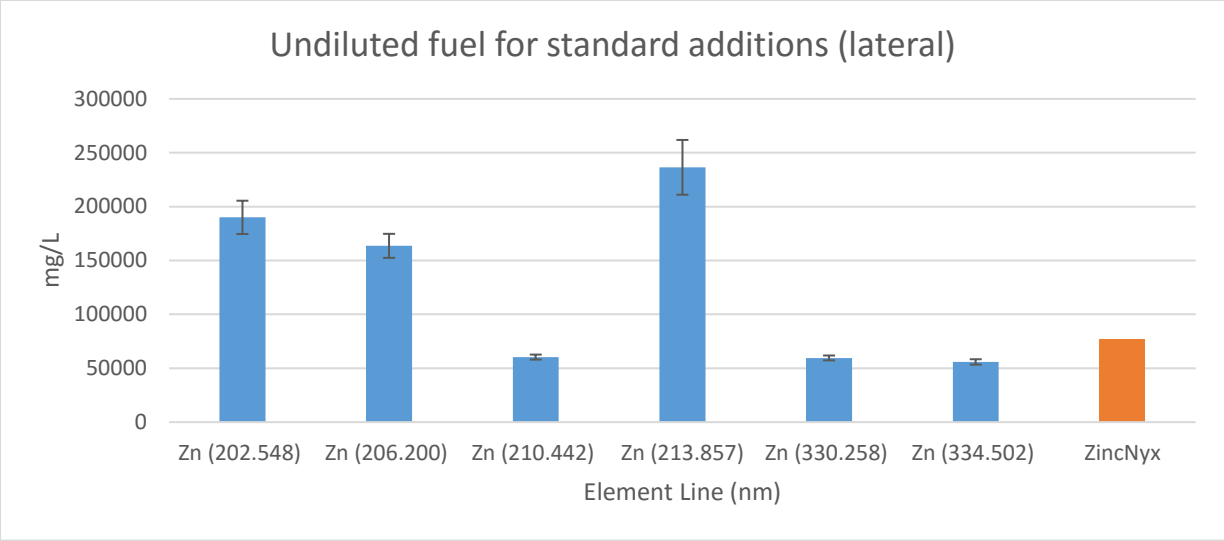

Figure 4.14: Lateral view standard addition experiment for undiluted fuel (n=5)

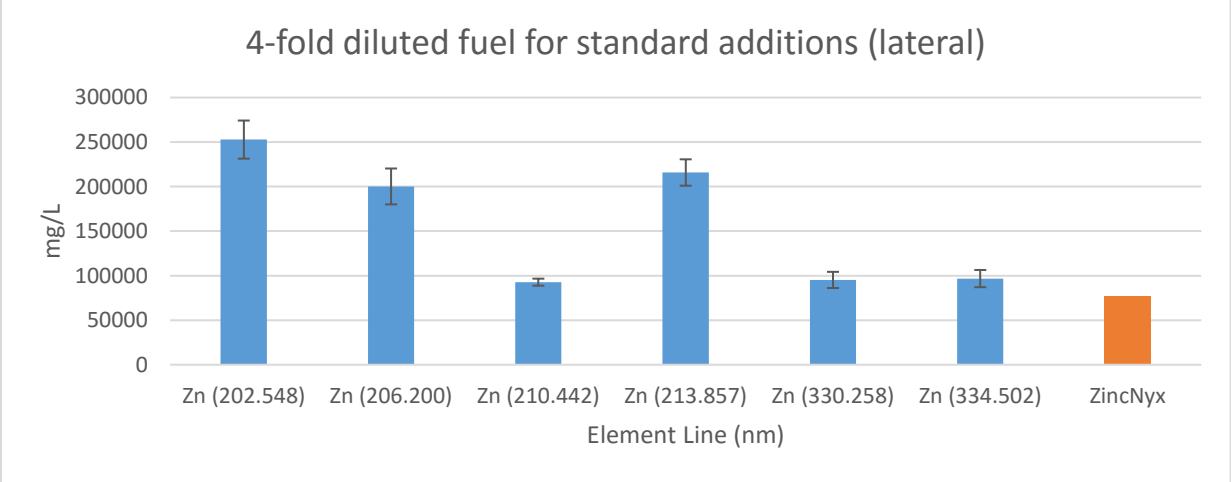

Figure 4.15: Lateral view standard addition experiment for fuel diluted 1/4 with DDW (n=5)

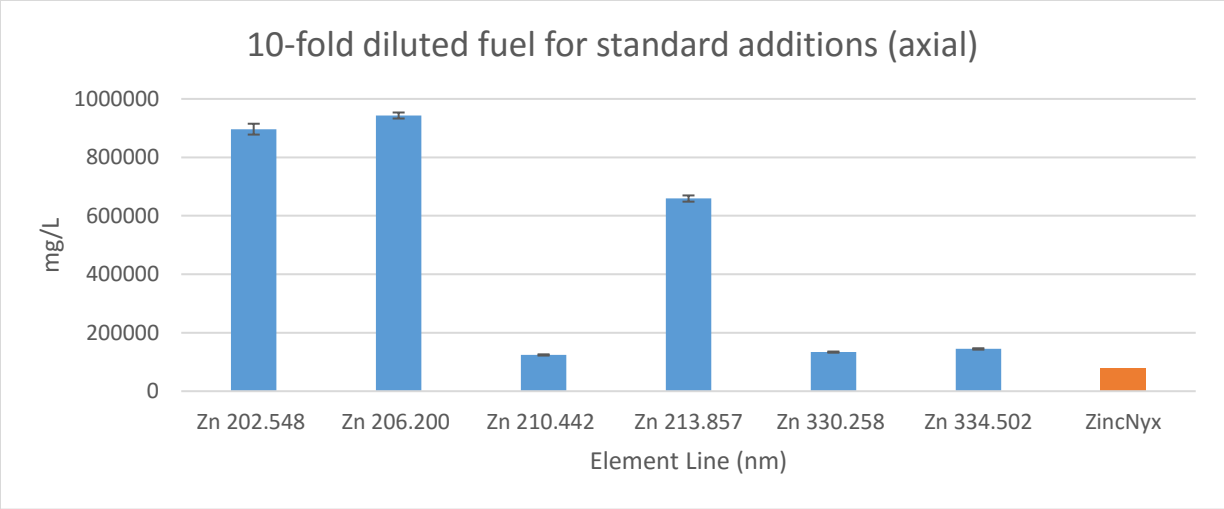

Figure 4. 16: Axial view standard addition experiment for fuel diluted 1/10 in DDW (n=5)

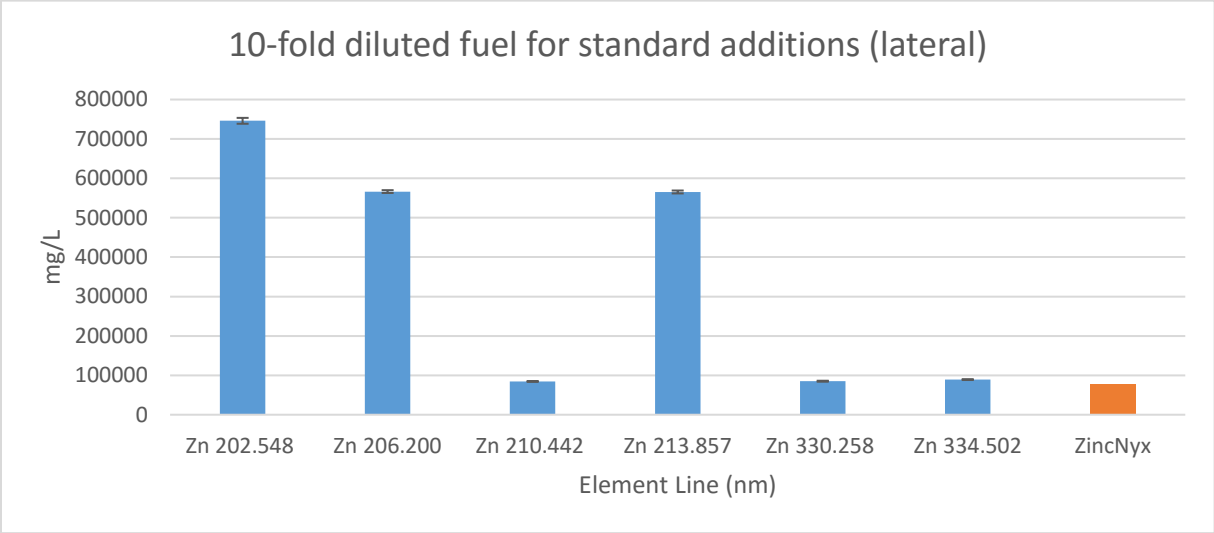

Figure 4.17: Lateral view standard addition experiment for fuel diluted 1/10 in DDW (n=5)

Given the promising results for Zn standard additions, similar experiments were conducted for K analysis, in which KNO_3 was added to 4, 10 and 100-fold diluted fuel (Fig. 4.18-4.21). Undiluted fuel with K standard additions was also tested, yet the detector was saturated by the extremely high concentrations. Again, the least sensitive K lines provided the most accurate results. Although these lines proved to be closer to the known K value than the most sensitive lines, comparisons to the 10 and 100-fold dilution method without standard additions proved that the latter actually produced the most

accurate results. In terms of standard additions experiments alone, the 100-fold dilution (Fig. 4.20-4.21) provided the closest match in concentration, likely because KNO_3 could dissolve more completely in the highly water-based matrix.

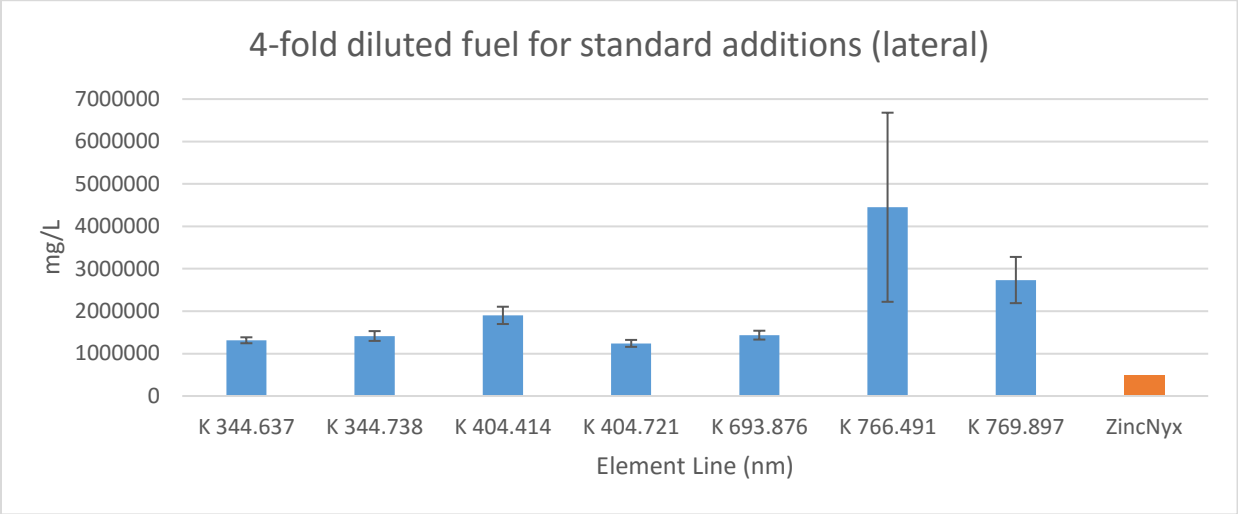

Figure 4.18: Lateral view standard addition experiment for fuel diluted 1/4 with DDW (n=5)

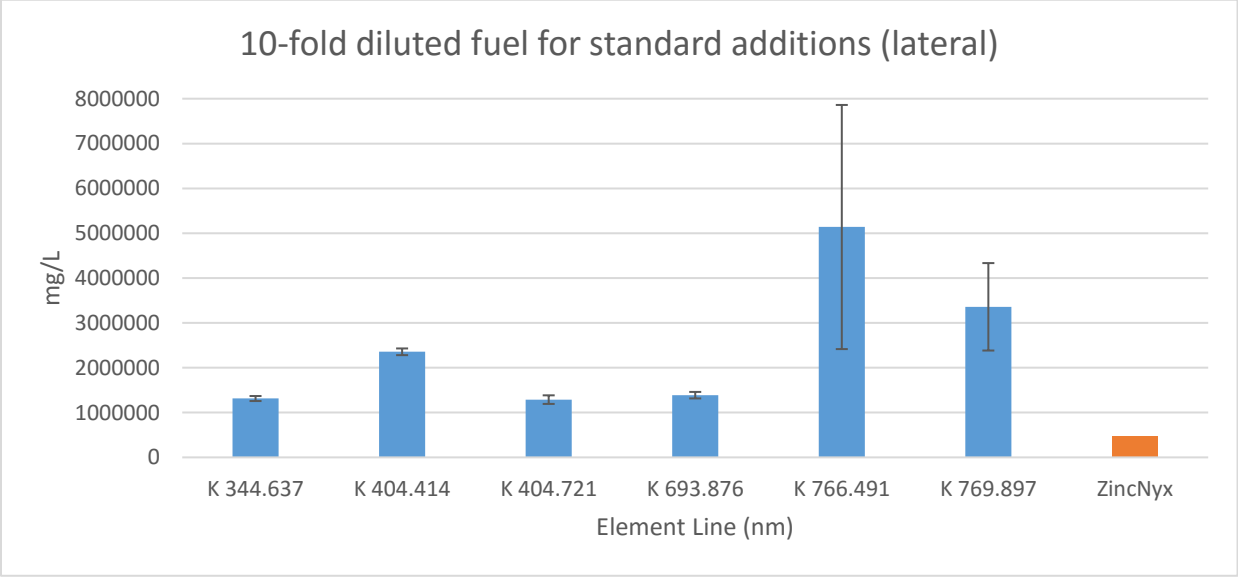

Figure 4.19: Lateral view standard addition experiment for fuel diluted 1/10 with DDW (n=5)

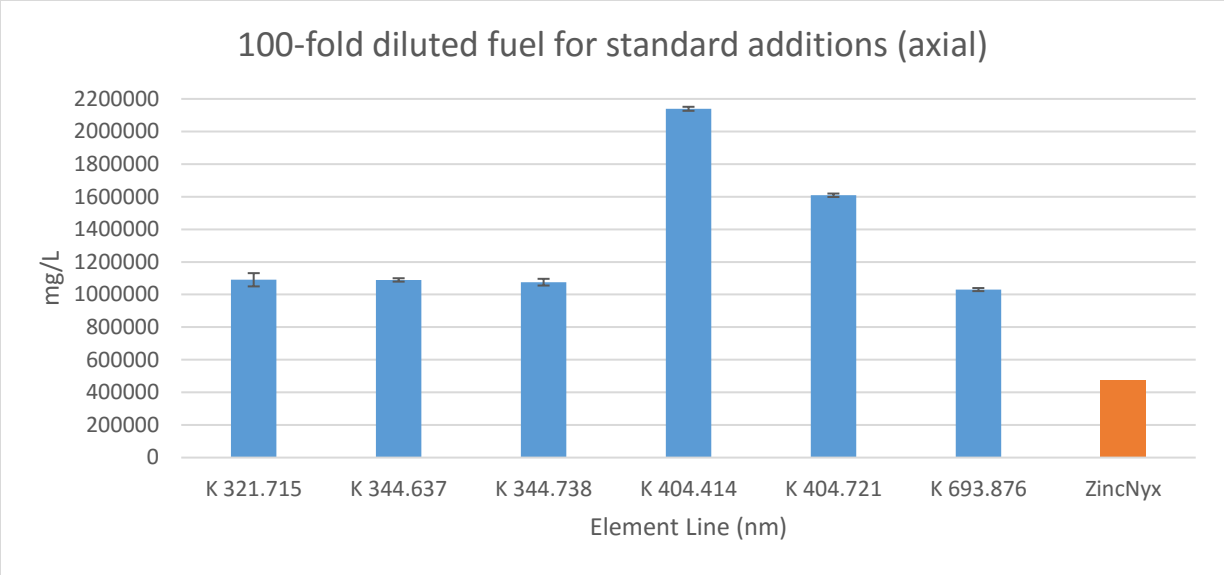

Figure 4.20: Axial view standard addition experiment for fuel diluted 1/100 with DDW (n=5)

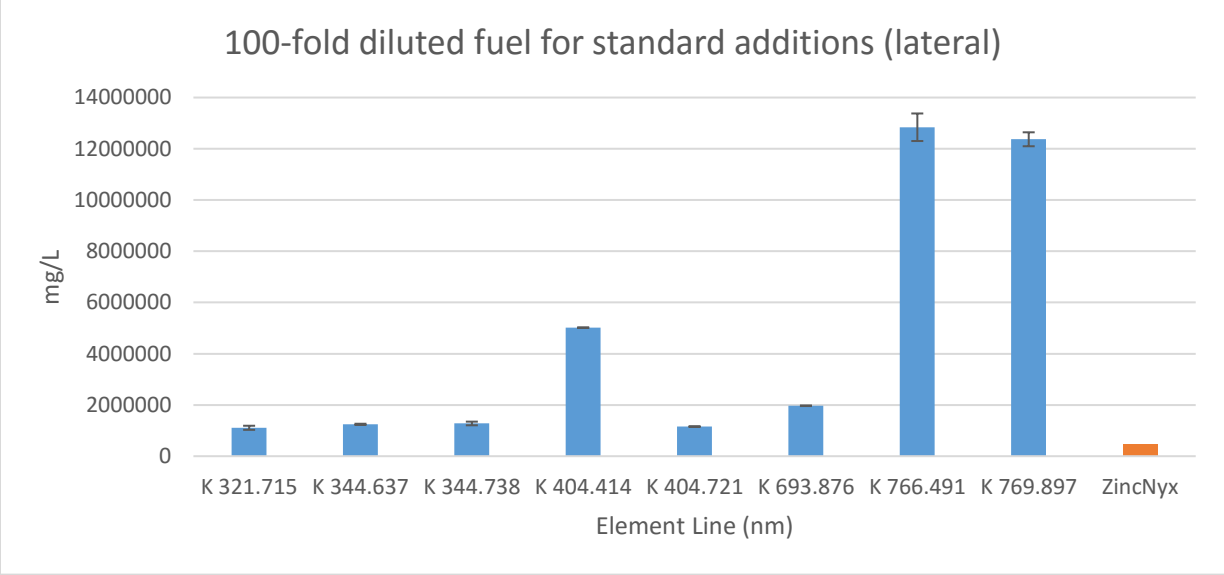

Figure 4.21: Lateral view standard addition experiment for fuel diluted 1/100 with DDW (n=5)

4.3.6 Fuel exposure analysis

The following graphs (Fig. 4.22-4.35) show the effects of leaving the potassium zincate electrolyte fuel exposed to air in a closed and open bottle (labelled “closed” and “open”, respectively) and an exposed beaker (labelled “exposed”) for periods of 12 hours, 24 hours, 96 hours, and 10 days. These results are shown for both lateral and axial views, and demonstrate the effects of potassium carbonate precipitate formation in the fuel. By reacting with the carbon dioxide in the air, the precipitate was formed along the exposed fuel’s surface. Hence an increase in carbon concentration is seen when a greater surface area of fuel was exposed (i.e. in the beaker), and when the fuel was exposed to air for a longer period of time. Upon examining all other elemental analytes, it is found that with longer exposure to air comes a decrease in elemental analyte concentration (within error). In the case of the closed bottle, even the headspace of air is enough to allow for precipitate formation. This suggests that as the potassium carbonate precipitate formed, dissolved analytes were drawn out of the liquid fuel and collected in the precipitate. Therefore, the discrepancy between results in section 4.3.3 and the concentrations provided by ZincNyx were due to the analyzed fuel aging in its bottle prior to analysis. In fact, this fuel was prepared 2 months prior to analysis – more than enough time for precipitate to form from the bottle’s air headspace. Of special consideration are the graphs for silicon, as it is possible that silicon from the glass beaker was etched by KOH, resulting in an increase in silicon concentration over longer exposure. For instance, in Fig. 4.24 the concentration at 24 hours in the exposed beaker is greater than that at 12 hours.

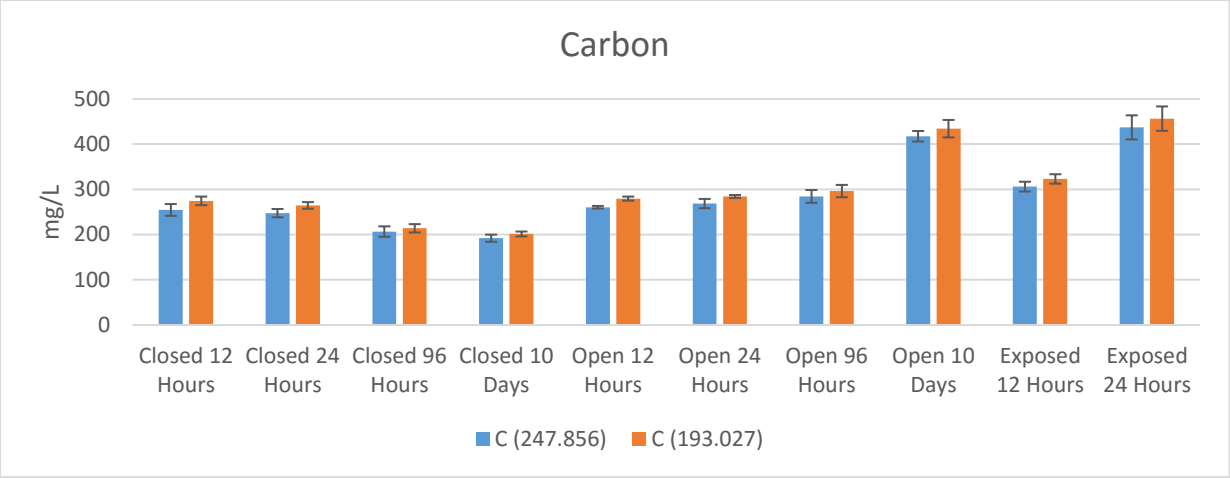

Figure 4.22: Lateral view exposure test of carbon in 12 M KOH filtered fuel (n=5)

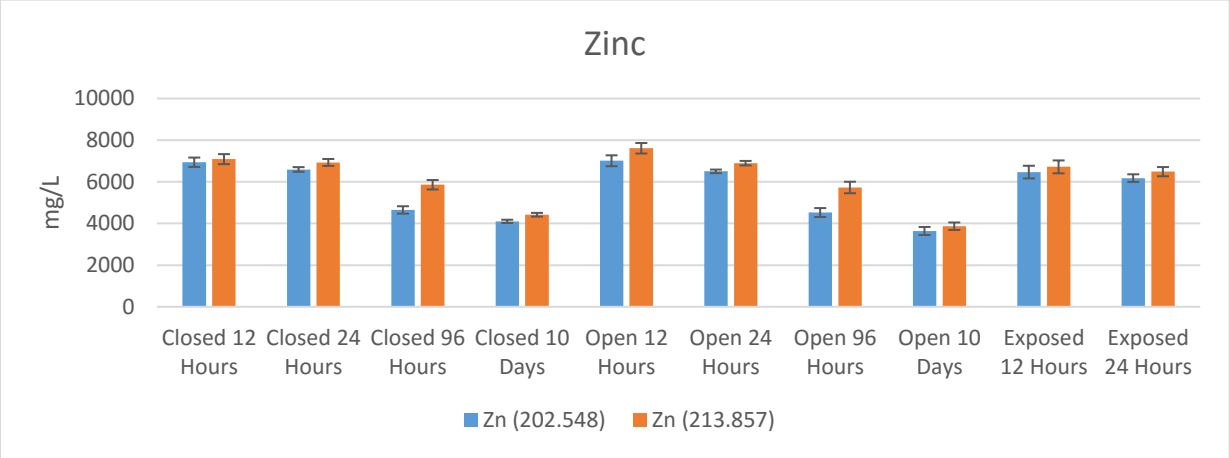

Figure 4.23: Lateral view exposure test of zinc in 12 M KOH filtered fuel (n=5)

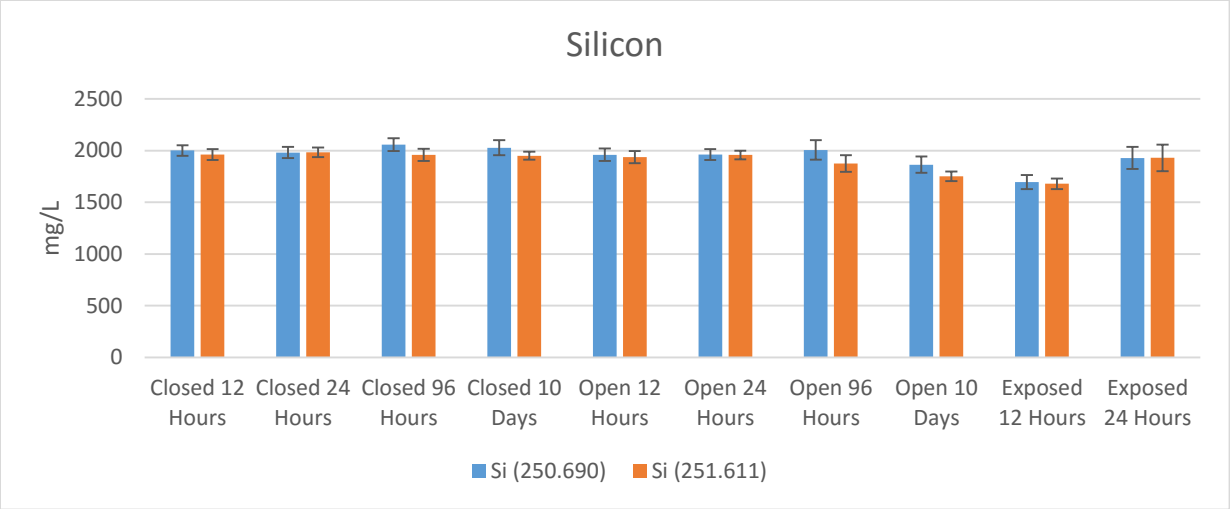

Figure 4.24: Lateral view exposure test of silicon in 12 M KOH filtered fuel (n=5)

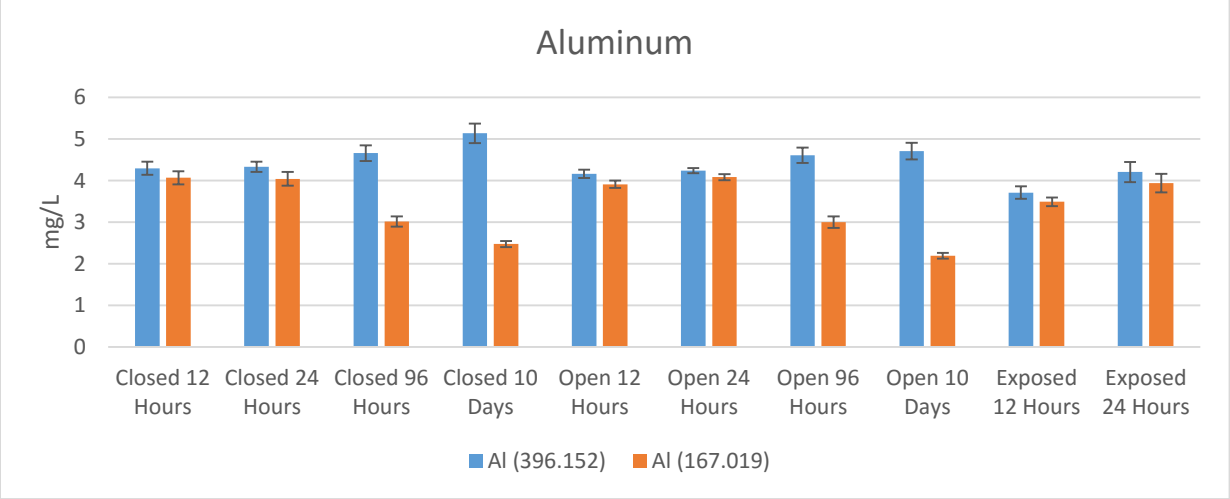

Figure 4.25: Lateral view exposure test of aluminum in 12 M KOH filtered fuel (n=5)

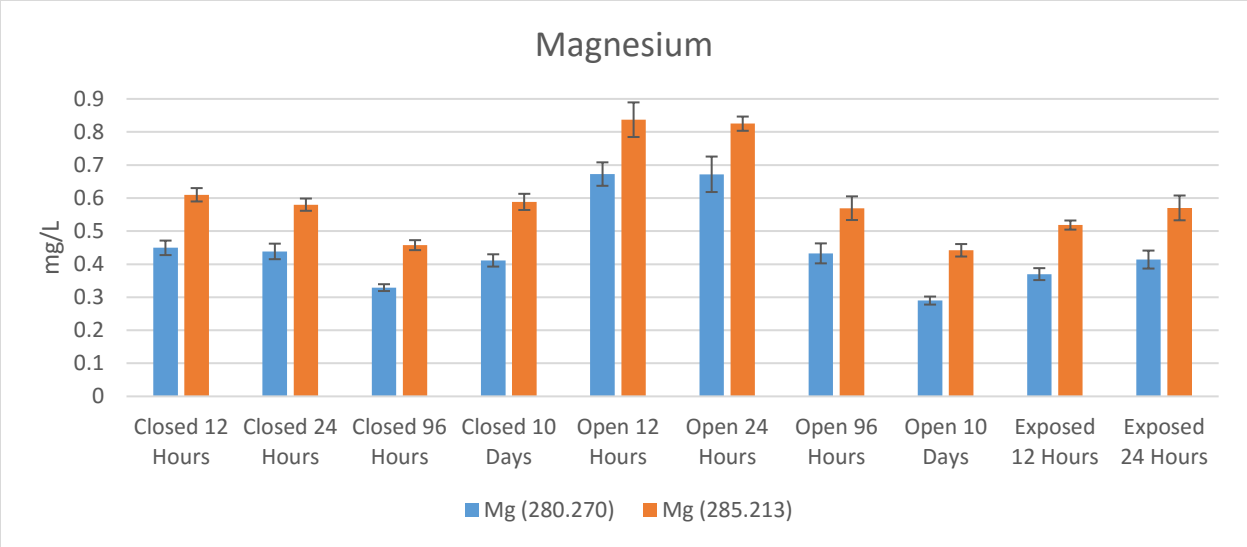

Figure 4.26: Lateral view exposure test of magnesium in 12 M KOH filtered fuel (n=5)

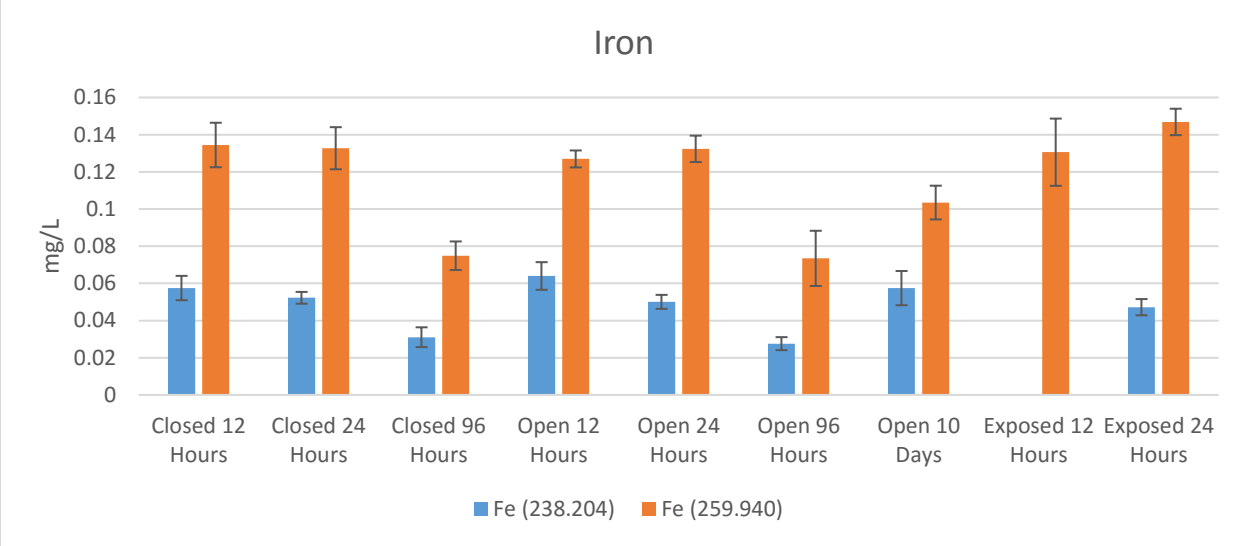

Figure 4.27: Lateral view exposure test of iron in 12 M KOH filtered fuel (n=5)

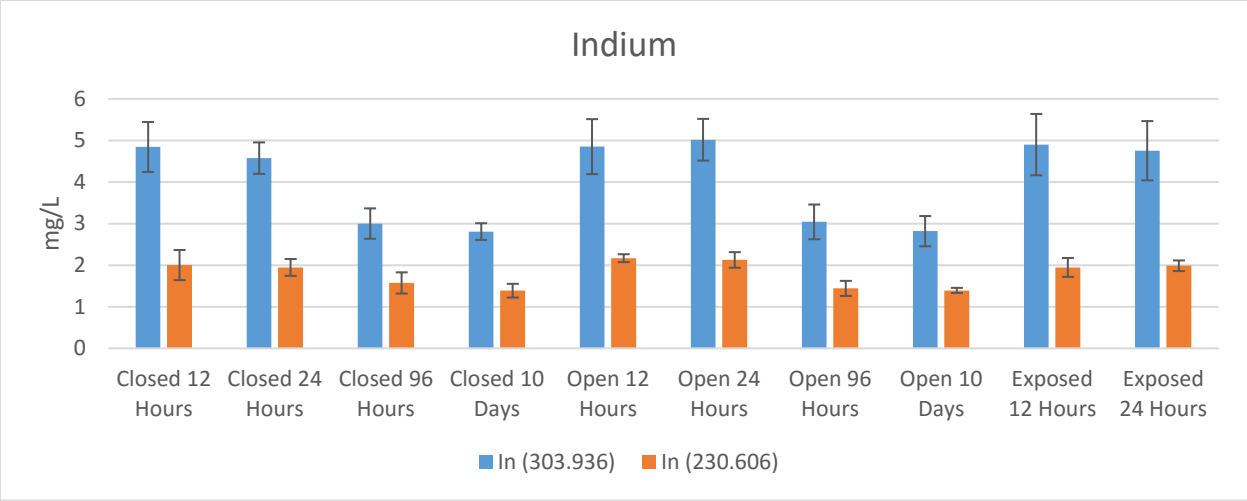

Figure 4.28: Lateral view exposure test of indium in 12 M KOH filtered fuel (n=5)

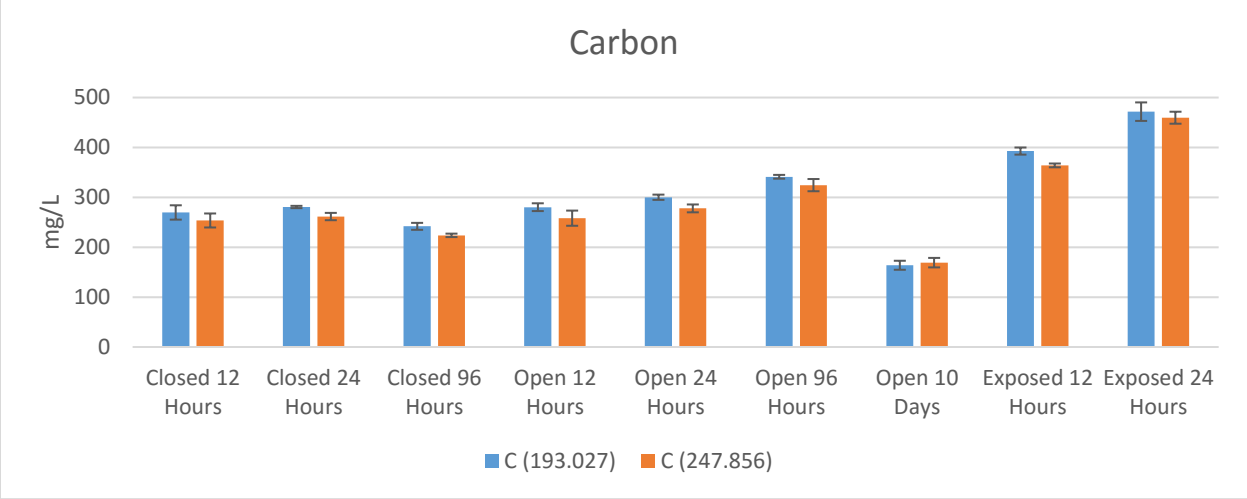

Figure 4.29: Axial view exposure test of carbon in 12 M KOH filtered fuel (n=5)

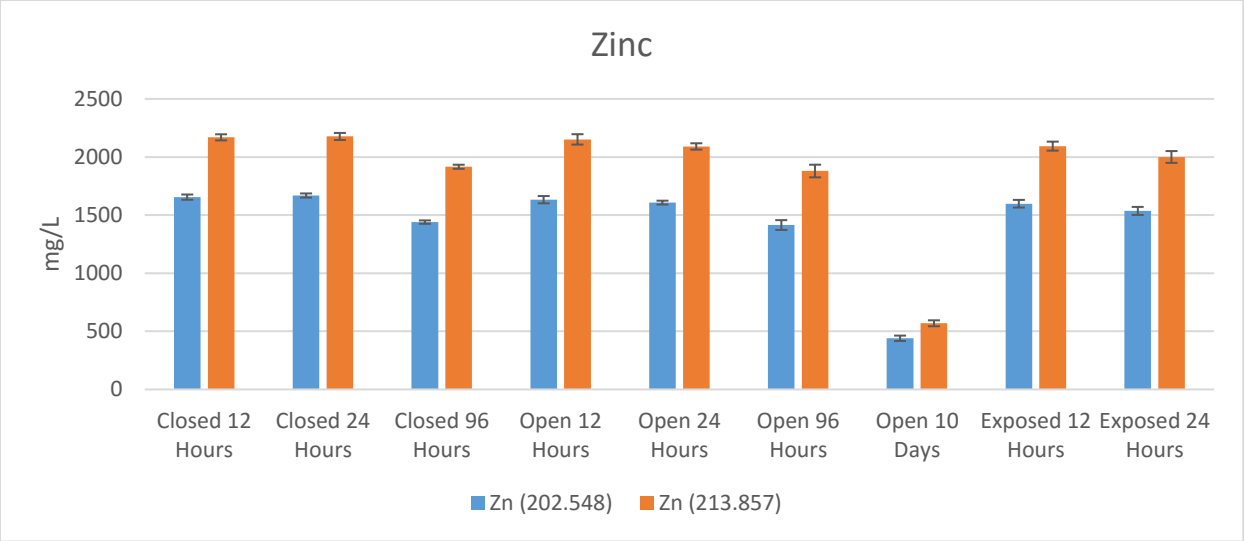

Figure 4.30: Axial view exposure test of zinc in 12 M KOH filtered fuel (n=5)

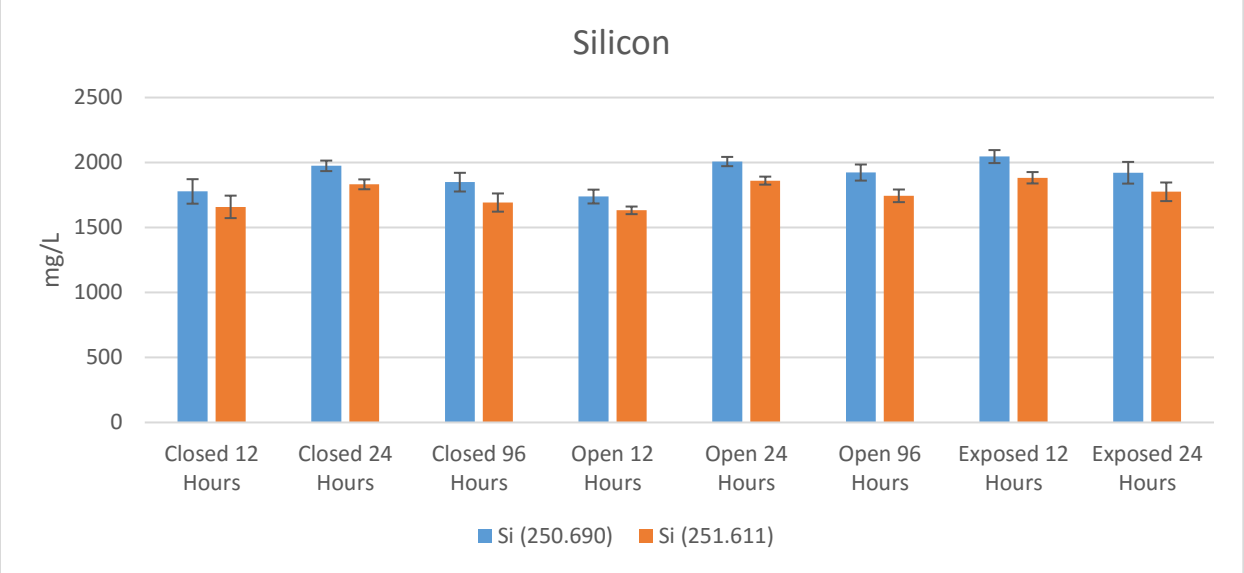

Figure 4.31: Axial view exposure test of silicon in 12 M KOH filtered fuel (n=5)

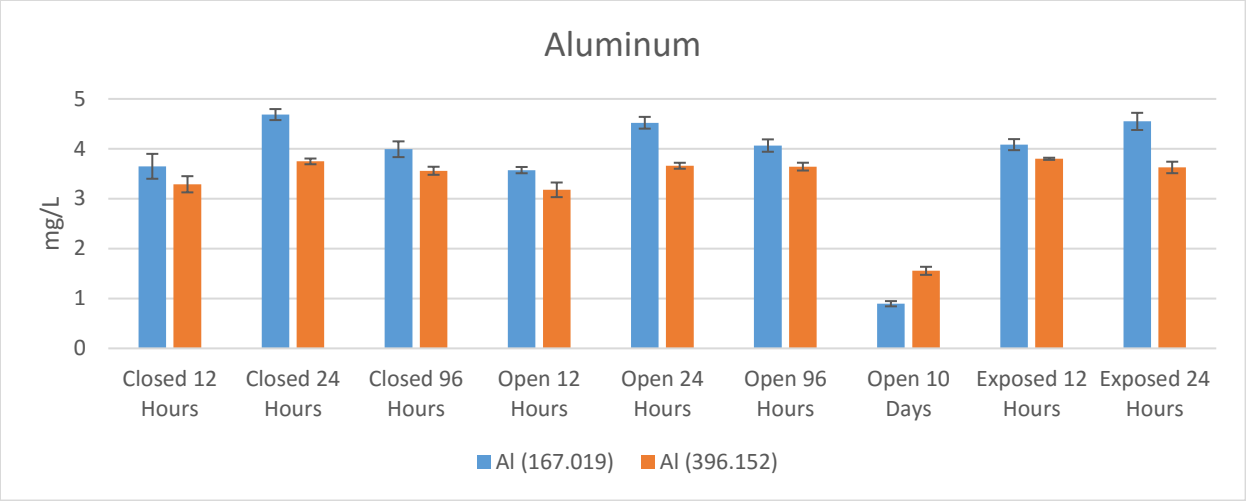

Figure 4.32: Axial view exposure test of aluminum in 12 M KOH filtered fuel (n=5)

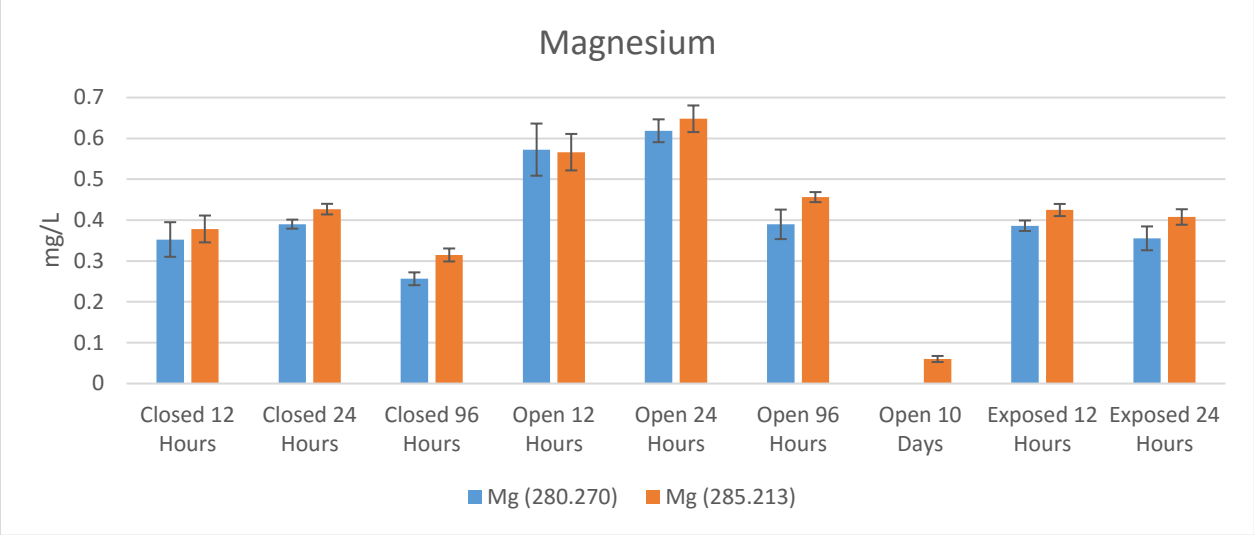

Figure 4.33: Axial view exposure test of magnesium in 12 M KOH filtered fuel (n=5)

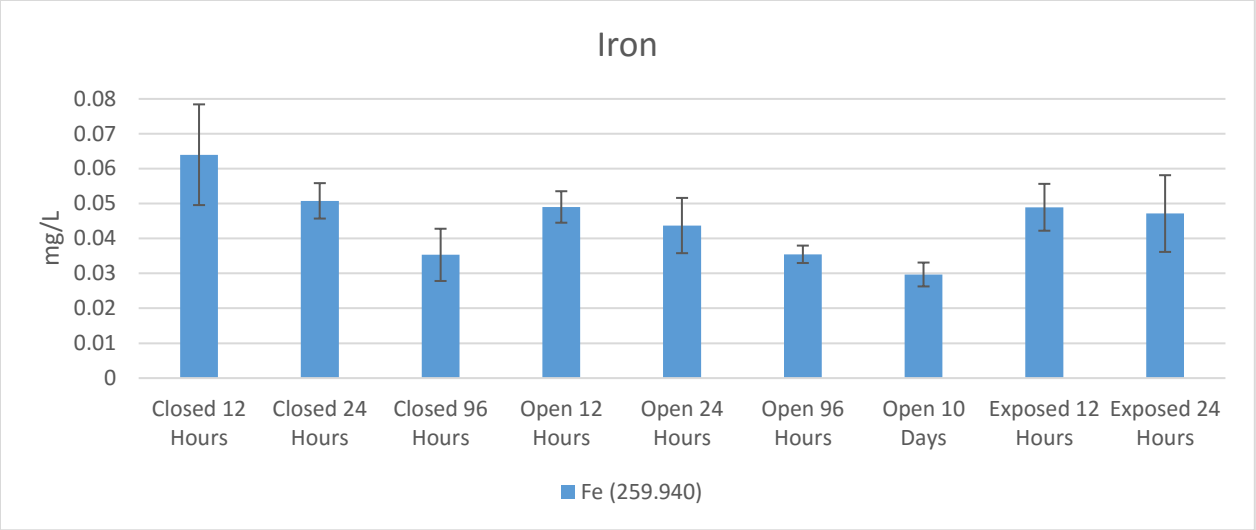

Figure 4.34: Axial view exposure test of iron in 12 M KOH filtered fuel (n=5)

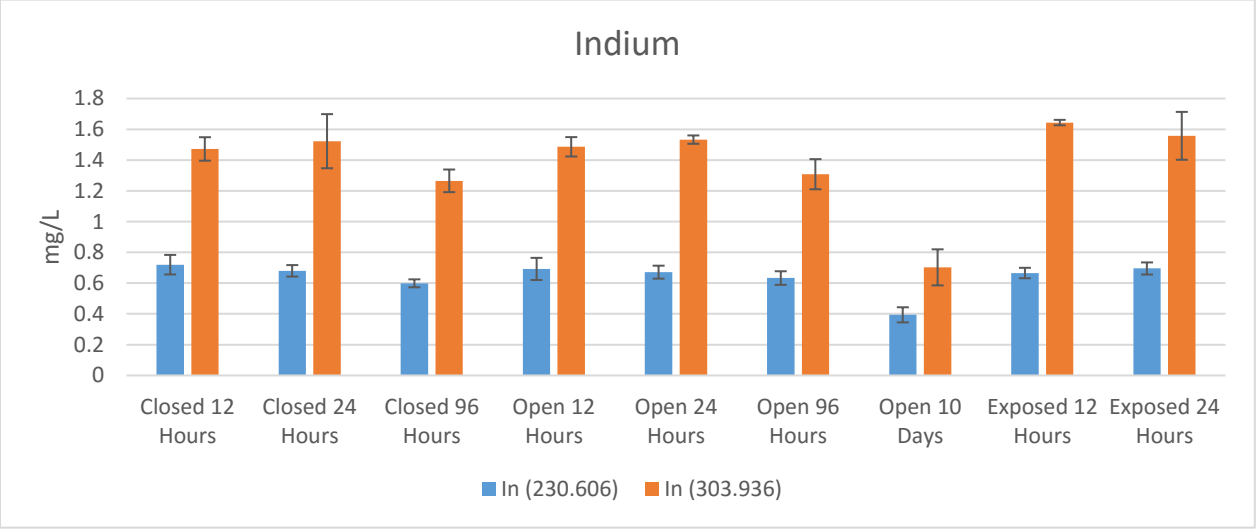

Figure 4.35: Axial view exposure test of indium in 12 M KOH filtered fuel (n=5)

To confirm that the dissolved analytes were in fact being lost to the potassium carbonate precipitate, elemental concentrations in precipitate and the aged fuel it was taken from were determined and compared to the same fuel sample prior to exposure to air for 96 hours (Fig. 4.36). These results prove that the precipitate content accounts for the difference in analyte concentration between fresh and exposed fuel (within error). While the carbon content is greater in both the aged fuel

and precipitate compared to the fresh fuel, the concentrations of In, Al, Si, and Zn in the aged fuel and precipitate add up to match those in the original fuel. Furthermore, these results demonstrate that very little Si is lost to the precipitate, while the other dissolved analytes are readily taken up by the potassium carbonate.

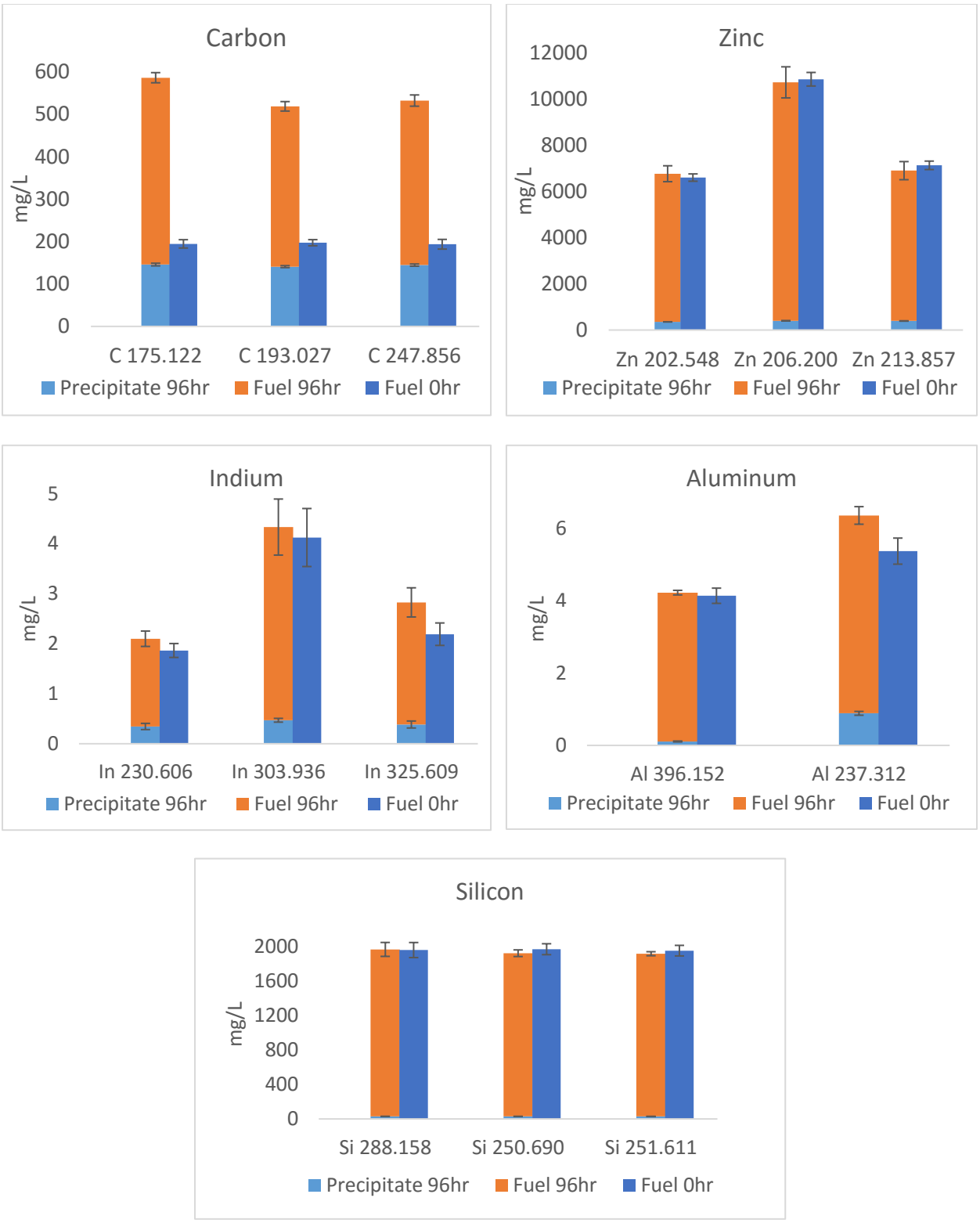

Figure 4.36: Comparisons of a fresh filtered fuel (0 hrs) to the additive concentrations of the same fuel after 96 hours of exposure to air, and its precipitate (n=5). Fe and Mg are excluded due to their concentrations in precipitate being undetectable. All results are from lateral view experiments.

4.3.7 Zinc oxide particle analysis

In order to analyze the potassium zincate electrolyte fuel in its entirety, the zinc oxide particles were removed from the fuel and an elemental analysis was conducted for four separate batches of particles. All batches were analyzed with the prototype V-groove nebuliser, while the Particle C batch was additionally analyzed with the OneNeb nebulizer for comparison (Table 4.9). Particle batches A and B were taken from one bottle of fuel provided by ZincNyx, while Particle batches C and D were taken from a second bottle sent by ZincNyx. These are all identified as separate batches as they were separated from the fuel, washed, dried, and prepared for analysis separately, in order to check for the effects of different sample preparation techniques. For instance, Particle batch A was not sufficiently washed prior to drying, resulting in potassium carbonate precipitate forming on the particles. This batch therefore has drastically higher concentrations of carbon and potassium, in addition to higher levels of zinc and aluminum, yet a decreased concentration of In, when compared to the other particle batches. Due to these differences, but a generally similarity among the other batches, Table 4.10 shows averages both including and excluding outlier A. Empty regions of Table 4.9 indicate analytes that were not detected for the given particle batch. For instance, Fe was only detectable in Particle D, and Mg was only detectable in Particles C and D.

Table 4.9: Analysis of ZnO particles (µg/g, n=5) mean ± standard deviation for "particle portions" A, B, C, and D

Element Line (nm)	PARTICLE A Prototype	PARTICLE A Prototype Error (±)	PARTICLE B Prototype	PARTICLE B Prototype Error (±)	PARTICLE C Prototype	PARTICLE C Prototype Error (±)	PARTICLE C OneNeb	PARTICLE C OneNeb Error (±)	PARTICLE D Prototype	PARTICLE D Prototype Error (±)
Al 396.152	102	24	25.1	6.3			8.0	2.24		
C 175.122	52200	2700	7850	150	3980	210	2990	130	10900	47
C 193.027	51500	2700	7780	200	3890	220	2820	110	10800	26
C 247.856	45900	2800	6840	170	3640	230	2520	120	10700	60
Fe 234.350									14.9	0.5
In 230.606	295	110	1860	26	1470	17	1430	14	1980	19
In 303.936	1170	170	1930	54	1480	22	1460	9	2030	36
In 325.609	1150	100	1920	31	1480	11	1460	6	2020	24
Mg 285.213					119	2			154	2
Si 250.690	476	62	385	8.05	302	4	401	3	337	3
Si 251.611	346	34	441	13	431	4	431	2	474	7
Si 288.158	818	38	439	5	321	2	399	2	345	4
K 766.491	62800	550	28700	104	7190	320	7310	770	3490	13
K 769.897	146000	660	44600	74	18100	450	17900	1200	8470	30
Zn 202.548	800000	5400	447000	2200	306000	950	220000	650	175000	769
Zn 206.200	848000	3900	614000	4700	463000	600	344000	590	283000	394
Zn 213.857	763000	4100	384000	1100	364000	1300	198000	300	194000	945

Table 4.10: Average concentration of analyte (μg/g) for particle sample groups A, B, C, and D

Element Line (nm)	Average A, B, C, D	Error (±) A, B, C, D	Average B, C, D	Error (±) B, C, D
Al 396.152	64	54	25	0
C 175.122	19000	23000	7600	3500
C 193.027	19000	22000	7500	3500
C 247.856	17000	20000	7100	3500
In 230.606	1400	770	1800	270
In 303.936	1700	400	1800	290
In 325.609	1600	400	1800	290
Mg 285.213	140	25	140	25
Si 250.690	380	75	340	42
Si 251.611	420	55	450	23
Si 288.158	480	230	370	62
K 766.491	26000	27000	13000	14000
K 769.897	54000	63000	24000	19000
Zn 202.548	430000	270000	310000	140000
Zn 206.200	550000	240000	450000	170000
Zn 213.857	430000	240000	310000	100000

4.3.8 Pure KOH analysis

12 M KOH, which had previously been used as the blank for flow injection experiments was analyzed via several dilution methods in order to check its validity as a blank. This analysis was done with both the prototype V-groove and OneNeb nebuliser for the first test sample of KOH. A second test was performed with the prototype nebuliser alone in which KOH samples A and B were taken from separate bottles provided by ZincNyx, but analyzed on the same day. As has been previously discussed, the dilution method results in enhanced analyte signals due to the change in nebuliser efficiency when the samples have differing viscosities from the standards. This effect is especially apparent for the 100-fold dilution results. Although all analytes found in the fuel were tested, only C, K, Al, and Si were detected in the 12 M KOH samples. Due to the formation of potassium carbonate on potassium hydroxide when exposed to air, the carbon content was unsurprising. Although Si and Al were unexpected contaminants, their low concentrations were decidedly minute in comparison to their

concentrations in the fuel (7.7 mg L^{-1} of Al, and 2021 mg L^{-1} of Si). Note that this is when considering the 1/100 dilution experiment as an unacceptable method. Therefore, the 12 M KOH was confirmed to be suitable for use as a blank for FI experiments.

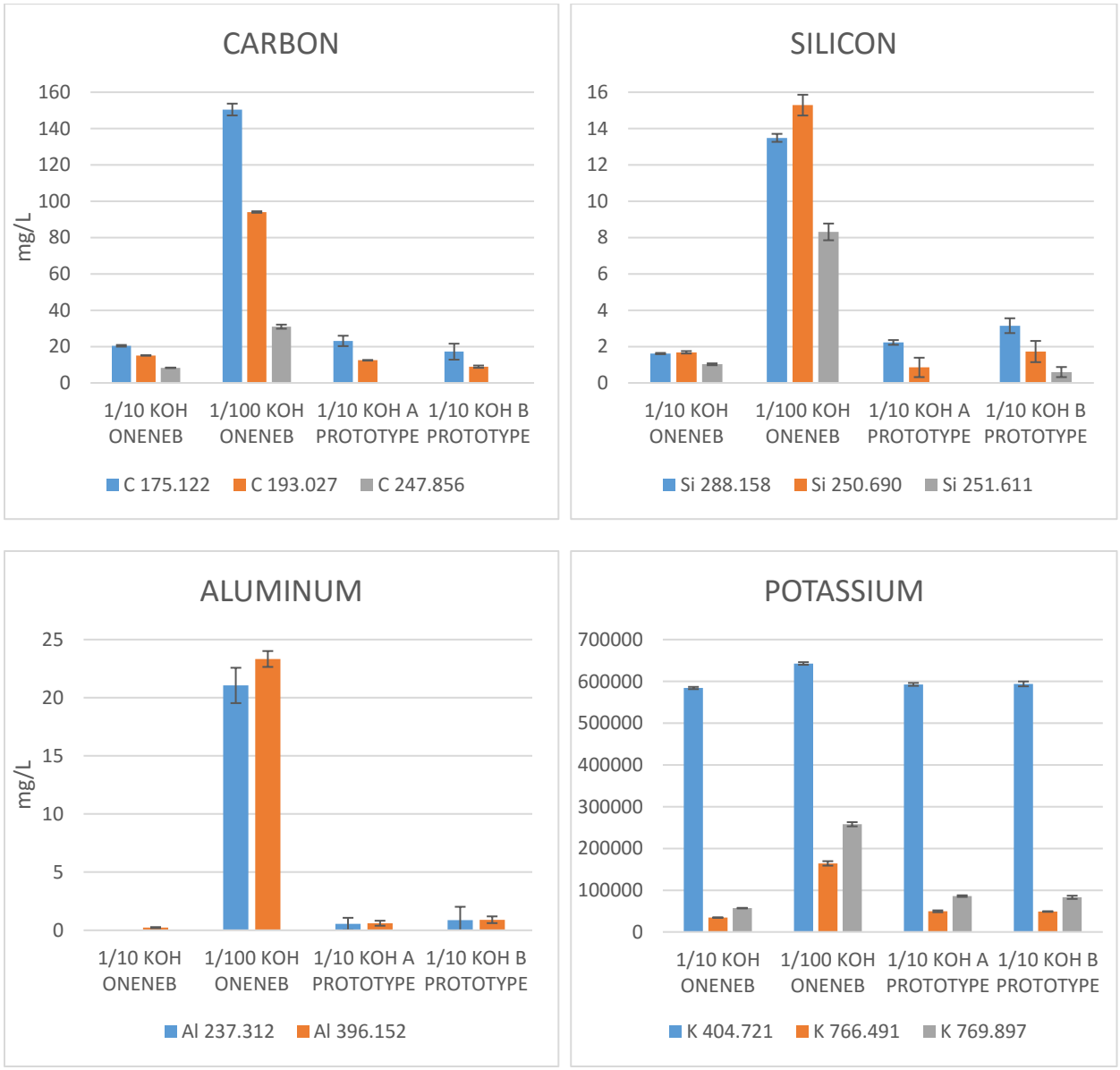

Figure 4.37: "Pure" 12 M KOH analysis with two different nebulisers and two dilution factors (mg/L, n=5). Lateral view was used for all experiments. KOH "A" and "B" are samples taken from different bottles and analyzed on the same day.

4.3.9 Simultaneous analysis of all analytes in liquid fuel

In order to simplify the experimental procedure and require only one factor of dilution (if any), and since a 4-fold dilution with standard additions had previously proven to be optimal for Zn analysis, 4-fold DDW dilution experiments without standard addition were attempted for K analysis alone (not shown in Table 4.8). However, following comparisons of all methods attempted for K and Zn analysis, it was found that a 10-fold dilution with standard additions for Zn, and without standard additions for K, provided the most accurate results. In both cases, using the least sensitive lines for analysis is imperative, with K 404.721 nm in axial view, and Zn 210.442 nm in lateral view having the leading closeness to the given values. Top choices of all methods for Zn and K analysis were narrowed down to those shown in Fig. 4.38 and 4.39. Given the results of section 4.3.6, and the ability of FI with undiluted fuel to provide relative accuracy for all dissolved analytes, this method was chosen for the determination of the remaining elements.

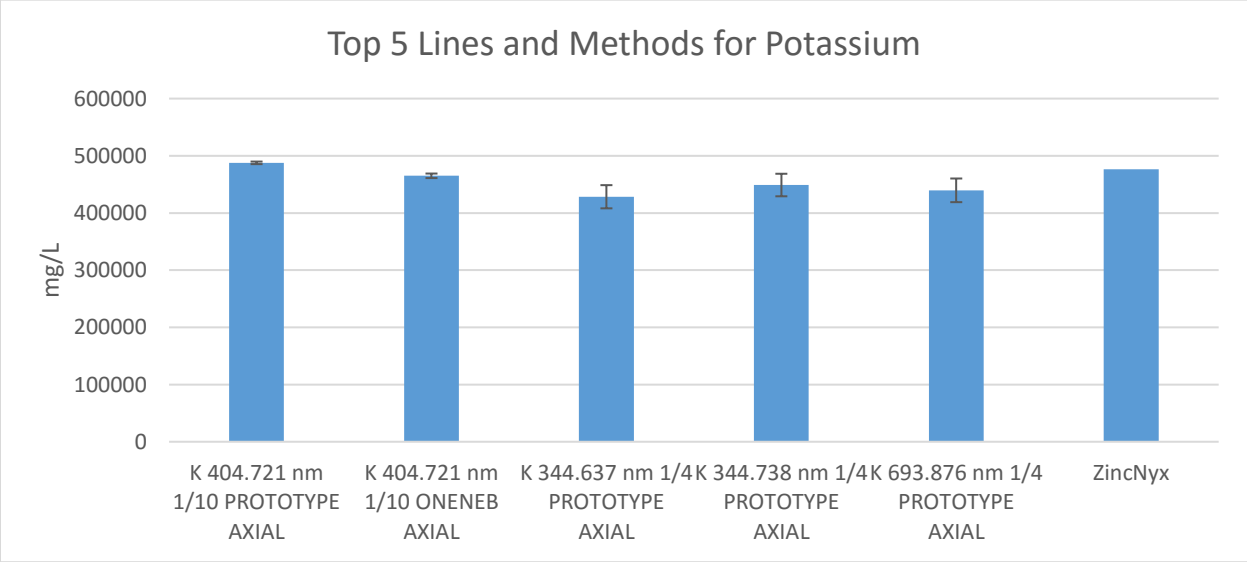

Figure 4.38: Five elemental line/ method combinations that provide the closest correlation to the given potassium concentration.

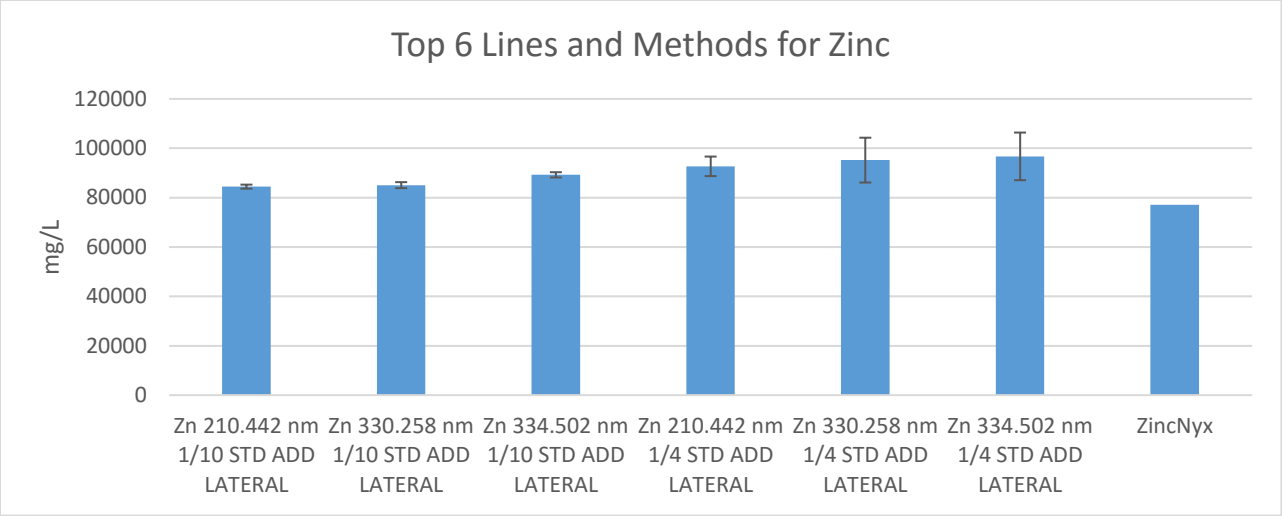

Figure 4.39: Six elemental line/ method combinations that provide the closest correlation to the given zinc concentration. All methods use the prototype V-groove nebuliser.

Table 4.11: Best methods and lines for overall and simultaneous determination of elemental analytes in fuel (concentrations in mg/L, n=5). All methods use the prototype V-groove nebulizer. * indicates other lines provide similar results.

Element and Line (nm)	Method	Concentration ± Error	ZincNyx Value
Al (237.312)*	FI, lateral	5.84 ± 0.40	7.7
C (193.029)*	FI, lateral	142 ± 3	N/A
Fe (259.940)*	FI, lateral	0.250 ± 0.60	<2.0
In (230.606)*	FI, lateral	2.32 ± 0.10	<2.0
Mg (285.213)*	FI, lateral	0.960 ± 0.40	3.6
Si (251.611)*	FI, lateral	1970 ± 60	2021
K (404.721)	1/10 diluted in DDW, axial	487000 ± 2000	476688
Zn (210.442)	1/10 diluted in DDW, standard additions, lateral	84500 ± 800	77051

All chosen methods for the overall analysis of the potassium zincate electrolyte fuel are listed in Table 4.11. In order to follow this table's outline while analyzing the fuel via a fast and reliable operation, the following procedure was envisioned for ZincNyx Energy Solutions:

1. Prepare a sample of fuel by filtering the ZnO particles from the liquid fuel portion. The fuel sample should be quickly sealed after filtering to avoid formation of precipitate. Should analysis of the particles be required, washed and dried particles should be dissolved in minimal amounts of nitric acid and diluted with DDW.
2. Prepare three sets of standards. The first set (Set A) is used for FI and consists of spiking pure 12 M KOH with a multielement stock (Al, Fe, C, In, Mg, Si), resulting in final concentrations of 0.5 ppm, 1 ppm, 2 ppm, 4 ppm, 8 ppm, and 10 ppm. The second set (Set B) of standards are made by spiking DDW with a K stock solution, yielding final concentrations of 10 ppm, 50 ppm, 100 ppm, 1000 ppm, and 10000 ppm. If particles are also to be analyzed, the Set B standards should also be spiked with a multielement stock to total Al, Fe, C, In, Mg, and Si concentrations of 0.5ppm, 1 ppm, 2 ppm, 4 ppm, and 8 ppm. The third set (Set C) of standards are prepared from a pre-made 100mL sample of fuel diluted 10-fold with DDW. To 20-mL bottles, powdered ZnO is added (0 g, 0.1 g, 0.2 g, 0.25 g, and 0.3 g) and each bottle is topped to 20-mL with the diluted fuel.
3. Set up the experiment on ICP-Expert Software. The method conditions are given by Table 4.1. Set replicates to 5, use a fitted background correction, and 3 pixels for detector readings. 22 series (total for blanks, standards, and samples) should be set.
4. After flushing the system with DDW for 20 min, aspirate a blank of DDW, Set B standards, particle sample(s), and Set C standards, all in sequence in analysis mode. The system should be rinsed with DDW between each standard. These results will be used for Zn and K determination in the fuel, and for all other analytes in the particles. Note that the 0 g standard from Set C doubles as the sample for Set B. For simplicity, dual mode can be used throughout this experiment.

5. Set up the flow injection device and switch to transient mode in lateral view. After flushing the system, inject Set A standards from lowest concentration to highest, saving at least 3 replicates of each standard. Inject the undiluted fuel last, taking at least 5 replicates. These results will be used for Al, Fe, C, In, Mg, and Si analysis.

4.4 Conclusion

Through the combined use of flow injection, fuel dilution, and standard additions, a sequential procedure for the overall analysis of a potassium zincate electrolyte fuel was recommended. Including analysis of both the ZnO particles and the 12 M KOH with dissolved analytes, this procedure is to be used by ZincNyx Energy Solutions for regular in-house quality assurance tests. Although both a prototype V-groove nebuliser and a OneNeb nebuliser were tested throughout this work, the prototype V-groove nebuliser was ultimately chosen for the final procedure as the majority of the experiments were completed with this setup. Additionally, the V-groove nebuliser is intended for high solid nebulisation and can be used for the analysis of suspended particles [19]. Therefore, it may be possible to analyze the size distribution of the fuel's ZnO particles. While this research could not be conducted due to the large integration time on the ICP Expert Software, changes to the software would likely allow for this particle analysis.

In order to determine all dissolved analytes and the CO_3^{2-} corrosion product in the fuel solution (Al, C, Fe, In, Mg, and Si), direct analysis of the undiluted filtered fuel with flow injection was proven to be the best method. Measurement of zinc in the fuel was most optimally completed with standard additions of ZnO powder in fuel diluted 10-fold with DDW and by measuring the less-sensitive 210.442 nm emission line. By again diluting the fuel 10-fold with DDW but doing a simple external calibration instead of standard additions, K concentration could be determined when monitoring the less-sensitive

line (404.721 nm) in axial mode. Meanwhile, by simply dissolving the ZnO particles in nitric acid, portions of particles could be analyzed with a simple DDW-based calibration curve.

This research also proved that the development of potassium carbonate precipitate on fuel exposed to the air (including air in the headspace of bottles) resulted in a decrease in concentrations of dissolved analytes in the fuel, as Al, Fe, In, Mg, and Zn precipitate out of solution over time. The missing concentrations of these elements were found in the analyzed precipitate, meaning there is a degradation of the fuel over longer periods of storage time, should these dissolved analytes be important to the functionality of the fuel.

Future work would benefit from using an ICP-OES instrument that measures lower emission lines in order to measure the oxygen concentration of the fuel. This measurement, in addition to analysis of H lines, would allow for a thorough determination of KOH and water in the fuel. Since the Agilent 5100 can only measure lines at and above 170 nm, the most sensitive oxygen lines in the low UV region cannot be reached. The accurate measurement of O and H in aqueous solution by ICP-OES has already been achieved [20], suggesting the KOH and water determination by this method would not be an impossible feat.

4.5 References

[1] P. R. Skidmore, S. S. Greetham, Trace-metal determinations in concentrated electrolyte solutions. A comparative study, Analyst 108 (1983) 171-7.

[2] J.-X. Gao, Fast determination of carbonate in potassium hydroxide samples through inductively coupled plasma atomic emission spectrometry, Tianjin Huagong, 27 (2013) 44-45.

[3] L. Ding, T. Zhang, C. Gong, J. Xia, Detection of metal ions in potassium hydroxide with inductively coupled plasma optical emission spectrometry method, Wujiyan Gongye, 44 (2012) 40-42.

[4] W. K. W. Lee, J. S. J. van Deventer, Use of Infrared Spectroscopy to Study Geopolymerization of Heterogeneous Amorphous Aluminosilicates, Langmuir, 19 (2003) 8726-8734.

[5] W.K.W. Lee, J.S.J. van Deventer, Structural reorganisation of class F fly ash in alkaline silicate solutions, Colloids Surf., A, 211(1), (2002),49- 66.

[6] J.Z. Xu, Y.L. Zhou, Q. Chang, H.Q. Qu, Study on the factors of affecting the immobilization of heavy metals in fly ash-based geopolymers, Mater. Lett, 60(6), (2006), 820-822.

[7] Y.-w. Lu, Y.-c. Sun, An on-line electrodialyzer-ICP-MS analytical system for direct determination of trace metal impurities in KOH, J. Anal. At. Spectrom. 23 (2008) 574-578.

[8] W. Xu, R. C. Sandford, P. J. Worsfold, A. Carlton, G. Hanrahan, Flow Injection Techniques in Aquatic Environmental Analysis: Recent Applications and Technological Advances, Crit. Rev. Anal. Chem, 35, 3, (2005), 237-246.

[9] D.C. Harris, Quantitative Chemical Analysis, 9th Edition, W.H. Freeman Company, New York, NY, 2016.

[10] J. M. Mermet, Use of magnesium as a test element for inductively coupled plasma atomic emission spectrometry diagnostics. Anal. Chim. Acta, 250, (1991), 85 – 94.

[11] I.B. Brenner, M. Zischka, B. Maichin, G. Knapp, Ca and Na interference effects in an axially viewed ICP using low and high aerosol loadings, J. Anal. At. Spectrom, 13, 11, (1998), 1257-1264.

[12] Boss, C.B and Fredeen, K. J. Concept, Instrumentation and Techniques in Inductively Coupled Plasma Optical Emission Spectrometry, Second Edition, Perkin Elmer, (1997).

[13] X. Romero, E. Poussel and J. M. Mermet, Influence of the operating conditions on the efficiency of internal standardization in inductively coupled plasma atomic emission spectrometry. Spectrochim. Acta B, 52, (1997), 487 – 493.

[14] I. Novotny, J. C. Farinas, J. L. Wan, E. Poussel and J. M. Mermet, Effect of power and carrier gas flow rate on the tolerance to water loading in inductively coupled plasma atomic emission spectrometry. Spectrochim. Acta B, 51, (1996), 1517-1526.

[15] M. Grotti, C. Lagomarsino, F. Soggia and R. Frache, Multivariate Optimization of an Axially-Viewed Inductively Coupled Plasma Multichannel-Based Emission Spectrometer for the Analysis of Environmental Samples, Ann. Chim. (Rome, Italy), (2005), 95, 37–51.

[16] M. Grotti, C. Lagomarsino and R. Frache, Multivariate study in chemical vapor generation for simultaneous determination of arsenic, antimony, bismuth, germanium, tin, selenium, tellurium and mercury by inductively coupled plasma optical emission spectrometry, J. Anal. At. Spectrom., (2005), 20, 1365-1373.

[17] Brennan, M., A Practical Approach to Quantitative Metal Analysis of Organic Matrices, John Wiley & Sons, (2008), West Sussex, United States.

[18] D. Goitom, Fundamental Studies on Direct Injection Nebulisers for Sample Introduction in ICP Spectrometry Aerosol Properties, ICP Characteristics and Analytical Performance, A thesis for the Department of Chemistry, Analytical Chemistry, (2006), Umeå University, Umeå, Sweden.

[19] P. Gaines, Sample Introduction for ICP-MS and ICP-OES, Inorganic Ventures, Spectroscopy Solutions for Materials Analysis, (2005).

[20] C. Odenigbo, Y. Makonnen, A. Asfaw, T. Anastassiades, D. Beauchemin, Towards the Use of Inductively Coupled Plasma Optical Emission Spectrometry for the Elemental Analysis of Organic Compounds such as Glucosamine J. Anal. At. Spectrom. 29 (2014) 454–457.

Chapter 5: Summary and Future Work

5.1 Chapter Summary and General Conclusions

With the aim of improving the analytical capabilities of ICP-OES, this thesis has explored and established several new methods for improved sensitivity, detection limit, precision, and robustness, and the ability to analyze a strong base directly. In three projects, the varying possibilities of analysis with ICP-OES when using different sample introduction systems were probed and broadened.

The first project sought to improve on previous methods of heating a pre-evaporation tube connected to an ultrasonic nebuliser for improved sensitivities and detections limits over the conventional USN-HC setup. As previously found, the USN-PET(IR) setup provided drastic improvements over USN-HC. Rather than removing water to pre-concentrate the analyte, water was preserved by the USN-PET(IR) setup, allowing the water vapour to act as a load buffer in the plasma and be a main source of hydrogen for the facilitation of energy transfer between the bulk of the plasma and its central channel. By comparing two different heaters (a rope IR heater and a block IR heater), it was determined that the uniformity of the pure IR heating facilitated by the block heaters provides greater improvements in sensitivity and detection limits. The rope heaters on the other hand, resulted in less uniform heating as they involve both convective and IR heating and caused the area downstream of the heated region to be of higher temperature than that measured by the thermocouple at the base of the torch. Hence, the optimal temperature value could not be used for pre-evaporation all along the PET. In comparing the best method of the current experiments to the best method of past research, it was confirmed that higher temperatures provide more effective pre-evaporation and therefore lower detection limits. However, by lowering the temperature of the previously published USN-PET(IR) method and cutting the sample uptake rate by half, a system with improved sample introduction efficiency and comparable sensitivity, detection limit, precision, and robustness was achieved. This

suggests that, depending on the application, the new, more efficient method may be preferred over the old.

This work was also compared on two instruments: the SPECTRO ARCOS, and the Agilent 5100. Due to space restrictions of the torch box and sample introduction area and the resulting need for a longer PET, in addition to the plastic torch construction of Agilent's torches, the methods optimized for the Agilent instrument saw far fewer improvements in detection limit and sensitivity. Therefore, future work on this instrument could include cutting the plastic shelf of the sample introduction area in order to move the USN closer to the torch box, allowing for a reduced PET length which could be made comparable to the length used on with the ARCOS instrument. By using a shorter PET, heating is made more efficient and sticky elements such as Hg have less opportunity to stick to the walls of the tube. Furthermore, the Agilent torch could be modified by hollowing out the plastic casing (creating a tunnel around the torch injector) and by making the casing from a material that is more resistant to heating. In this way, a larger surface area of the torch injector could be heated, and the pre-vaporized aerosol would not cool before entering the plasma. Through these modifications, the benefits of using the Agilent instrument could be combined with the physical advantages in sample introduction characteristics achieved on the ARCOS instrument.

The second project involved the addition of an IR-heated pre-evaporation tube to a multimode sample introduction system, and comparison to past work in which the PET was heated with heating tape. Improvements in sensitivity, detection limit and robustness were achieved in all three MSIS operating modes (dual mode, hydride generation mode, and nebulisation mode); however the greatest improvements were achieved with those modes involving HG. This investigation led to greatly improved detection limits for Be when MSIS(IR) was employed over conventional MSIS, suggesting that beryllium hydride may be produced by the combination of the HG reaction and heat. In general, the improvements in analytical capabilities throughout this research were correlated to hydride-generation

enhancing sensitivity in hydride-forming elements (i.e. when compared to PN), the hydrogen by-product of MSIS HG improving plasma excitation efficiency, and the pre-evaporation of the aerosol resulting in preserved water vapour for improved plasma excitation characteristics and reduced sample droplet size.

While experiments on the Agilent 5100 provided improvements over ARCOS in terms of robustness, it is expected that greater improvements in sensitivity and detection limit can be achieved for the Agilent setup if the torch is modified to provide a larger surface area for heating. In the same way discussed about for USN-PET(IR), the plastic casing of the torch could be made out of a more heat-resistant material (i.e. Teflon) and formed with a hollow inner area so that the rope heater can be wrapped further up the torch injector. By heating closer to the ICP, the pre-vaporised aerosol will not have time to cool and condense prior to reaching the plasma, and the potential improvements in detection limits by using a PET will not be lost.

The final project involved creating a method for the overall analysis of a 12 M KOH electrolyte fuel from ZincNyx Energy Solutions. This was to include trace metal analysis of both the ZnO particles and the 12 M KOH containing dissolved analytes, as well as confirmation of the potassium content in each. By combining flow injection for direct analysis of an undiluted fuel, diluted fuel analysis, and standard additions with ZnO and KNO_3, a procedure for the accurate elemental analysis of the fuel was produced. All dissolved analytes and the CO_3^{2-} corrosion product in the fuel solution (Al, C, Fe, In, Mg, Si) were directly analysed from undiluted filtered fuel via flow injection. Zinc was determined through standard additions of ZnO powder in fuel diluted 10-fold with DDW and by measuring the less-sensitive 210.442 nm emission line. Similarly, K was most successfully quantified by again diluting the fuel 10-fold with DDW but doing a simple external calibration instead of standard additions. One of the least sensitive K lines (404.721 nm) provided the most accurate results, as it did not saturate the detector. The particles were analyzed by dissolving the ZnO particles in nitric acid, and quantifying the elemental composition with a simple DDW-based calibration curve. This procedure is expected to be employed by

ZincNyx for routine in-house quality assurance tests. This work also compared two different nebulisers from Agilent, a prototype V-groove and a OneNeb, and was therefore useful in uncovering the benefits of each.

By analyzing the 12 M KOH fuel over different exposure times and by varying the type of exposure, it was found that the development of potassium carbonate precipitate on the surface of the fuel resulted in decreased concentrations of the dissolved analytes. Through analysis of fresh and aged fuel, and the potassium carbonate precipitate, it was found that Al, Fe, In, Mg, and Zn leached out of solution into the precipitate over time.

In the future, modifications to the ICP-Expert software could be made to reduce the read time of the signal in order to analyze the size distribution of the ZnO particles. While the system itself appears capable of such a task, particularly with the V-groove nebuliser (which is intended for analysis of high solid content and suspended particles), the high integration time of 1 second results in an averaging of the particle signals. Therefore, single particle analysis could not be conducted on this instrument, but it is believed a change to the software could eliminate any obstacles. Furthermore, if the detection of lower emission lines was available on the Agilent 5100, the oxygen lines could be monitored and quantification of KOH and water content in the fuel could be performed. While the Agilent 5100 only measures as low as 170 nm, past experiments on the SPECTRO ARCOS (which reaches the low-UV range) have proven the accurate measurement of O and H in aqueous solution by ICP-OES. By employing such a method for the analysis of the 12 M KOH electrolyte, a fuller picture of the exact concentrations of all contents in the fuel may be reached.